Increasing the Feasibility of Superconducting Generators for 10 MW Direct-Drive Wind Turbines

Liu, Dong

DOI
10.4233/uuid:074d4f96-e7bf-4dde-a7b4-86c9dd2e214f

Publication date
2017

Document Version
Final published version

Citation (APA)
Liu, D. (2017). *Increasing the Feasibility of Superconducting Generators for 10 MW Direct-Drive Wind Turbines*. [Dissertation (TU Delft), Delft University of Technology]. https://doi.org/10.4233/uuid:074d4f96-e7bf-4dde-a7b4-86c9dd2e214f

Increasing the Feasibility of Superconducting Generators for 10 MW Direct-Drive Wind Turbines

INCREASING THE FEASIBILITY OF SUPERCONDUCTING GENERATORS FOR 10 MW DIRECT-DRIVE WIND TURBINES

Proefschrift

ter verkrijging van de graad van doctor
aan de Technische Universiteit Delft,
op gezag van de Rector Magnificus prof. ir. K.C.A.M. Luyben,
voorzitter van het College voor Promoties,
in het openbaar te verdedigen op 20 juni 2017 om 10:00 uur

door

Dong LIU

Master of Science in Electrical Engineering,
Technische Universiteit Delft,
geboren te Lanzhou, Gansu, China.

Dit proefschrift is goedgekeurd door de

promotor: prof. dr. J. A. Ferreira
copromotor: dr. ir. H. Polinder
copromotor: dr. A. B. Abrahamsen

Samenstelling promotiecommissie:

Rector Magnificus,	voorzitter
Prof. dr. J. A. Ferreira,	Technische Universiteit Delft, promotor
Dr. ir. H. Polinder,	Technische Universiteit Delft, copromotor
Dr. A. B. Abrahamsen,	Technical University of Denmark, copromotor
Onafhankelijke leden:	
Prof. dr. Z. Q. Zhu	The University of Sheffield
Prof. dr. G. J. W. van Bussel	Technische Universiteit Delft
Prof. dr. R. Ross	Technische Universiteit Delft
Dr. M. Dhallé,	Universiteit Twente

This project receives funding from the European Union's Seventh Framework Programme for research, technological development and demonstration under grant agreement No. 308974.

Printed by: Ridderprint BV

Front & Back: Dong Liu

ISBN 978-94-6299-627-4

An electronic version of this dissertation is available at
`http://repository.tudelft.nl/`.

CONTENTS

SUMMARY

In recent years, superconducting synchronous generators (SCSGs) have been proposed as an alternative to permanent magnet synchronous generators (PMSGs). They are expected to reduce the top head mass and the nacelle size for such large wind turbines. In 2012, the INNWIND.EU project initiated this research to investigate SCSGs for 10-20 MW direct-drive offshore wind turbines. However, the feasibility of SCSGs was limited by a few critical issues, such as high costs, AC losses in the superconducting winding and excessive short circuit torque. Furthermore, SCSG designs proposed in the literature were various but all less competitive than PMSGs. There had been no agreement on the most feasible SCSG designs.

This thesis aims at increasing the feasibility of SCSGs for large wind turbines and identify the most feasible SCSG designs by investigating the following four questions:

• How to reduce the capital cost of energy of an SCSG by selecting appropriate generator topologies?

• Is the AC losses of the selected generator topologies acceptable?

• Can the short circuit torque be reduced to an acceptable level?

• What is the potential of SCSGs to have significant advantages over PMSGs?

This thesis focuses only on partially superconducting generators in which the field winding is superconducting while the armature winding is with copper conductors. This type of SCSGs is considered more feasible than fully superconducting generators for the moment. A 10 MW reference wind turbine provided by the INNWIND.EU project is used throughout this thesis.

TOPOLOGY COMPARISON BASED ON CURRENTLY AVAILABLE MgB_2 SUPERCONDUCTORS

The levelized cost of energy (LCoE) of a wind turbine using an SCSG could be much higher than that of conventional wind turbines due to the employment of costly superconducting wires and cryogenic cooling systems. The high LCoE hinders the commercialization of SCSGs for wind power industry and limits the feasibility of SCSGs. Electromagnetic designs for reducing the capital cost of energy of SCSGs are assessed by comparing twelve different generator topologies. These topologies combine iron and non-magnetic material in the rotor back core, rotor pole core, stator tooth and stator yoke. Each topology is optimized for the lowest levelized capital

cost of energy (LCCoE). The optimization applies the genetic algorithm. The optimization method combines 2D stationary finite element (FE) models and analytical models to calculate the active material costs and energy production. A commercial MgB_2 superconducting wire supplied by Columbus Superconductors is used in the field winding operating at 20 K.

Based on the current unit cost and current density capability of the employed MgB_2 wire, the topologies with more iron have a lower LCCoE than the other topologies with more non-magnetic cores. The fully iron-cored topology with salient iron poles is most advantageous regarding the LCCoE as well as the resulting annual energy production, active material cost and superconductor length.

Since the superconductor technology is developing fast, only using the current properties of the MgB_2 wires may limit the perspective of comparing the topologies. The topologies that are less advantageous at present may become promising in the long run. Three scenarios on the employed MgB_2 wire are therefore investigated, assuming

1) reducing the wire cost per unit length to 1/4,

2) four times engineering critical current density, and

3) the combination of both.

These scenarios can effectively lower the capital LCCoE for all the topologies, especially those with more non-magnetic cores. The third scenario, considered as a long-term goal, results in very small differences of LCCoE among the twelve topologies. Then the topologies with more non-magnetic cores will catch up those with more iron. Aiming at a lower LCCoE, however, those topologies having the most iron in the core are still the most promising candidates for both now and the long term, although they could result in large generator masses.

RIPPLE FIELD AC LOSSES IN MgB_2 SUPERCONDUCTING FIELD WINDINGS

The most promising fully iron-cored topology with salient poles has iron teeth in the stator. These iron teeth produce high-order magnetic field harmonics. These harmonics produce AC losses in the superconducting field winding. The AC loss level is evaluated by combining 2D transient FE models for calculating the magnetic field and analytical models for calculating the AC losses. The result shows that the amount of AC losses produced by iron teeth can be very small and this topology is feasible from the perspective of AC loss production.

REDUCING THE SHORT CIRCUIT TORQUE

SCSGs usually have larger magnetic air gaps than conventional generators because of space for a cryostat or use of non-magnetic cores. As a result, the inductance becomes lower and then the short circuit torque can become as high as more than 10 times the rated torque which is too high for wind turbine constructions. Three

approaches of suppressing the short circuit torque are assessed. The first is to use an electromagnetic shield between the field winding and the armature. The second is to use iron teeth instead of non-magnetic teeth in the stator. The third is to use armature winding segmentation with multiple power electronic converters. 2D transient FE models are used to simulate the torque during a no-load three-phase short circuit. The first and second approaches are not effective. The third approach of armature winding segmentation can effectively suppress the short circuit torque for all the four selected generator designs when only one segment is shorted, assuming the segments are independent of each other in the FE model. Increasing the number of segments improves the torque reduction and four segments can limit the peak torque below 3 times the rated torque.

POTENTIAL OF PARTIALLY SUPERCONDUCTING GENERATORS

By conducting a comparison between 10 MW SCSGs and PMSGs, the SCSGs are not competitive yet if the cost or cost of energy is chosen as the primary design objective. It is needed to look for significant advantages which will make SCSGs sufficiently attractive in the wind energy industry. The potential of partially SCSGs for 10 MW direct-drive wind turbines is assessed by investigating their performance for a very wide range of excitation currents. Performance indicators such as shear stress and efficiency and other generator characteristics are compared for the twelve generator topologies. To be sufficiently attractive, superconducting generators must have significant advantages over permanent magnet direct drive generators which typically have shear stresses in the order of 53 kPa and efficiencies of 96%. Therefore, as an example, it is investigated what excitation is required to obtain a doubled shear stress and an efficiency of 98% for four selected topologies. To achieve this generator performance, the four topologies require a range of excitation from 200 to 550 kAt (Ampere-turns) with a low armature current density of 2 A/mm^2. The more iron is used in the core of these topologies, the easier they achieve this performance. By examining the maximum magnetic flux density at the location of the superconducting field winding, feasible superconductors can be chosen according to their engineering current density capabilities. It is found that high- and low temperature superconductors can meet the performance criteria for many of the four topologies. MgB_2 superconductors are feasible for the fully iron-cored topology with salient poles but needs cooling down to 10 K.

▽ ▽ ▽

From the perspective of electromagnetic design, this thesis points out a direction to increase the feasibility of SCSGs for large direct-drive wind turbines:

• Aiming at a lower LCCoE, iron-core based generator topologies are more feasible than the other topologies and the used lengths of superconducting wires are

shorter. The fully iron-cored topologies are most feasible and their AC loss level is acceptably low. If low generator weight is also desired, however, the topologies with more non-magnetic cores can be considered once the superconducting wire becomes much cheaper and capable of much higher current densities.

• Currently, the SCSG do not show advantages of LCCoE over PMSGs. To make superconducting generators attractive to wind energy industry, the shear stress and efficiency of the generator should be much higher than those of permanent magnet generators. Such advantages may offset the disadvantages of high generator costs and complicated cryogenic cooling.

• To achieve competitive shear stresses and efficiencies, the excitation of the superconducting field winding should be increased to a high level. To realize such high excitation, LTS and HTS are more feasible than MgB_2 wires at present. In addition, iron-core based generator topologies are again more feasible than the other topologies to reach high shear stresses and efficiencies, especially the fully iron-cored topologies.

• Aiming at an acceptable short circuit torque, armature winding segmentation with multiple power electronic converters can be considered.

This direction may not be the only one. However, it takes into account the key feasibility issues at the moment from the electromagnetic design perspective. Prototypes can be built following this direction to demonstrate and prove this technology. This thesis makes a step of contribution to increase the technology readiness level of SCSGs for large direct-drive wind turbines. Efforts are still going on to achieve a mature SCSG design that should be proven to be compact, lightweight, efficient, reliable and cheap.

SAMENVATTING

De afgelopen jaren is er steeds meer interesse in supergeleidende synchrone generatoren (SCSG). Supergeleidende synchrone generatoren (SCSG) worden steeds meer als een alternatief voor permanent magneet synchrone generatoren (PMSG) gezien. Het is de verwachting dat de topmassa en de gondel afmetingen gereduceerd kunnen worden bij grote windturbines. In 2012 is het INNWIND.EU proje-ct gestart met als doel om het gebruik van SCSG in 10-20 MW direct aangedreven offshore windturbines te onderzoeken. Echter, de haalbaarheid van SCSG is gelimiteerd door een paar kritische zaken, waaronder: hoge kosten, wisselstroomverliezen in supergeleidende spoelen en een zeer hoog kortsluitkoppel. Verder waren zeer verschillende SCSG ontwerpen in de literatuur niet competitief met PMSG's. Er is geen convergentie in de ontwerp methodologie van een SCSG, er is niet één ontwerp dat eruit springt.

Dit proefschrift heeft als doel om de toepasbaarheid te vergroten van SCSG voor grote windturbines en om de meest waarschijnlijke ontwerpen te identificeren. Dit wordt gedaan op basis van de volgende 4 vragen:

• Hoe kan de kostprijs van energie beperkt worden door de generator topologie?

• Is het mogelijk om de wisselstroomverliezen terug te brengen tot een acceptabel niveau?

• Kan de kortsluitstroom beperkt worden tot een acceptabel niveau?

• Wat is het significante potentiële voordeel van een SCSG boven een PMSG ontwerp?

In dit proefschrift wordt de focus gelegd op generatoren welke gedeeltelijk supergeleiding gebruiken. De veldwikkeling is gebaseerd op supergeleidende technologie. De stator is gebaseerd op koper technologie. Dit type SCSG wordt op dit moment beschouwd als een meer haalbare oplossing dan een volledige generator gebaseerd op volledige supergeleidende techniek. Een 10 MW referentie windturbine ontwerp is aangeleverd door het INNWIND.EU project en wordt in dit proefschrift veelvuldig gebruikt.

VERGELIJKING VAN TOPOLOGIEN OP BASIS VAN BESCHIKBARE MgB_2 SUPERGELEIDERS

De genormaliseerd kosten van energie (zgn. Levelized Cost of Energy, LCoE) van een windturbine gebaseerd op een SCSG ontwerp kan veel hoger zijn dan van conventionele windturbines. Dit komt doordat er gebruik wordt gemaakt van dure super

geleidende geleiders en cryogene koeling. De hoge LCoE verhindert de vermarkting van SCSG binnen de wind turbine industrie en beperkt de haalbaarheid van SCSG. Elektromagnetische ontwerpen om de kapitaalkosten van SCSG te reduceren zijn onderzocht door twaalf verschillende generator ontwerp topologien met elkaar te vergelijken. In deze topologien worden verschillende combinaties van ijzer en niet-magnetische materialen voor het: rotor juk, rotor pool kern, stator tand en stator juk met elkaar vergeleken. Iedere topologie is geoptimaliseerd voor de laagste genormaliseerd gekapitaliseerde kosten van energie (zgn. Levelized Capital Cost of Energy, LCCoE). Een genetisch algoritme is gebruikt voor de LCCoE optimalisatie. De optimilisatie methode combineert 2D stationaire eindige elementen (FE) modellen en analytische modellen om de materiaalkosten en energie productie te berekenen. Een commerciele MgB_2 supergeleidende draad welke geleverd werd door Columbus Superconductors is gebruikt in de veld spoel welke operationeel is op 20 K.

Gebaseerd op de huidige kosten en mogelijken in de stroomdichtheid van het toegep-aste MgB_2 draad hebben de topologien met meer ijzer een lagere LCCoE dan de andere topologien met meer niet-magnetische kern materialen. De versie met een volledige ijzer kern topologie en uitspringende ijzeren polen is de meest interessante optie met betrekking tot de LCCoE en de totale opgewekte energie, materiaal kosten en gebruikte lengte van supergeleidend materiaal. De supergeleidende technologie ontwikkelt zich snel, alleen is de nu beschikbare MgB_2 draad een beperkend element in de vergelijking tussen de verschillende topologien. De topologien die nu minder interessant zijn kunnen een winnaar zijn in de toekomst. Drie verschillende scenario's in de ontwikkeling van het MgB_2 draad zijn onderzocht:

1) De kostprijs van de draad per lengte eenheid word ¼ van de huidige prijs,

2) De nuttige stroomdichtheid in de applicatie stijgt met een factor 4, en

3) Optie 1 en 2 samen.

Deze scenario's kunnen effectief de LCCoE verlagen voor alle topologien, in het bijzonder die met niet-magnetische kern materiaal. De derde optie is een langer termijn doel, en zal resulteren in hele kleine verschillen in de LCCoE tussen de 12 topologien.

In dat geval zullen de topologieen met niet-magnetisch materiaal in de buurt komen van topologieen die meer ijzer gebruiken. Teneinde een zo laag mogelijke LCCoE te krijgen zijn die topologieen die het meeste ijzer in de kern hebben desalniettemin de meest geschikte kandidaten voor nu en in de toekomst, hoewel zij leiden tot in een hoger gewicht van de generator.

WISSELSTROOMVERLIEZEN IN SUPERGELEIDENDE MgB_2 VELDWIKKELINGEN

De meest veelbelovende topologie is gebaseerd op een volledig ijzeren kern met uitspringende polen en maakt gebruik van een stator met ijzeren tanden. Deze ijzeren tanden produceren een magnetisch veld met harmonischen van hogere orde. Deze

harmonischen produceren wissselstroomverliezen in de supergeleidende veldwikkeling. Het nive-au van deze AC verliezen wordt bepaald door combinatie van 2D transiente FEM modellen die het magnetische veld bepalen in combinatie met analytische modellen die de wisselstroomverliezen bepalen. De resultaten laten zien dat de wisselstroomverliezen die geproduceerd worden door de ijzeren tanden erg laag kunnen zijn en daarmee is deze topologie geschikt uit oogpunt van beperking van wisselstroomverliezen.

REDUCTIE VAN KORTSLUITKOPPEL

SCSG's hebben een grotere magnetische luchtspleet dan conventionele generatoren door de ruimte benodigd voor een cryostaat of het gebruik van niet-magneti-sche kern materialen. Het gevolg hiervan is dat de inductantie lager wordt en dat hierdoor het koppel als gevolg van een kortsluiting meer dan 10 keer zo groot kan worden als het nominale koppel. Een dergelijk koppel is te groot voor een wind turbine constructie. Drie methoden om het kortsluitkoppel te beperken worden onderzocht. De eerste is het gebruik van een elektromagnetische afscherming tussen de veldwikkelingen en het anker. De tweede methode is het gebruik van ijzeren in plaats van niet-magnetische tanden in de stator. De derde methode is segmentatie van de ankerwikkeling met behulp van meerdere vermogensomvormers. 2D transient FEM modellen worden gebruikt om het koppel gedurende een kortsluiting in onbelaste toestand te bepalen. De eerste en de tweede methode zijn niet effectief. De derde methode die gebruik maakt van segmentatie van de ankerwikkeling is in staat om effectief het kortsluitkoppel te verlagen voor alle vier ontwerpen van de generator, wanneer een segment wordt kortgesloten, ervan uitgaande dat de segmenten onafhankelijk van elkaar zijn in het FE model. Verhoging van het aantal segmenten verlaagt het kortsluitkoppel; vier segmenten beperken het kortsluitkoppel tot minder dan drie keer nominaal koppel.

HET POTENTIEEL VAN GEDEELTELIJK SUPERGELEIDENDE GENERATOREN

Door het uitvoeren van een vergelijking tussen 10 MW SCSG en PMSG blijkt dat SCSG's nog niet competitief zijn als er op basis van de energie kostprijs ontworpen word. Er moet worden gekeken naar specifieke voordelen van SCSG welke ze interessant kunnen maken voor de windturbine industrie. Het potentieel van gedeeltelijke SCSG voor 10 MW direct aangedreven windturbines is uitgevoerd door hun prestaties voor verschillende bekrachtigings-stromen te onderzoeken. De 12 topologien zijn vergeleken met elkaar op basis van onder andere genomen: kracht-dichtheid en rendement. Om aantrekkelijk genoeg te zijn moeten SCSG's een significant hogere krachtdichtheid en rendement hebben dan PMSG, een PMSG heeft typisch een krachtdichtheid van 53 kPa en een rendement van 96%. Als voorbeeld is onderzocht voor 4 topologien wat de impact is op de bekrachtiging is om de kracht-

dichtheid te verdubbelen en een rendement van 98% te bereiken. Om dit te bereiken hebben de 4 topologien een bekrachtiging van 200 to 500 kAt (Ampere-turns) nodig met een bekrachtigings-stroomdichtheid van 2 A/mm2. Des te meer ijzer er gebruikt wordt in het ontwerp des te makkelijker het doel bereikt kan worden. Door de maximale magnetische fluxdichtheid in de supergeleidende veldwikkeling te onderzoeken, kan er een geschikte supergeleider gekozen worden op basis van hun stroomdichtheid ontwerpspecificatie. Uitkomst is dat hoge en lage temperatuurgeleiders aan de eisen kunnen voldoen voor de meeste van de vier topologien. MgB_2 supergeleiders zijn haalbaar in een volledig ijzer kern topologie met uitspringende polen, echter is een temperatuur van 10 K noodzakelijk.

▽ ▽ ▽

In dit proefschrift wordt er vanuit perspectief van het het elektromagnetische ontwerp gewezen op een richting om de haalbaarheid van SCSG in grote direct aangedreven windturbines te vergroten.

Als het doel een zo laag mogelijke LCCoE is, dan is een generatorontwerp gebaseerd op een ijzer-kern meer haalbaar dan andere topologien en is de noodzakelijke lengte van supergeleidend materiaal korter. De ontwerpen op basis van ijzerkernen zijn het best haalbaard en de wisselstroomverliezen zijn op een acceptabel niveau. Als een laag generator gewicht ook een eis is dan moeten de concepten met meer niet-magnetisch materiaal in overweging genomen worden als de supergeleidende draden een stuk goedkoper worden en veel hogere stroomdichtheden kunnen halen.

Op dit moment heeft een SCSG in de LCCoE analyse geen voordeel boven een PMSG. Om supergeleiding aantrekkelijk te maken voor de windturbine industrie moet de krachtdichtheid en het rendement veel beter zijn dan een permanent magneet generator. De voordelen van een hoger rendement en hogere krachtdichtheid kunnen de nadelen van hogere kosten en de cryogene koelingcompense-ren.

Om competitieve krachtdichtheden en rendementen te halen moet de sterkte van de bekrachtiging van de veldwikkeling naar een hoger niveau gebracht worden. Om dit mogelijk te maken zijn LTS en HTS beter kandidaten dan MgB_2 draden op dit moment. Daarbij zijn ontwerpen gebaseerd op ijzerkernen beter haalbaard dan andere topologien om de hoge krachtdichtheden en rendementen te halen. In het bijzonder de ontwerpen met een volledig ijzeren kern. De kortsluitkoppels kunnen gereduceerd worden door de generator op te delen in meerdere segmenten en door ieder segment zijn eigen vermogensomzetter te geven.

Dit is niet de enige ontwerprichting. Echter houdt deze ontwerprichting rekening met de hoofdfactoren van de huidige elektromagnetische ontwerpmethodologie. Prototypes kunnen gebouwd worden volgens deze richtlijn om deze technologie te valideren en te demonstreren. Dit proefschrift helpt mee in de ontwikkeling

en opbouw van kennis voor grote direct aangedreven SCSG windturbine generatoren. De huidige stand van de techniek in het vakgebied wordt in dit proefschrift samengevat. De ontwikkeling gaat verder, de techniek zal steeds meer volwassen worden om een bewezen compacte, lichtgewicht, hoog rendement en goedkope SCSG generatoren te ontwikkelen.

1

INTRODUCTION

1

1.1. BACKGROUND

THe conservation of fossil fuels and the need for reducing green house gas emission accelerates the development of renewable energy. Wind energy, as a promising renewable energy source, is developing rapidly nowadays. Onshore wind energy has been extensively developed in the last two decades. A few countries with a vast land area, such as China, have established large-scale wind farms inland [1]. A large number of wind turbines of 1-3 MW form such wind farms. In those with small land areas, such as European countries, the capacity for onshore wind farms is limited, which are greatly constraining the development of onshore wind energy utilization in such countries [2].

For this reason, offshore wind has been drawing increasing attention in European countries [3], [4]. In offshore regions, particularly the North Sea, wind resources are superior to those of onshore regions, as illustrated in Fig. 1.1. The naturally vast area of ocean makes offshore wind energy quite promising to European countries around the North Sea. Denmark, Norway, UK, Netherlands and Germany are building and testing offshore wind farms in the North Sea. An advanced high voltage direct current (HVDC) network is also under development to connect those offshore wind farms to inland power grids [5].

However, utilization of offshore wind energy brings about much higher costs in installation, maintenance and repair due to long distances between a wind farm and its neighboring land. Harsh offshore environment elevates the difficulties and complexities. As a result, the costs of building and maintaining an offshore wind farm can be several times higher than those of an onshore wind farm.

An effective way to lower such costs is to decrease the number of individual wind turbines in a wind farm. Then the major costs of a wind farm, expensive foundations and grid connections, can effectively be limited. To maintain the same capacity of the wind farm, an individual wind turbine must have a very large power rating. Most onshore wind turbines are in the range of 1-3 MW. An offshore wind turbine needs to be much larger to be competitive. A large wind turbine is more expensive than a smaller one regarding the capital expenditure (CAPEX) of the turbine itself. However, the costs of installation, maintenance and repair of a wind farm of large wind turbines are thought to be reduced when the number of wind turbines effectively decreases. As a whole, the cost per unit energy production can be reduced, which is highly desired in wind energy industry.

The trend of the power rating of a single offshore wind turbine, as illustrated in Fig. 1.2, proves that offshore wind turbines are becoming increasingly larger in recent years. The deployment of 4-6 MW turbines seen in 2015 will be followed by the gradual introduction of 6-8 MW turbines closer towards 2018 [7]. In industrial

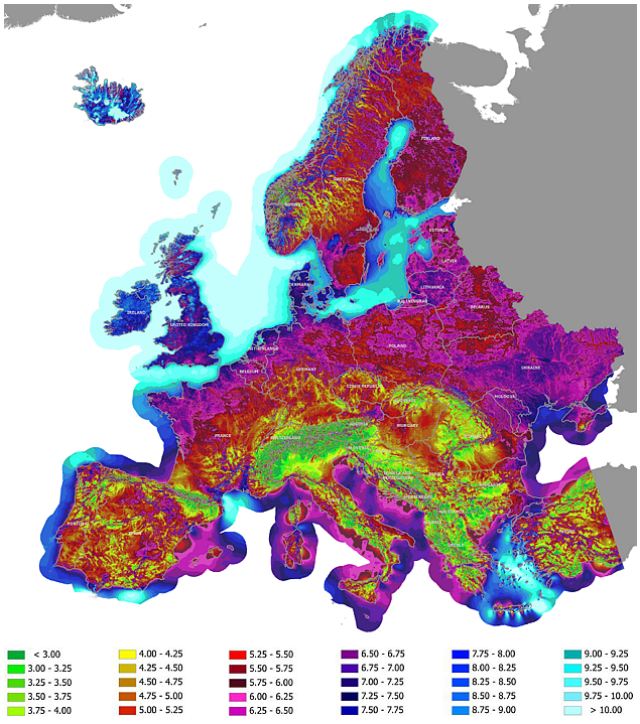

Figure 1.1: Annual mean wind speed in Europe at 80 m high. Reproduced from [6].

practices, Siemens is commercially supplying 8 MW offshore wind turbines [8] and Vestas has also increased the power level of a single wind turbine to 8 MW [9].

Large wind turbines (e.g. over 6 MW) put forward new issues with drive trains. A drive train in a wind turbine converts the kinetic energy from wind into electrical energy. Conventional drive trains for wind turbines below 6 MW are categorized into two main types. One is a high-speed or medium-speed generator integrated with a gearbox. This gearbox is located between the faster generator rotor and the slower aerodynamic rotor (i.e. the wind turbine rotor with three blades). This geared drive train mainly contains the following concepts:

• A high speed doubly-fed induction generator with a partially rated power converter. A three-stage gearbox is used.

• A high speed synchronous generator with a fully rated power converter and a three-stage gearbox is used. A modification is the medium speed synchronous generator with a fully rated power converter and a single or double stage gearbox is

1

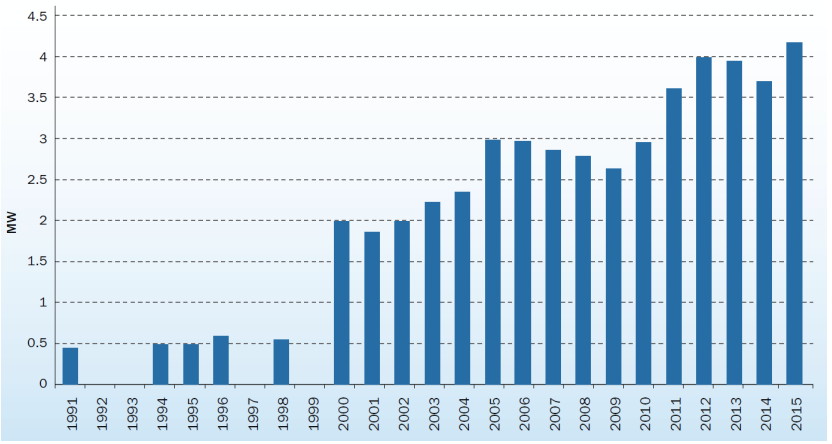

Figure 1.2: Average power rating of offshore wind turbines newly installed per year in Europe. [7]

then used.

The other drive train type is simply a low-speed synchronous generator directly connected to the low-speed aerodynamic rotor without a gearbox. Both the rotors rotate at the same speed. A fully rated power converter is used. This type is called direct drive and two generator types are primarily employed to it. One is electrically excited synchronous generator (EESG) and the other is permanent magnet synchronous generator (PMSG). Using fully rated converters decouples the generator and the power grid, and enables the electrical output to comply with the latest grid codes.

For small and medium wind turbines in onshore applications, these two drive trains are both extensively employed. Geared generators are compact and lightweight due to high speed operation. Direct-drive trains are, however, expected to be more reliable because of the removal of the less-reliable gearbox [10]. The resulting size and weight of an onshore direct-drive generator are not problematic for the wind turbine support, installation and transportation.

In offshore wind energy conversion, when larger wind turbines (above 6 MW) are desired for a low cost of energy, geared drive trains encounter a challenge with the large and expensive gearbox. Such big gearboxes are not easy to be manufactured and their reliability is of a question. Direct-drive generators, such as EESGs and PMSGs, would become very large in size due to low rotational speeds (e.g. 10 rpm for a 10 MW wind turbine). Larger sizes usually mean higher costs. Since EESGs are usually less efficient than PMSGs due to resistance in the excitation circuit, the

PMSGs are of more interest in the design of direct-drive wind turbines. However, PMSGs need a large amount of rare-earth materials, i.e. permanent magnets. Since the natural resources of rare-earth materials are limited, the fact of markets shows that permanent magnets (PMs) are not cheap and their price is hardly predictable. Due to such uncertainty of PM costs, European countries are looking for alternatives which can replace permanent magnets or reduce the use of permanent magnets for wind energy conversion with large wind turbines.

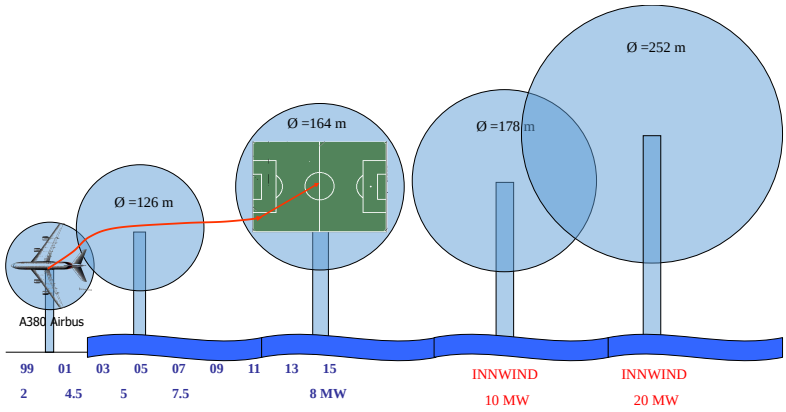

Figure 1.3: Trend of wind turbine sizes, including the expectation by the INNWIND.EU project. The most left turbine is the largest inland, which has a power below 4 MW and was established in around 2000. Then the record of sizes is being broken by offshore wind turbines.

The INNWIND.EU project funded by the European seventh framework (FP7) started in 2012 and has been studying two promising candidate generator systems which could become such alternatives [11]. One of the generator systems is pseudo direct drive (PDD) generator system and the other is superconducting generator system. Both are intended for 10-20 MW direct-drive wind turbines whose sizes are sketched in Fig. 1.3.

A PDD generator applies a magnetic gearbox for contactless torque transmission [12] so that the generator can be made small, lightweight and reliable, [13, 14]. This generator system is being studied, designed and demonstrated by Magnomatics Ltd. and the University of Sheffield. A superconducting generator makes use of the large current capability of superconducting materials to produce high magnetic fields so that the generator can be made small, lightweight and efficient [14–16]. Within the INNWIND.EU project, the superconducting generator system is being studied, designed and demonstrated by DTU Wind Energy, Delft University of Tech-

nology, SINTEF and Siemens Wind Power. The INNWIND.EU project aims at finding a promising alternative for large offshore wind turbines and considers these two generator systems.

1.2. MOTIVATION

Superconducting machines have been studied for several decades. Besides theoretical studies, a few laboratory or industrial practical demonstrations were also designed and operated, especially for military ship propulsion [17, 18]. These studies focused on proving the technical feasibility of superconducting machines. However, successful industrial applications for power engineering are still far away. The challenges for industrial application involve many aspects, such as cryogenic cooling, performance of large-scale superconducting wires, mechanical construction and costs. Applying superconducting generators in wind energy conversion systems has drawn attention. This is because this generator has potential in large offshore wind turbines to reduce the size and weight of the tower head.

Theoretical studies and ship propulsion experiences on superconducting machines may not be directly transplanted to wind energy conversion, since they may have quite different requirements. First of all, wind energy industry requires a low cost of energy. Secondly, a wind turbine itself puts mechanical and spatial constraints onto the drive train. Thirdly, offshore wind energy conversion requires a high reliability and availability. These special issues challenge the drive train and particularly the performance of the superconducting generator.

The performance of an electrical machine significantly depends on the electromagnetic design. However, academia and industry have not yet found or agreed on a dominant design concept. There are many trade-offs in the design process depending on a specific application and its requirements. For example, military or aerospace engineering may not very much care about costs but size, weight and efficiency are essential. As a result, such applications tend to use lightweight but costly materials and designs.

Unlike in military applications, wind energy conversion rigorously requires low costs and high energy production which can facilitate commercialization. Small size and weight of a generator are advantages as expected by both the academia and commercial companies [15, 16, 19–22]. However, size and weight may become less important (but still important) in large offshore wind turbines. Those electromagnetic designs of generator which result in low costs per unit energy production are preferred. Therefore, they should be found out in the first place.

Despite the intention of low costs of energy, there are still many different electromagnetic design concepts being proposed and developed. AMSC [21], General Electric (GE) [20] and the Suprapower project [23] proposed designs using HTS (BSCCO

or YBCO), LTS (NbTi) and MgB_2, respectively. Moreover, GE employed a retrofit stator core with steel laminates but a novel non-magnetic rotor core for the superconducting field winding. Suprapower proposed conventional salient iron rotor poles but introduced non-magnetic teeth to the stator core. Keysan designed transverse-flux superconducting generators which are quite different from conventional radial-flux ones [24]. In addition to all the above mentioned partially superconducting concepts, AML Superconductivity and Magnetics is developing a fully superconducting design [22] in which both the field and armature windings are superconducting [25, 26]. These concepts have formed a vast range of electromagnetic design possibilities.

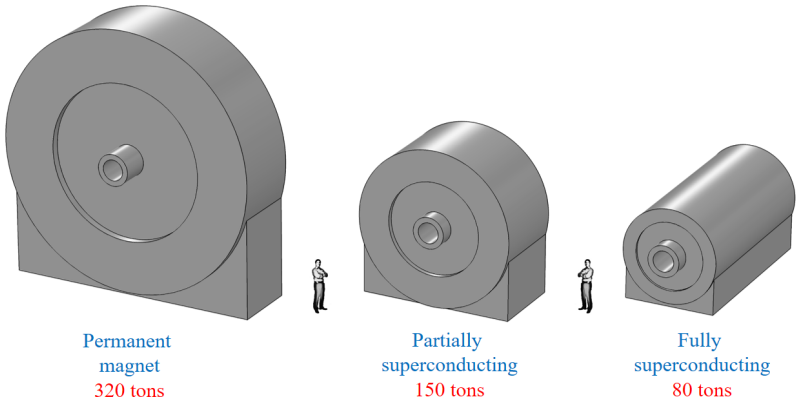

Figure 1.4: Size and weight reduction by using superconducting generators for 10 MW direct-drive wind turbines. The permanent magnet generator is estimated based on [27]. The partially superconducting generator is estimated based on [20]. The fully superconducting is estimated by [28].

An electromagnetic design of a superconducting machine usually starts from topology selection, which defines the combination of ferromagnetic and non-magnetic in the machine cores. Using ferromagnetic cores or not can make the cost, efficiency, size and weight of a generator quite different [29, 30]. Generally speaking, the design of a superconducting machine is made by integrating a particular topology with currently available superconductors. Such a design is capable of certain performance for evaluation. For offshore wind energy conversion, we evaluate different designs by the cost of energy.

Unlike such forward thinking from design to performance, a design can also be made and evaluated through reverse thinking from required performance to design.

This way of thinking is enabled due to the fact that the superconductor technology is still developing fast. A design based on the present superconductor technology will probably be out of date soon in near future. Hence, we may not limit ourselves to the currently available superconductors. Instead, we can set the values of desired performance indicators, such as a specific size, weight, efficiency or cost, for the application. Then, we find out the required design parameters and suitable or potentially suitable superconductors to achieve such high performance. This approach is expected to reveal the potential performance of a superconducting generator for future.

Accompanying the general electromagnetic design, i.e. topology selection, AC losses are always an issue uniquely with superconductors. Some generator designs may produce excessive AC losses in the superconducting winding due to ripple magnetic fields from winding distribution or slotting effects [31, 32]. Such losses either reduce the efficiency or challenge the cooling system. Hence, an electromagnetic design should also be evaluated from the perspective of AC losses.

Another unique challenge for designing a superconducting machine is the high short circuit torque due to a large magnetic air gap. The peak torque during a short circuit (at the generator terminal) could reach as high as more than ten times the rated torque [33], which is way beyond the mechanical limit usually designed for a wind turbine. This problem must be addressed. Otherwise, application of superconducting generators in wind turbines will stay infeasible.

1.3. RESEARCH OBJECTIVE

IN line with the background and motivation, the objective of this thesis is to *"Provide insights and solutions from the perspective of electromagnetic design to increase the feasibility of superconducting generators for large wind turbines."*

To achieve this objective, this thesis will investigate the following four aspects of feasibility:

- Costs,
- AC losses,
- Short circuit torque, and
- Performance, i.e. shear stress and efficiency,

These four aspects greatly determine the feasibility level of superconducting generators applied in large wind turbines. Apparently, electromagnetic design is the backbone of this research. However, we cannot overlook the role that mechanical and cryogenic cooling designs play in such a complicated multi-physical system. Appropriate considerations will be taken to form realistic electromagnetic designs.

1.4. RESEARCH QUESTIONS

According to the research objective, four research questions must be answered in this thesis:

•Q1: *Which topologies result in the lowest cost of energy, based on currently available superconductors?* The purpose of answering Q1 is to *"find out superconducting generator topologies suitable for wind turbine application and provides insights to selection of topologies for superconducting generator design"*.

•Q2: *What are the levels of AC losses in the superconducting winding of different electromagnetic designs due to ripple magnetic fields? Are the AC losses acceptably small or not?* The purpose of answering Q2 is to *"evaluate the technical feasibility of AC loss levels in superconductors of different electromagnetic designs"*.

•Q3: *How can the short circuit torque be effectively suppressed by electromagnetic design?* The purpose of answering Q3 is to *"assess that the short circuit torque of a superconducting generator can be sufficiently small for mechanical construction of a wind turbine"*.

•Q4: *How competitive is a superconducting generator compared with a permanent magnet generator?* The purpose of answering Q4 is to *"evaluate the feasibility of performance indicators of a superconducting generator when comparing it to a technically mature competitor"*.

•Q5: *What is the potential of a superconducting generator for large wind turbines? What are the design parameters and suitable superconductors required to achieve high generator performance?* The purpose of answering Q5 is to *"reveal the prospect of superconducting generators for wind energy conversion"*.

1.5. THESIS LAYOUT

Based on the research questions, this thesis has a structure shown in Fig. 1.5 and is divided into seven chapters. Chapters 3-7 answer the four research questions in the order which constitute the scientific contributions of this thesis.

• Chapter 2 introduces superconductivity and describes how a superconducting generator is integrated into a large offshore wind turbine.

• Chapter 3 overviews possible topologies for a 10 MW superconducting machine and compares them by the criterion of cost of energy. Chapter 3 answers Q1.

• Chapter 4 models the AC losses in the superconducting winding due to ripple magnetic fields and evaluates the loss level for different 10 MW superconducting generator designs. Chapter 4 answers Q2.

• Chapter 5 models the short circuit torque of 10 MW superconducting generators and then presents and evaluates the methods to suppress the excessive short circuit torque. Chapter 5 answers Q3.

• Chapter 6 compares 10 MW superconducting generators and permanent magnet generator under the same design and optimization methods and the same operating conditions. Chapter 6 answers Q4.

• Chapter 7 reveals the potential performance of 10 MW superconducting generators and the requirements to design parameters and superconductors to achieve high performance. Chapter 7 answers Q5.

• Chapter 8 concludes this thesis and gives recommendations for future work.

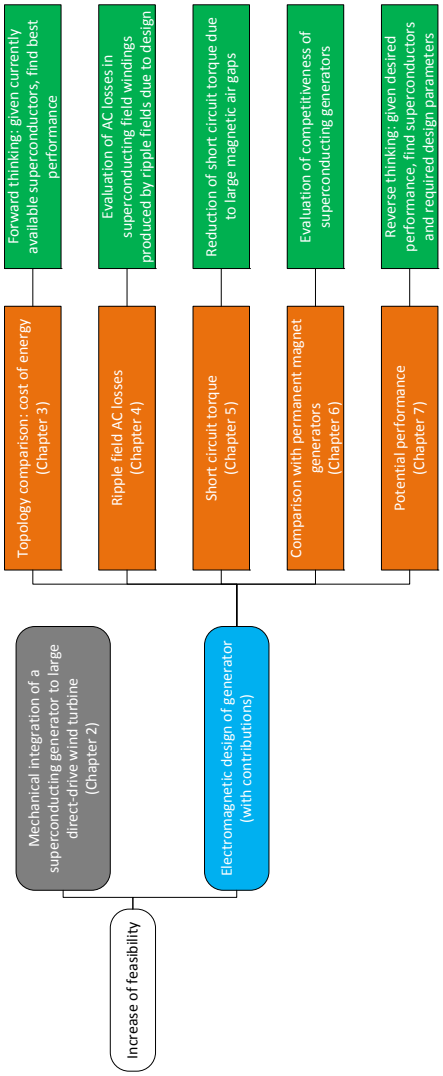

Figure 1.5: Thesis structure.

2

SUPERCONDUCTING DRIVE TRAIN FOR LARGE WIND TURBINES

2.1. INTRODUCTION

Superconducting machines take advantage of the large current density capability of superconductors for exciting high magnetic fields. This chapter starts with introducing basic physical properties of superconductor. Then the basic structure of a superconducting machine is described and its fundamental properties, such as machine type, partially or fully superconducting, radial or axial flux and cryogenic cooling method, are reviewed for wind turbine applications. In the end, integration of a superconducting generator to a 10-20 MW direct-drive wind turbine nacelle concept is introduced, followed by an brief overview of the other 10 MW up-to-date superconducting nacelle concepts. The objective of this chapter is to depict a superconducting drive train and its integration into a large wind turbine.

2.2. INTRODUCTION TO SUPERCONDUCTIVITY

Superconductivity is a phenomenon where some materials exhibit no electrical resistance below certain cryogenic temperatures. It was discovered on 8 April, 1911 by Heike Kamerlingh Onnes, who was studying the resistance of solid mercury at cryogenic temperatures using the recently produced liquid helium as a refrigerant. At the temperature of 4.2 K, he observed that the resistance abruptly disappeared [34, 35].

Superconductors have two distinct properties: zero resistance and Meissner effect. Basically, all superconductors can be divided into two basic types: Type-I and Type-II superconductors. Alternating currents or magnetic fields produce losses in superconductors. Striped superconductors are anisotropic, and their $B - J$ critical characteristics and AC losses depend on the direction of the applied magnetic field.

2.2.1. ZERO RESISTANCE

The first property of superconductors is zero resistance. The temperature for achieving zero resistance for a superconductor has become increasingly higher over the last 100 years, from 4.2 K to above 100 K and even 203 K (H_2S at 150 GPa pressure). The material which can be superconducting has also become more various, from mercury to, for instance, NbTi, YBaCuO, MgB_2 and H_2S. The coolant for cooling superconductors originates from liquid helium and now goes to liquid nitrogen and even liquid tetrafluoromethane (CF_4). The time line of the development of superconductors is shown in Fig. 2.1.

Zero resistance of a superconductor is true under the condition of unchanged currents and magnetic fields. However, losses will occur if a superconductor is with changing currents or magnetic fields. Thus, strictly speaking, we should say that superconductors have zero DC resistance for the sake of considering their AC resis-

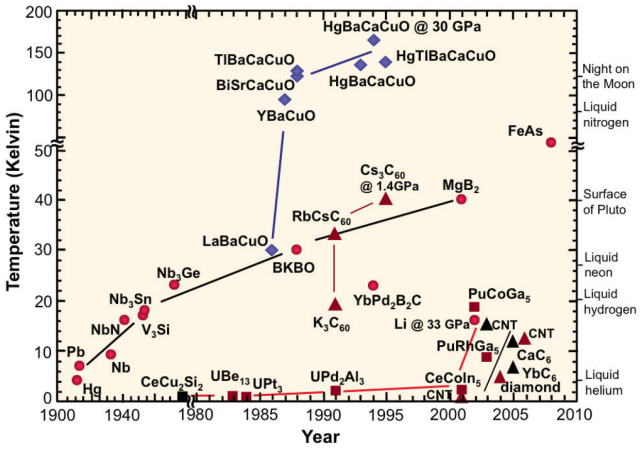

Figure 2.1: Timeline of the development of superconductors from 1911 to 2010 [36]. The boiling point of different coolants is also indicated. In 2015, it was discovered that sulfur hydride (H_2S) becomes superconducting at 203 K at a high pressure of 155 GPa [37].

tance.

2.2.2. MEISSNER EFFECT AND TYPE-I SUPERCONDUCTORS

In 1933, Walther Meissner and Robert Ochsenfeld discovered the Meissner effect, which is the second property of superconductors [38]. This effect shows that the magnetic field is not fixed inside a superconductor when it is cooled down through the critical temperature. Instead, the magnetic field is forced out of the material. The magnetic field is suddenly expelled from the center of the material, forcing the field lines to run around the superconductors, as illustrated in Fig. 2.2. When the material becomes superconducting, screen currents occur near the surface of the material, screening the inside from the outside magnetic field [39].

This effect occurs in Type-I superconductors which suddenly lose their superconducting properties once the field strength reaches above a certain magnetic field strength H_{c1} [40]. This type of superconductivity is normally exhibited by pure metals, e.g. aluminum, lead, and mercury.

2.2.3. TYPE-II SUPERCONDUCTORS

The superconductors currently applied in electrical apparatus, e.g. NbTi, Nb_3Sn, MgB_2, BSCCO and ReBCO, are all Type-II superconductors, which are capable of higher magnetic fields compared to Type-I superconductors [40, 42].

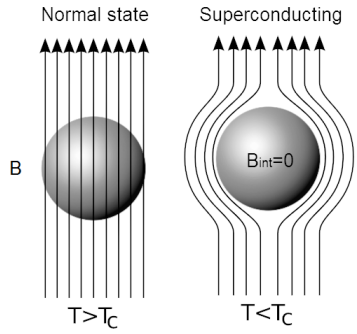

Figure 2.2: Meissner effect in a superconductor. The conductor on the left is in the normal state (not superconducting) when it is above its critical temperature. The conductor on the right is in the superconducting state when it is below its critical temperature and the magnetic field inside the conductor is zero. The external magnetic field is below H_{c1} in the both cases. Reproduced from [41].

Type-II superconductors behave the same as Type-I superconductors below H_{c1}. But at a higher magnetic field strength, the flux lines gradually penetrate the superconductor whose superconducting properties remain. When the magnetic field strength increasingly reaches above a value H_{c2}, the superconducting properties are lost. The region between H_{c1} and H_{c2} can be considered as a transition from no magnetic field penetration to full penetration. Although the flux lines seem to enter the superconductor, they are still shielded from the superconducting parts by current vortices. This transition region is called a mixed state. The mixed state makes Type-II superconductors usable since such superconductors can withstand higher magnetic fields. All the states of Type-I and Type-II superconductors are depicted in Fig. 2.3b.

2.2.4. CHARACTERISTICS OF A SUPERCONDUCTOR

$E-J$ CHARACTERISTIC

A superconductor can be characterized by its $E-J$ characteristic, where E is the electric field and J is the current density. This characteristic measures the resistance in a superconductor when a certain current density is applied. In a limited range (below the current density for a flux flow state [44]), an $E-J$ characteristic can be modeled by the power law:

$$E = E_c(\frac{J}{J_c})^n, \tag{2.1}$$

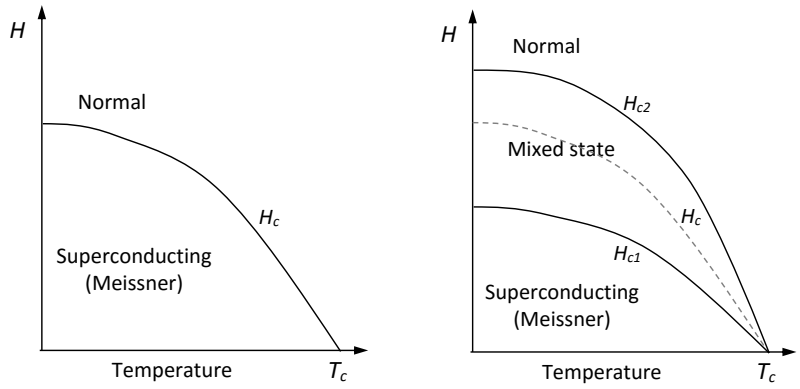

(a) Type-I (b) Type-II

Figure 2.3: Phase diagrams for Type-I and Type-II superconductors with the superconducting, mixed and normal states indicated. Reproduced from [43].

where $E_c = 1\ \mu$V/cm, J_c is the critical current density when E reaches E_c, and n is the power value which indicates how fast a superconductor transits from the superconducting state to the normal state. To illustrate the power law, a few measured $E-J$ characteristics of a superconductor are plotted in Fig. 2.4.

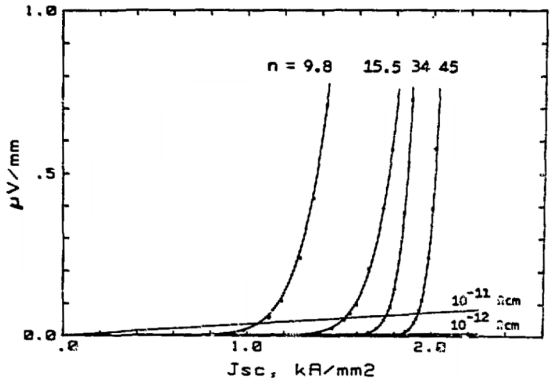

Figure 2.4: $E-J$ characteristic of multi-filamentary NbTi superconductor at $T = 4.23$ K and $B = 5$ T. High (low) values of n are the results of large (small) diameter filaments [45].

CRITICAL SURFACE

A superconductor is only superconducting within its critical surface, which is constrained by current density J, temperature T and magnetic flux density B, as illustrated in Fig. 2.5. Superconductivity exists within the volume bounded by the surfaces bordered by the functions: $f_1(T=0,J,H)$, $f_2(H=0,J,T)$ and $f_3(J=0,H,T)$. Each superconductor has its unique critical surface. A superconductor operating outside its critical surface leaves its superconducting state. Thus, most designs with superconductors (except for applications like a fault current limiter (FCL)) must ensure that all the superconductors are operating within this limit enclosed by critical current density J_c, critical temperature T_c and magnetic flux density B_c.

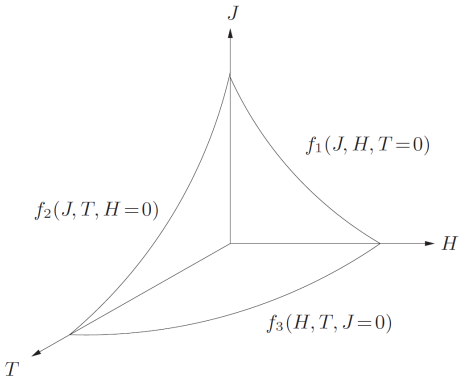

Figure 2.5: Critical surface of a typical Type-II superconductor [41].

When temperature is fixed, we can obtain a $B-J$ characteristic at this temperature. The $B-J$ characteristic of different superconductors at 4.2 K is plotted in Fig. 2.6. A series of $B-J$ characteristics of a certain superconductor at different temperatures is practically useful especially when the operating point of the superconductor is determined.

2.2.5. ORIGIN OF LOSSES IN A SUPERCONDUCTOR

As the first property, a superconductor has zero DC resistance. Thus, DC losses do not exist in a superconductor. However, AC losses can be produced in a Type-II superconductor due to the penetration of magnetic fields. In the penetration depth, an electric field is excited by a changing magnetic field by

$$\nabla \times E = \frac{\partial B}{\partial t}, \tag{2.2}$$

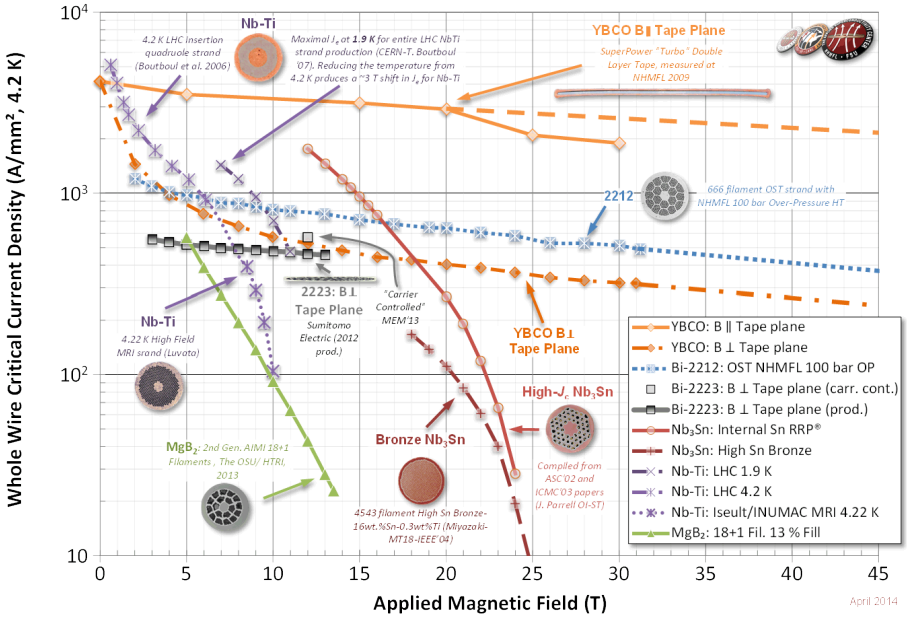

Figure 2.6: Critical characteristics of different superconductors at 4.2 K. Bi-2212 and Bi-2223 are both 1G HTS (BSCCO) with different wire architectures. YBCO is 2G HTS (ReBCO). $B \perp$ and $B \parallel$ are the magnetic fields perpendicular and parallel to the longer side of a superconductor (tape plane), respectively. LHC stands for large hadron collider. MRI stands for magnetic resonance imaging. Reproduced from [46].

and the resistive loss (Joule loss) per unit volume p is then produced by

$$p = J \cdot E. \tag{2.3}$$

where J is the current density flowing in the penetration depth of the superconductor, as illustrated in Fig. 2.7. This current density reaches as high as the critical value J_c according to Eq. (2.1). The AC loss due to this mechanism is called hysteresis loss. The hysteresis loss can be reduced by decreasing the dimensions of the superconductor [47].

Furthermore, a superconducting wire consisting of multiple superconducting filament is subject to coupling losses. These filaments are embedded in a normal-metal matrix. Eddy current losses are produced in the matrix by alternating magnetic fields. Besides, alternating magnetic fields produce electric fields which drive currents to flow in both the filaments and the matrix, as illustrated in Fig. 2.8. These

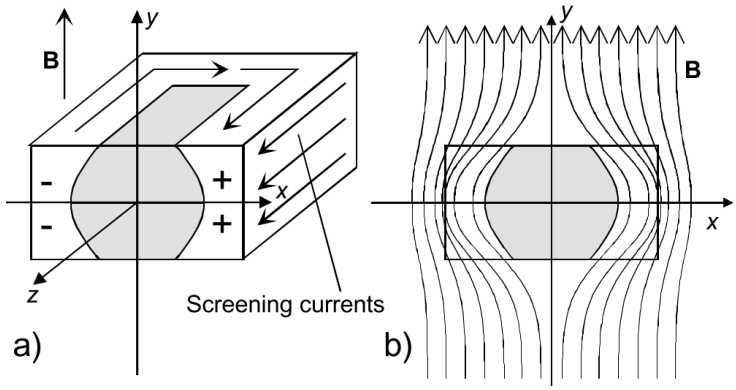

Figure 2.7: Cross-section of a superconductor in a changing external magnetic field. The screening currents in the white region shield the interior (gray) from the magnetic field. [47]

currents couple different filaments through the matrix at the end of the filaments. In the filaments, the current flows without resistance and is therefore large. In the matrix, the same large current encounters the resistance of the matrix and produces high losses. The coupling currents can be decreased by applying a twist to the filaments, by reducing the dimension of the wire or by increasing the resistivity of the matrix material [47].

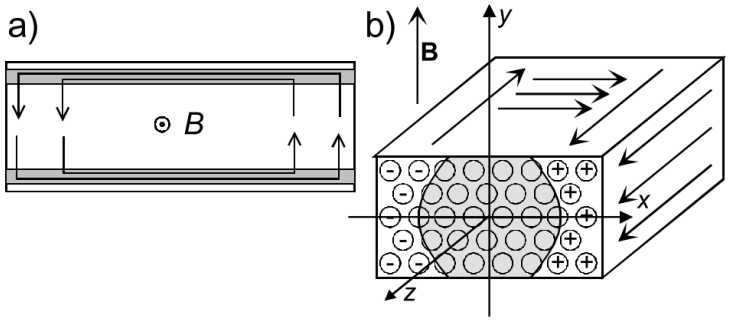

Figure 2.8: Coupling currents between non-twisted filaments in a composite conductor [47]. In (a), the filaments are shown in the gray and the arrows are coupling currents.

2.2.6. ANISOTROPY

A round superconductor has isotropic properties which are independent of the direction of applied magnetic fields. A striped superconductor is, however, anisotropic. The anisotropy of a striped superconductor especially affects the $B - J$ critical characteristic. A perpendicular magnetic field lowers the critical current density compared to a parallel one of the same value [48, 49] as shown in Fig. 2.9. This effect can also be observed in striped wires as shown in Fig. 2.6 (Bi-2223 and YBCO). In this figure and by convention, $B \perp$ and $B \parallel$ are the magnetic fields perpendicular and parallel to the longer side of a superconductor, respectively. In addition, AC losses of a single striped superconductor or a striped wire of multiple superconductor filaments are also dependent on the direction of the magnetic field [50]. The significant effect of anisotropy on the performance of a striped superconductor must be taken into account in the design process of a superconducting apparatus.

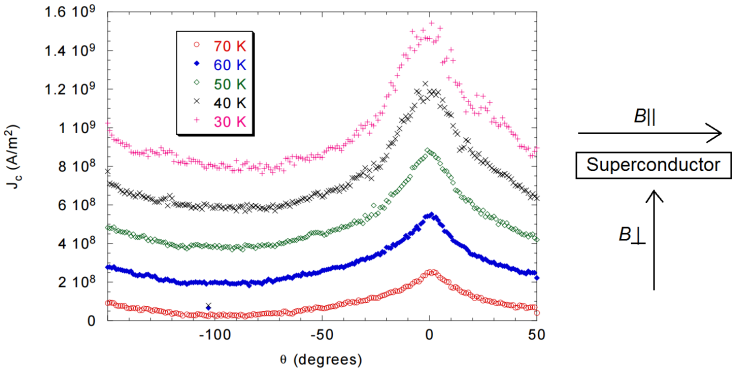

Figure 2.9: Critical current density measurements performed on a sample YBCO film at temperatures of 30-70 K. The data was obtained in a magnetic field of $B = 1$ T. At $\theta = 0$ ($\theta = -90°$), and the magnetic field is parallel (perpendicular) to the striped superconductor. Reproduced from [49].

2.2.7. OVERVIEW OF SUPERCONDUCTOR TYPES

Superconductors can be divided into three categories according to the operating temperature: low temperature superconductor (LTS), magnesium diboride (MgB_2) and high temperature superconductor (HTS).

LTS operates at liquid helium temperatures (4 K) or even lower temperatures. Typical LTS's are niobium-titanium (NbTi) and niobium-tin (Nb_3Sn). NbTi is an alloy and Nb_3Sn is a compound. Wires of either NbTi or Nb_3Sn are multi-filamentary.

MgB_2 is superconducting below $T_c = 39$ K and is expected to operate at 10-20 K, a temperature range between 4 K (liquid helium) and 65 K (liquid nitrogen). MgB_2

wires are multi-filamentary.

The term of high temperature means that all HTS has critical temperatures over the boiling point of nitrogen (77 K). HTS is further divided into the 1st generation (1G) HTS (i.e. BSCCO) and the 2nd generation (2G) HTS (i.e. ReBCO). The composition of BSCCO is $Bi_2Sr_2Ca_{n-1}Cu_nO_{2n+4}$. Typical BSCCOs are Bi-2212 ($n = 2$) and Bi-2223 ($n = 3$). Regarding the 2G HTS, the industry currently uses Rare Earth compounds (Yttrium, Samarium, Neodymium, Gadolinium) with Barium-Copper-Oxide (BCO) to surpass the 1G HTS in electrical performance but at higher cost. BSCCO wires are multi-filamentary while ReBCO wires are generally coated.

Table 2.1 summarizes the most popular commercial superconductors and their properties and typical applications. The cross-section of wires consisting of these superconductors is sketched in Fig. 2.10.

Table 2.1: Properties of most popular commercial superconductors.

Category	LTS		MgB_2	HTS	
Composition	NbTi	Nb_3Sn	MgB_2	BSCCO (1G)	ReBCO (2G)
Critical temp.	9.2 K	18 K	39 K	85-110 K†	92 K
Wire architecture	MF††	MF††	MF††	MF††	coated
Magnetic field level	high		low, medium	medium, high	
Applicable temp.	≤4.2 K		10-20 K	20-77 K	
AC loss level	medium	medium	medium	medium	high
Wire cost	low	low	medium	high	high
Application	MRI, accelerator		machine	power cable, machine, maglev, FCL	

†85 K: Bi-2212, 110 K: Bi-2223.

†† Multi-filamentary.

2.2.8. SUPERCONDUCTORS UNDER CONSIDERATION

At present, LTS is mainly used in high-field application such as magnetic resonance imaging (MRI) [52] and accelerator magnets [53, 54] cooled by liquid helium. GE has proposed a 10 MW generator design using NbTi at 4.2 K, which has established a concept for LTS generators [20]. HTS cooled by liquid nitrogen at 77 K is mainly used in power cables [55] and fault current limiters (FCLs) [56]. When it comes to generators, HTS usually has to be cooled down to below 40 K to achieve good performance. Furthermore, HTS materials are currently rather expensive (one order more expensive than LTS and MgB_2). MgB_2 seems to lie in a moderate position. It requires a temperature of 10-20 K to make a generator with decent performance but it is much cheaper than HTS. Although MgB_2 has shortcomings such as low magnetic

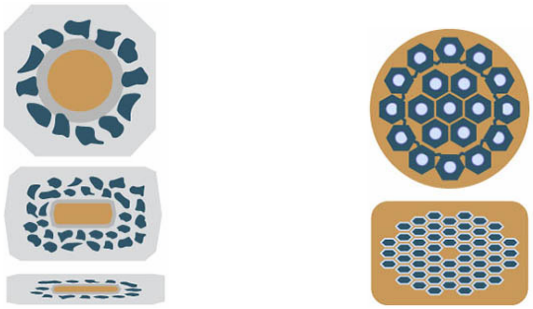

(a) MgB_2 (b) LTS

(c) BSCCO (d) ReBCO

Figure 2.10: Cross-section sketch of LTS (NbTi or Nb_3Sn), MgB_2 and HTS (1G: BSCCO and 2G: ReBCO). Except that ReBCO is coated superconductors, BSCCO, MgB_2 and LTS are all multi-filamentary superconductors. Coated superconductors are in strip shape while multi-filamentary ones can be round or striped. [51]

field capability and hardness of the material, it is considered as a good starting point to design a superconducting generator for wind turbines. In this thesis, we mainly use MgB_2 for the electromagnetic study for designing a superconducting generator. LTS and HTS will be discussed in Chapter 7 when we look for the potential performance of a partially superconducting generator.

The MgB_2 wire used in this thesis is fabricated by Columbus Superconductors [57]. The cross-section of the wire is depicted in Fig. 2.11. A single wire has 19 MgB_2 filaments embedded, and arranged approximately elliptically, in a nickel matrix. The fill factor is 21.5% and the twist pitch is 0.3 m. The dimension is 0.5 mm x 3 mm with an additional 0.2 mm thick copper strip soldered to one longer side of the wire. The critical characteristics of the employed MgB_2 wire in the $J-T$ plane are shown in Fig. 2.12. At 10 K and 20 K, a current density above 100 A/mm^2 can be achieved in the magnetic field below 5 T and 3 T, respectively. The operating temperature remarkably limits the current density in high magnetic fields. However, to avoid cooling difficulties similar to LTS, we primarily study the performance of the MgB_2 at 20 K in this thesis as a starting point. Other temperatures will be involved in Chapter 7 when we look for the potential performance of a partially superconducting generator.

Note that engineering (critical) current density is different from (critical) cur-

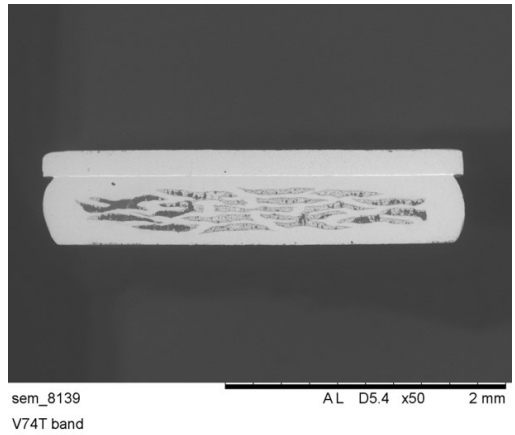

Figure 2.11: Cross-section of a single MgB_2 wire used in this thesis.

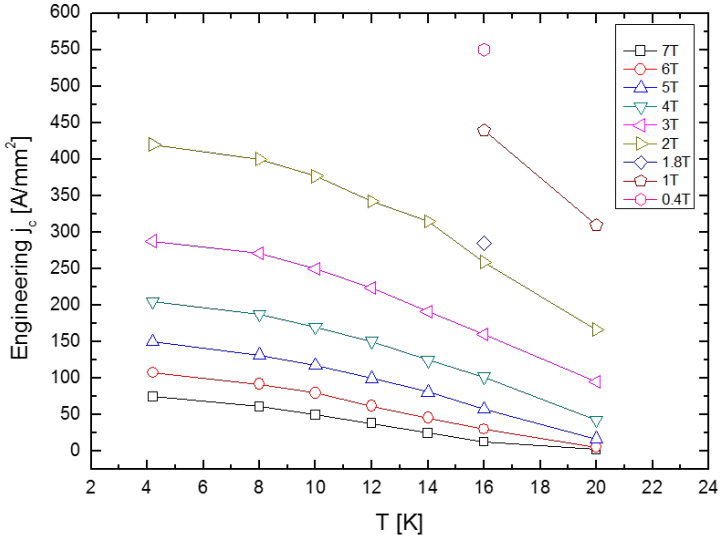

Figure 2.12: Critical characteristics of the employed MgB_2 in the $J-T$ plane.

rent density for characterizing a superconducting material. Engineering (critical) current density is defined as the (critical) current density of a superconducting wire. Critical current density is defined as the critical current density of the superconduct-

ing region of a superconducting wire. In large-scale applications, such as electrical machines, engineering critical current density is extensively used instead of critical current density. In this thesis, we use the term "critical current density" for engineering critical current density for the purpose of simplicity unless particularly pointed out.

2.3. SUPERCONDUCTING MACHINES

Superconducting machines are electrical machines which have superconducting windings to excite the magnetic field and produce the electromagnetic torque. Superconducting generators are superconducting machines which operate in generator mode. The used superconducting materials are multi-filamentary or coated wires consisting of multiple superconductors and other functional materials.

With zero DC resistance, superconducting wires are capable of carrying very large current densities. Superconducting machines take this advantage to excite magnetic fields which can be much greater than conventional machines using copper wires or permanent magnets.

2.3.1. SIZING OF AN ELECTRICAL MACHINE

Interests of applying superconductors in electrical machines originate from sizing electrical machines. The electromagnetic power of an electrical machine is defined by

$$P = \omega_m T_e \tag{2.4}$$

where ω_m is the mechanical rotational speed of the rotor of a machine and T_e is the electromagnetic torque of a machine. In large direct-drive wind turbines, the rotational speed ω_m is very low due to the limitation of keeping a safe tip speed of the wind turbine blades. Hence, the electromagnetic torque T_e must be sufficiently high to achieve the electromagnetic power and then the nominal output power.

The average electromagnetic torque T_e is a function of the average shear stress σ, the air gap diameter D and the active length L of a machine [58]:

$$T_e = \frac{\pi}{2} D^2 L \sigma \tag{2.5}$$

where the average shear stress σ of an electrical machine can be calculated by

$$\sigma = BA \tag{2.6}$$

where B and A are called the magnetic loading (average air gap magnetic flux density) and electrical loading (linear current density) of a machine, respectively. The

electrical loading A is proportional to the current density of the armature winding $A \propto J_s$. The magnetic loading B is determined by the field current density J_f [59].

The electromagnetic torque T_e must be very high in a direct-drive generator. To limit the size of the generator (D or L), we need to increase the shear stress σ by either increasing the magnetic loading B or the electrical loading A. The need for such increases means that we need to increase the current density either in the field winding J_f or in the armature winding J_s or both.

Large wind turbines require electromagnetic torques in the order of about 10 MNm for 10 MW and about 30 MNm for 20 MW. The generator size can roughly be estimated for a 10 MW direct-drive wind turbine. If we use copper conductors for the field and armature windings, the current density of about $J_f = J_s = 3$ A/mm^2 will result in a generator diameter of about $D = 10$ m if the generator length is set to $L = 1$ m. Instead, if we apply superconducting field winding with $J_f = 260$ A/mm^2, it is possible to reduce the generator diameter to $D = 4.3$ m with the generator length of $L = 1.88$ m [20]. Further, if we apply both superconducting field and armature windings with $J_f = 160$ A/mm^2 and $J_s = 100$ A/mm^2, it is claimed to reduce the generator diameter to $D = 3.8$ m with the generator length of only $L = 0.8$ m [26].

Hence, the reduction of generator size will be remarkable by applying superconductors, like what is expected in Fig. 1.4. It can be expected that the weight of electrical machines can also be effectively reduced with a smaller size, both of which are radically the motivation to study and develop superconducting machines.

Table 2.2: Overview of three fundamental machine types.

	DC	Induction	Synchronous
Rotor winding	AC	AC (variable frequency)	DC
Stator winding	DC	AC (fixed frequency)	AC (variable frequency)
Power capacity	low	high	high
Primary application	motor, diesel gen.	motor, DFIG	power generator
Application in MW wind turbines	none	geared DFIG	direct-drive or geared
Suitability for MW SC generators	low	low	high†

†Only when the field winding is superconducting while the armature is not.

2.3.2. MACHINE TYPE

Electrical machines can generally be divided into three basic types: DC (direct current) machine, induction machine and synchronous machine [60]. Each type can operate in both generator and motor modes, but only one of the modes can be de-

signed for satisfactory performance. Above all, not all the three machine types are suitable for applying superconductors. When talking about the suitability of a machine type, we have two criteria:

- adoption of superconductors, and
- feasibility for mega-watt wind turbines.

By overviewing the properties of the three generator types in Table 2.2, the choice space is narrowed down to only synchronous generators which meet both of the criteria.

2.3.3. BASIC STRUCTURE OF A SUPERCONDUCTING SYNCHRONOUS GENERATOR

A superconducting synchronous generator has a DC field winding and an AC armature winding. The field winding is superconducting with superconductors at a low temperature. The armature winding can be either superconducting at a low temperature or non-superconducting with copper conductors at an ambient temperature. Appropriate cooling must be provided to the superconducting winding(s) to maintain the low operating temperature. Structural support must withstand the high torque produced by high magnetic fields. A torque tube or more precisely, a torque transfer element must transfer the torque through the cold winding to warm supports of the generator [61, 62].

One of the basic structures of a superconducting synchronous generator is sketched in Fig. 2.13, which has been widely proposed in the literature. The rotor is accommodated in a cryostat which maintains the operating temperature for the superconductors. Effective cooling is achieved by several means and cryocooler cooling shown in this figure is a popular concept. The electromagnetic part of a superconducting machine consists of field winding, armature winding and the cores to support the windings and increase the magnetic field.

Superconducting coils are usually designed in racetrack shape as illustrated in Fig. 2.14. This shape facilitates manipulating the bending of wires according to the minimum bending radius of superconductors [64, 65]. Each superconducting field coil forms a pole of the synchronous generator. Each pole excites a magnetomotive force (MMF) which is almost squarely distributed along the air gap circumference. Individual field coils are connected in series to form the field winding.

2.3.4. PARTIALLY OR FULLY SUPERCONDUCTING

If a generator has a superconducting field winding with a non-superconducting armature winding, we call it a partially superconducting generator (Fig. 2.13). If both windings are superconducting, as illustrated in Fig. 2.15, we call it a fully superconducting generator. In wind turbine application, most of attention is being paid to

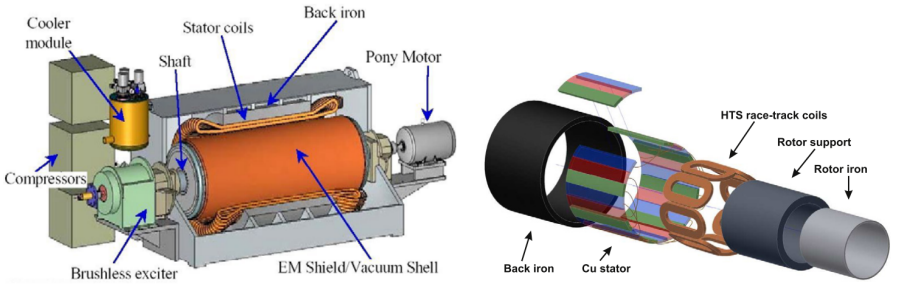

(a) Generator structure. Source: AMSC. [63] (b) Electromagnetic composition. [15]

Figure 2.13: Sketch of a superconducting synchronous generator structure. There are many possibilities of a superconducting machine design. This is only one of them, which is HTS partially superconducting machine, and its magnetic flux is in the radial direction.

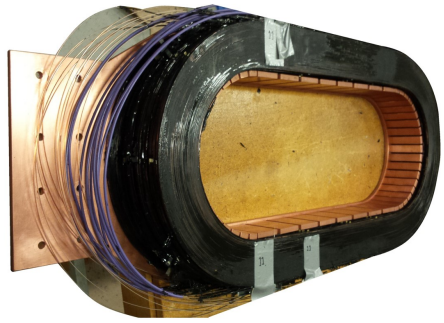

Figure 2.14: Racetrack superconducting coil (MgB_2) for test in the INNWIND.EU project. [66]

partially superconducting generators mainly due to three reasons:

• The level of AC losses in a superconducting armature winding is unacceptable for currently available cryogenic cooling technology [26, 29, 67]. The unacceptability is high for HTS but low for multi-filamentary LTS and MgB_2 with ultra-fine filaments.

• Conventional armature winding design can easily be retrofitted to use and only the rotor needs new design [20, 21]. Design of a superconducting armature winding and its cooling takes much more innovative efforts [25, 68–70].

• The cold mass of a partially superconducting generator is smaller compared to that of a fully superconducting generator. The cold mass can further be reduced when special cryostat design applies to the field winding, e.g. modular cryostat pro-

posed by Technalia [23]. Cooling for smaller cold mass can be easier to manipulate, although the thermal capacity will become smaller.

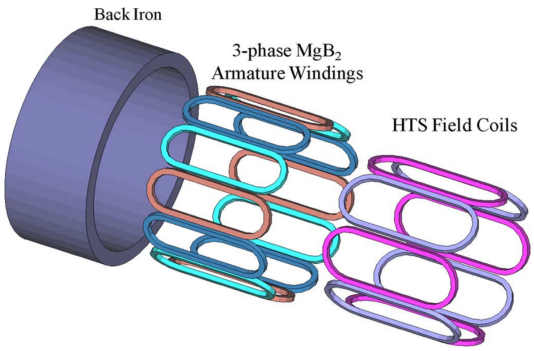

Figure 2.15: Sketch of a fully superconducting machine concept. This is one possibility with an HTS field winding and an MgB_2 armature winding. [70]

However, fully superconducting generators have their own advantages. As mentioned in Section 2.2.1, the ultimate and most exciting advantage is significant reduction of the generator size (to boost the power density, in other words), because the superconducting armature winding produces a high electrical loading. As listed in Table 2.3, we can also break down the advantages and disadvantages of these two superconducting types from the generator design point of view.

Some meaningful attempts have been made to utilize superconductors in the armature winding. Conceptual designs are being developed to reduce the AC losses in the armature winding [71–75]. Fully superconducting generators are considered as a long-term goal for being applied to wind turbines. On one hand, the AC losses will become increasingly smaller and finally acceptable as the superconducting materials are advancing. On the other hand, the cryogenic cooling technology will one day become capable of the high level of AC losses that a superconducting armature winding produces today.

At present or in near future, the most feasible option is thought to be partially superconducting generators, although their effects on increasing power density is not as remarkable as fully superconducting generators.

2.3.5. RADIAL OR AXIAL FLUX

Electrical machines can also be divided into radial, axial [76, 77] and transverse flux machines [78, 79], regarding the direction of magnetic flux as their names suggest. Radial flux generators have dominated the power generation industry as well as the

Table 2.3: Comparison between partially and fully superconducting generators.

	Partially superconducting	Fully superconducting
Field winding	superconducting	superconducting
Armature winding	non-superconducting	superconducting
Magnetic loading	high	high
Electrical loading	low	high
Power density†	moderately high	very high
AC loss	low	high††
Magnetic air gap	large	small†††
Size and weight†	moderately small	very small
Cost†	high	very high
Proposed application	wind energy, ship propulsion	aerospace

†Compared to conventional synchronous generators.

††Ultra-fine filaments can limit the AC loss of a superconductor at a moderate level.

†††Assuming the field and armature windings are located within the same cryostat.

wind turbine market. Because not only people can use the well established design and operation experiences of such machines, but also they are superior to axial flux and transverse flux ones in most aspects. Transverse flux concepts are not mature yet in any power generator. They have low power factors due to large armature leakage fields so the output active power is small. Although power factors can be corrected by a few means, such as active current control by power converters or magnetic circuit optimization, transverse flux machines have rather complicated structures with complex core designs for manufacturing [80]. Thus, we only compare here the radial and axial flux machines (Fig. 2.16) as given in Table 2.4. Nevertheless, transverse flux superconducting generators are being investigated for wind turbine applications (Fig. 2.17). The latest concept can be found in [24] with a few merits highlighted.

Radial flux machines have been concluded to be better than axial flux machines regarding costs when the output is more than 100 kW [29]. Thus, the radial topology is more suitable for generators for mega-watt wind turbines. Axial flux machines are pointed out to become attractive when the number of poles is high and axial length is short [83]. However, superconducting machines usually have a small number of poles which could be a result of the minimum bending radius of superconductors as well as space limitation from mechanical supports [29]. In large offshore wind wind turbines (10-20 MW), radial flux generators are therefore preferred when cost and reliability are of highest design priority.

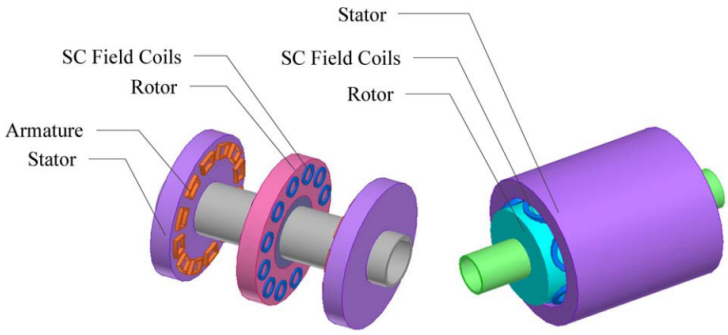

Figure 2.16: Sketch of axial flux and radial flux machine structures. Left: axial flux. Right: radial flux. [29]

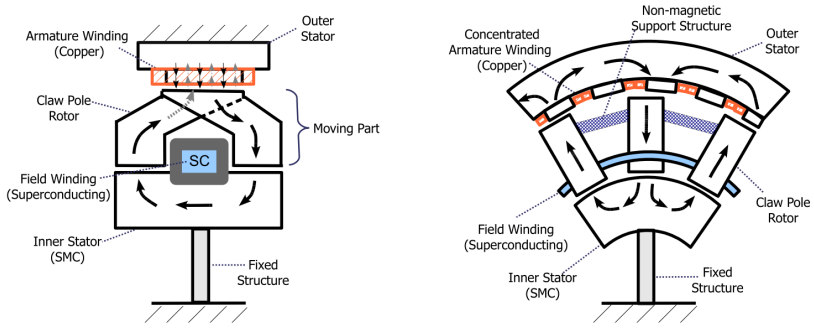

Figure 2.17: Concept of transverse flux superconducting machine. Left: axial cross-section view. Right: vertical cross-section view. [81]

2.3.6. CRYOGENIC COOLING

Superconductors must operate below their critical temperatures. In most cases, they need to be cooled down further to a lower temperature to attain satisfactory performance. For example, LTS prefer 4.2 K or even lower, MgB_2 are proposed for 10-20 K, and HTS are usually proposed for 20-50 K for electrical machines and 77 K for cables and FCLs. In such a vast range of cryogenic temperatures, the cooling efficiency is quite different. Cooling methods and applied coolants are not the same either. Moreover, couplings must be designed to incorporate the cooling system to the rotating electrical machine.

COOLING EFFICIENCY

In general, the cooling efficiency at the required cryogenic temperatures is low. Two factors limit the cooling efficiency. One is the Carnot efficiency which depends on

Table 2.4: Comparison between radial and axial flux superconducting generators [82].

	Radial flux	Axial flux
Torque to volume ratio	larger	smaller
Torque to mass ratio	smaller	larger
Generator diameter†	larger	smaller
Generator length	larger	smaller
Air gap maintaining	easy	difficult for large diameter
Cogging and noise	design dependent	low††
Field coil shape	racetrack (locally concentrated field)	can be circular (more uniform field)

†Due to structural stability.

††Slotless machines.

temperature gradients [84] and the other is the efficiency of refrigerators.

The Carnot efficiency η_c is defined as

$$\eta_c = \frac{T_L}{T_H - T_L} \tag{2.7}$$

where T_L is the cryogenic temperature and T_H is the ambient temperature. It can be seen that the lower the cryogenic temperature, the lower the Carnot efficiency. For example, $\eta_c = 1.4\%$ for $T_L = 4.2$ K and $\eta_c = 34.5\%$ for $T_L = 77$ K, both with $T_H = 300$ K.

At present, the typical efficiency of a refrigerator is 20% which has to be multiplied to the Carnot efficiency. Consequently, the overall cooling efficiency η is even much lower. For example, $\eta = 0.28\%$ for $T_L = 4.2$ K and $\eta = 6.9\%$ for $T_L = 77$ K ($T_H = 300$ K).

Another way to express the overall cooling efficiency is the specific power or so-called cryogenic penalty ($= 1/\eta$). This expression means the number of watts of input power required to remove 1 W of heat at the cryogenic temperature. For example, it requires 14.5 W of input power to remove 1 W of heat from the 77 K region. The cryogenic penalty is 357 W input for 1 W at 4.2 K. The cryogenic penalty at cryogenic temperatures is shown in Fig. 2.18. In this figure, the boiling point of widely used coolants and the critical temperature of different superconductors are also provided for giving a clearer picture of how the cryogenic penalties affect the selection of superconductor types.

CONDUCTION (INDIRECT) OR DIRECT COOLING

The cooling methods for superconductors can be divided into direct and indirect cooling [41, 86, 87]. LTS magnets employing NbTi or Nb_3Sn are in general cooled by submerging them into liquid helium (LHe). This cooling is called pool-boiling

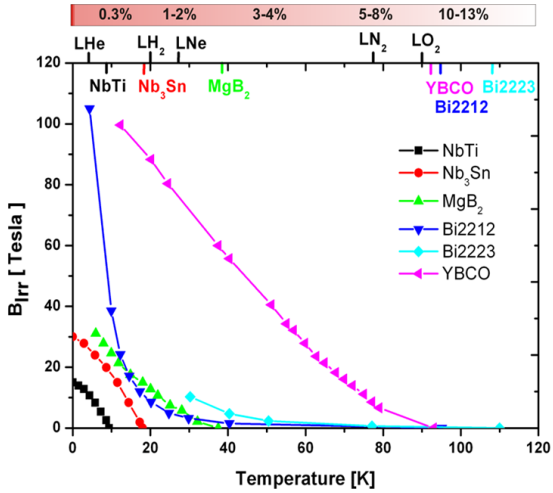

Figure 2.18: $B-T$ critical characteristic of different superconductors, on top of which is the cryogenic penalties at different cryogenic temperature. Different superconductors lie in different ranges of critical temperatures and cryogenic penalties. [85]

method which can also apply to other liquid coolants such as liquid hydrogen (LH_2), neon (LNe), nitrogen (LN_2) and oxygen (LN_2). When demanding more effective and controllable cooling, superconducting magnets are cooled by a forced flow of liquid coolants through conduits between superconductor strands. Very large magnets may use both the approaches.

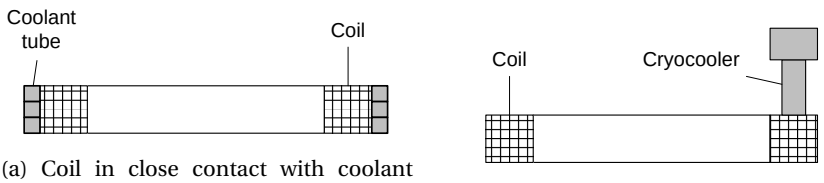

(a) Coil in close contact with coolant tubes.

(b) Coil in contact with a cryocooler.

Figure 2.19: Sketch of conduction cooling concepts. Reproduced from [88].

Indirect cooling is also referred to as conduction cooling. This cooling method is simple and convenient with cryocooler refrigerators [89]. The heat generated in part of superconducting coils is transfered to the cold head of a cryocooler by thermal conduction. The thermal resistance between the coil and the cryocooler must

be designed sufficiently low. The heat transfer can also be realized through tubes in close contact with the surface of a superconducting coil. A coolant which can operate in a closed cycle or with a storage container flows inside the tubes to transfer heat. These two conduction cooling concepts are sketched in Fig. 2.19.

The popular cryocoolers are cryogen free: Gifford-McMahon (G-M) [90, 91], Stirling [92] and Pulse-Tube coolers [93]. All of them apply regenerative heat exchange with oscillating gas flow. The G-M concept is most popular, primarily because it isolates the compressor from the regenerator and displacer and then allows a modified commercial air-conditioning compressor to be used [88]. For low temperature applications, the coolers usually have two stages of temperature, e.g. 300 K-30 K-4 K or 300 K-80 K-20 K, for the purpose of increasing the Carnot efficiency. Single-stage coolers are also used but usually for high temperatures. Stirling cryocoolers are more efficient but more costly than G-M cryocoolers. At present, pulse-tube cryocoolers to date only have small cooling capacities and they need further development.

(a) Gifford-McMahon (Sumitomo RDK-415D).

(b) Stirling (CryoTel GT).

(c) Pulse-tube (Sumitomo RP-062B).

Figure 2.20: Commercial products of three typical cryogen-free cryocooler concepts with regenerative heat exchange.

In wind turbine applications, either direct or indirect cooling can be adopted to a superconducting generator. Regarding cost and construction complexity, conduction cooling with cryocoolers is preferred. The cryocoolers and compressors can be placed outside the generator. Only the cold heads are plugged into the cryostat of the generator and contact the thermal conductor. However, conduction cooling may lead to non-uniform temperature distribution over a superconducting coil and must be carefully examined.

CRYOSTAT

A cryostat is used to house and maintain the superconducting winding in cryogenic environment suitable for the operation of superconductors [94]. Usually, a cryostat means a cryostat assembly which contains a shell, a vacuum chamber, multi-layer thermal insulation and torque transfer elements. With conduction cooling, thermal conductors or cooling tubes are also integrated into the cryostat. Thermally, a cryostat prevents ambient and radiation heat from getting into the cryogenic environment. Mechanically, it transfers the force or torque from the cold parts to the warm parts of the generator. Magnetically, its electrically conductive shell may act as a damping winding or an electromagnetic shield.

Conventionally, a cryostat is shaped cylindrically as large as capable of accommodating the whole rotor or only the field winding assembly, as shown in Fig. 2.21 and Fig. 2.22. This configuration originates from the design and practice of superconducting magnets for MRI and accelerators but results in a relatively large cold mass to be cooled. To minimize the cold mass inside the cryostat as well as modularize the superconducting winding, a modular cryostat concept has been proposed by [23] and [30]. As illustrated in Fig. 2.23, each superconducting field coil has its own cryostat in the same racetrack form. Shells, vacuum chambers and multi-layer thermal insulation are still necessary. Forces are transfered from the cold coil to the warm rotor pole core in the coil center through the cryostat wall. Besides the advantages of cold mass and modularity, this concept enables to employ salient poles which have been extensively applied in conventional synchronous generators. More advantages and applications of such combination of salient poles and modular cryostat will be involved or discussed in every later chapter.

Figure 2.21: Cylindrical cryostat of a commercial product (Babcock Noell GmbH). [95]

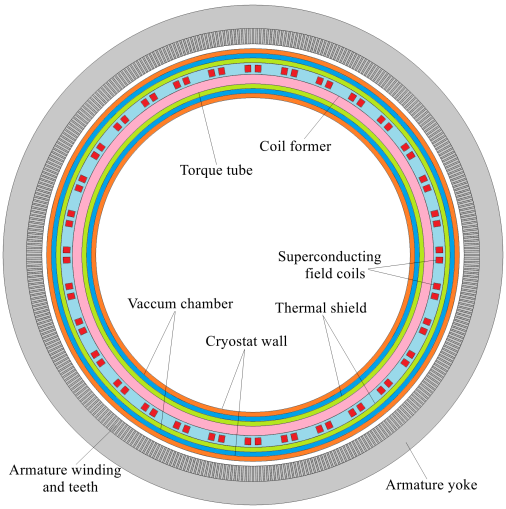

Figure 2.22: Sketch of the cross-section of a cylindrical cryostat in a partially superconducting machine. The superconducting field winding assembly is located within the cryostat. Reproduced from [96].

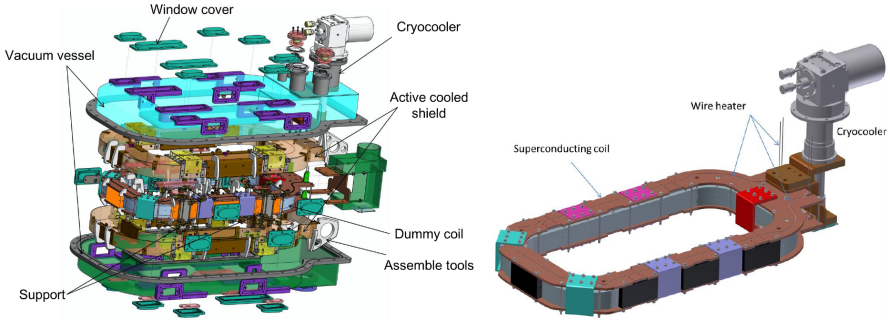

(a) Assembly.

(b) Coil and cooling.

Figure 2.23: Modular cryostat assembly with its components, proposed by the Suprapower project [97, 98].

ROTATING OR STATIONARY SUPERCONDUCTING FIELD WINDING

When cooling the rotating superconducting field winding of a synchronous generator, coupling or sealing is required between the stationary part of the cryogenic

cooling system and the rotating cryostat and field winding. However, the rotating coupling can be avoid by letting the field winding stand still but the armature winding rotate. This reversal of the rotating role requires brushes and slip rings to couple the rotating armature winding to the power converter. The full power will impose onto the brushes which require sophisticated contact. The superconducting field winding remains stationary for simpler cooling system coupling. GE proposed in [20] this concept of rotating armature for their LTS generator design for 10 MW wind turbines.

However, a rotating coupling is not so difficult to realize that most of the superconducting machine designs have still proposed rotating field windings. Although the cooling efficiency may drop due to slight leakage, it is not necessary to introduce less-reliable fully rated brushes to a rotating armature winding. The advantage of rotating field windings may not be recognized by LTS generators but can apply well to HTS generators.

So far, most of the superconducting machine prototypes have employed the G-M cryocoolers. The cold heads are placed inside the generator and pinned to the rotating cryostat. As sketched in Fig. 2.24 for instance, the cold heads connect to stationary compressors outside the generator housing through a rotating coupling.

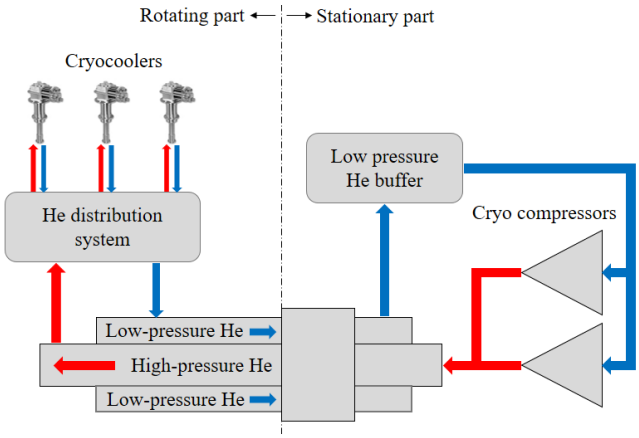

Figure 2.24: Rotating coupling concept: the cryogenic system connected to the rotating and stationary parts of a superconducting generator through rotating coupling (based on G-M cryocoolers). Reproduced from [23].

The rotating coupling concept can also be visualized in Fig. 2.25 proposed by Stirling Cryogenics. Two Stirling cryocoolers are placed outside the generator housing and exchange the warm and cold helium gas out of and into the cold heads in

the generator. The superconducting coils are cooled by the oscillating helium gas flow via cold heads.

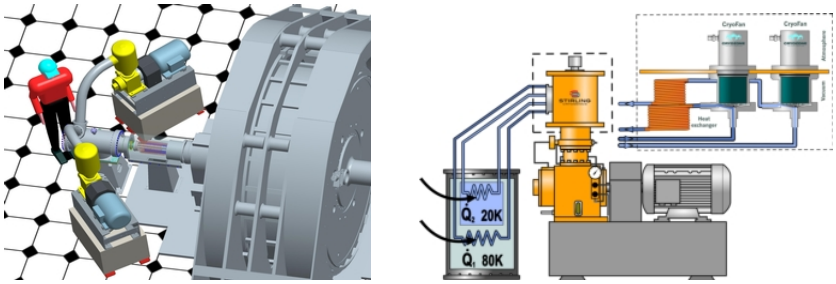

(a) Coupling. (b) Principle.

Figure 2.25: Sketch of the coupling and principle of Stirling cryocoolers for rotating generators, as proposed by [99].

When it comes to a modular cryostat shown in Fig. 2.23, the cooling is more straightforward. the cryocooler's cold head closely contacts the thermal conduction plates (copper). The heat generated by each coil is transferred to the cold head through the copper plates attaching the coil.

2.3.7. DEMONSTRATING PROTOTYPES OF SUPERCONDUCTING MACHINES

Over the last decades, a few pilot projects experimentally demonstrated the feasibility and operation of superconducting machines. At the beginning, the superconducting machine prototypes were designed, built and tested for ship propulsion as motors. Then, more power generators were built and tested. In recent years, a few projects are trying to demonstrate superconducting generators in wind turbine applications. These projects and the corresponding superconducting machines are summarized in Table 2.5.

2.4. INTEGRATION OF SUPERCONDUCTING GENERATORS IN WIND TURBINES

Based on the previous overviews and discussions, we can make a few fundamental choices for a superconducting generator design for wind turbines. The following properties are now preferred for designing the generator:

- Synchronous machine.
- Partially superconducting- only the field winding is superconducting while the armature winding is not.

Table 2.5: Demonstrating projects and superconducting machine prototypes built or being built.

Designer	Report year	Power	Speed	SC material	Cryogenic Temperature	Application
AMSC [100]	2002	3.5 MW	1800 rpm	BSCCO-2223	35 K	Ship propulsion
AMSC [17]	2006	5 MW	230 rpm	BSCCO-2223	32 K	Ship propulsion
AMSC [101]	2011	36.5 MW	120 rpm	BSCCO-2223	30 K	Ship propulsion
AMSC [63]	2006	8 MVar	-	BSCCO	-	Synchronous condenser
Converteam [102]	2009	1.7 MW	214 rpm	BSCCO-2223	30 K	Power generator
GE [103]	1985	20 MVA	3600 rpm	NbTi	4 K	Power generator
GE [104]	2008	1.3 MW	10500 rpm	BSCCO	30 K	Airborne generator
Siemens [105]	2006	400 kW	1500 rpm	BSCCO-2223	25-30 K	Power generator
Siemens [105]	2006	4 MVA	3600 rpm	BSCCO-2223	25-30 K	Power generator
AMSC Sea-Titan* [106]	Ongoing	10 MW	10 rpm	2G HTS	-	Wind power generator
AML* [28]	Ongoing	10 MW	-	MgB_2	-	Wind power generator
EcoSwing* [107]	Ongoing	3.6 MW	15 rpm	YBCO	-	Wind power generator
ICMAB-CSIC* [108]	Ongoing	2 MW	-	-	-	Wind power generator

*The details of the ongoing wind power projects are very limited.

- Radial magnetic flux.
- Conduction cooling with cryocoolers.
- Rotating superconducting field winding.

Given these five choices, a superconducting generator can be integrated into a direct-drive wind turbine nacelle and connected to the power grid through a fully rated power electronic converter, as sketched in Fig. 2.26. Various converter concepts and control strategies have been concretely reviewed in [80, 109, 110] for direct drive systems.

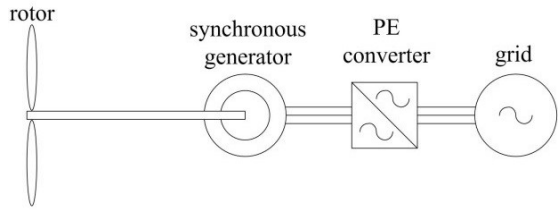

Figure 2.26: Sketch of direct-drive concept. The direct-drive (superconducting) synchronous generator is connected to the power grid through a fully rated power electronic converter. [14]

Different nacelle structures may result in different integration concepts [111, 112]. Here, we introduce three up-to-date wind turbine integration concepts for 10 MW wind turbines available in detail and then the conceptual nacelle from the INNWIND.EU project for 10-20 MW wind turbines. All these concepts are aimed at improving the feasibility of integrating a superconducting generator to a large direct-drive wind turbine.

2.4.1. THREE CONCEPTS IN THE LITERATURE

A few integration concepts have also been proposed by other research projects prior to or in parallel with the INNWIND.EU project. Some are completely new while the others evolve from conventional concepts. Many interesting concepts are proposed for 10 MW direct-drive wind turbines which employ partially or even fully superconducting synchronous generators. Three of them have been published and the details can be found in the literature. The others, e.g. AMSC's and AML's concepts, are not available in detail due to confidentiality issues. Here, the three published concepts are briefly introduced.

GE CONCEPT

GE proposed their integration concept in [20] for a 10 MW direct-drive LTS generator. There are two shafts together supporting the generator as shown in Fig. 2.27. One is stationary in the center for supporting the inner field assembly. The other

for supporting the outer armature assembly is rotating on the stationary shaft via a bearing. The field assembly is inside a cryostat in which liquid helium is cooling the field winding through conduction cooling tubes. The liquid helium is liquefied by cryocoolers located at the two ends of the field assembly.

This concept is novel and suitable for the designed small generator diameter. The nacelle is located behind the hub, but the two-shaft concept can also be used for a front nacelle when an inner stationary field winding is preferred.

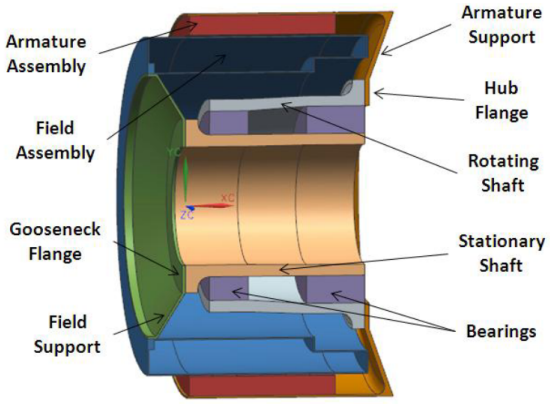

Figure 2.27: Integration concept by General Electric for a 10 MW direct-drive LTS generator. [20]

SUPRAPOWER CONCEPT

The European FP7 project Suprapower [98] has proposed a conceptual nacelle integration. They designed such a large-diameter generator to reduce the generator weight that the generator is axially very short. The small aspect ratio results in the current nacelle concept as depicted in Fig. 2.28. The rotor with field winding is spinning on a stationary hollow shaft via long supporting beams and a bearing. The stator with armature winding is fixed to a large frame which houses both the rotor and stator.

As introduced in 2.3.6, the field coils are housed in individual modular cryostats. Distributed cryocoolers exchange the warm and cold helium gas with the compressors which are concentratedly placed in the hollow shaft. The nacelle is placed behind the hub and may not be capable of being in front due to the large diameter.

SIEMENS CONCEPT

Siemens Wind Power [113] designed a nacelle concept by changing the current direct-drive PM generators into a superconducting version. As shown in Fig. 2.29, in the

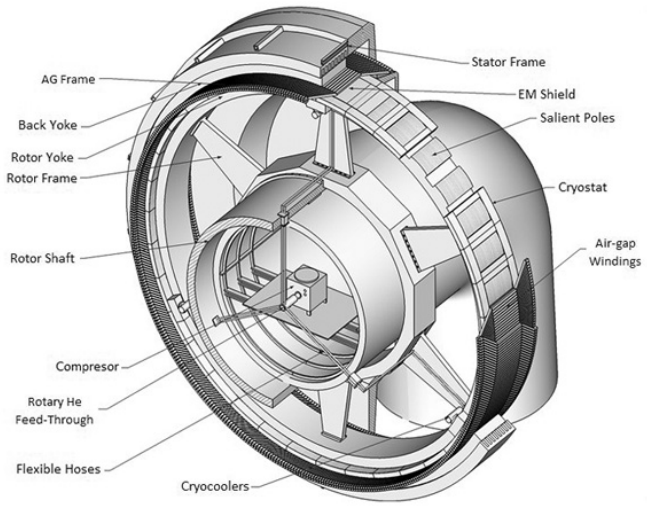

Figure 2.28: Integration concept from the Suprapower project for a 10 MW direct-drive MgB_2 generator. Patented by Tecnalia. [98]

center of the nacelle is also a stationary hollow shaft supporting the inner armature winding. The outer field winding is driven by the spinning hub. This layout and the placement of the cooling system are both similar to those of the "Kingpin" nacelle, but the location of the nacelle is behind the hub and the generator can be designed with an either large or small diameter.

2.4.2. INNWIND.EU CONCEPT

For the INNWIND.EU project, a conceptual nacelle using a kingpin [114] is designed for direct-drive generator systems. As shown in Fig. 2.30, the nacelle is located in front of the turbine hub. The designers claim that this concept not only can be used for 10-20 MW wind turbines but will be the only feasible option for 20 MW [85]. In this concept, the stationary axle (called kingpin) holds both the blades and the generator through one or two bearings. The shorter distance between the large blades for capturing 10-20 MW power and the tower will effectively reduce the bending moment. The front generator will not add significant mechanical loads to the tower because the nacelle weight is negligible compared to the whole mechanical loads.

To adapt to the stationary kingpin, the generator would better have an inner stationary armature winding and an outer rotating field winding. As illustrated in Fig. 2.31, the hollow axle provides a tunnel for placing cryogenic cooling pipes connect-

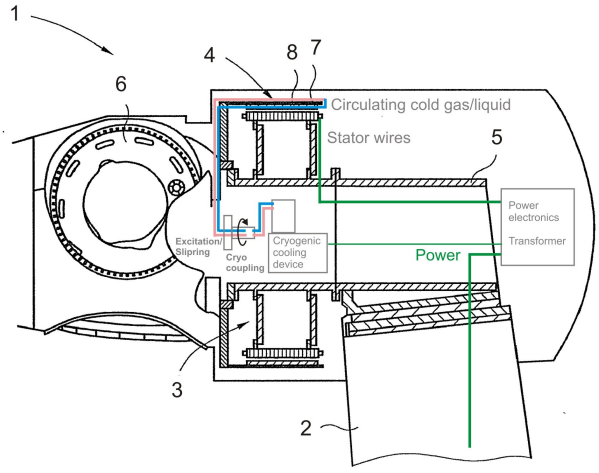

Figure 2.29: Integration concept by Siemens Wind Power for a 10 MW direct-drive HTS generator. (1-Nacelle. 2-Tower. 3-Stator support. 4-Rotating superconducting field winding. 5-Stationary hollow shaft. 6-Hub. 7-Cryostat. 8-Fixed armature winding.) [85]

ing cryocoolers at the generator side to compressors at the tower side.

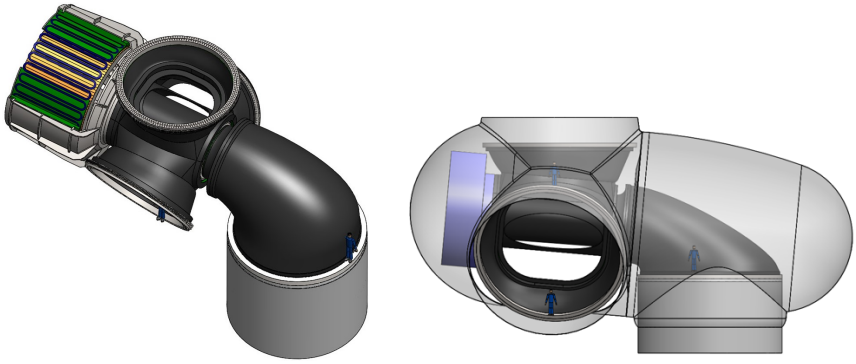

(a) Nacelle with a generator (b) Housing of the nacelle.

Figure 2.30: INNWIND.EU nacelle concept using a kingpin for 10-20 MW direct-drive wind turbines. The generator is located in front of the hub. [11]

Mechanically, the generator can be supported by the main bearing of the hub or a separate bearing, depending on the mechanical load from the generator. A possi-

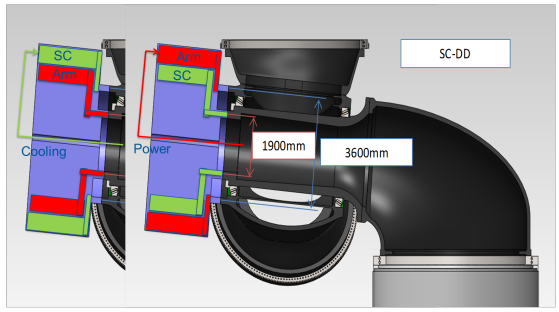

Figure 2.31: Two possibilities of arranging the superconducting field winding and the copper armature winding in the INNWIND.EU nacelle concept. The superconducting field winding will rotate if placed outside. The axle hollow can be used as a channel for placing pipes connecting rotating cryocoolers' cold heads to stationary compressors. [85]

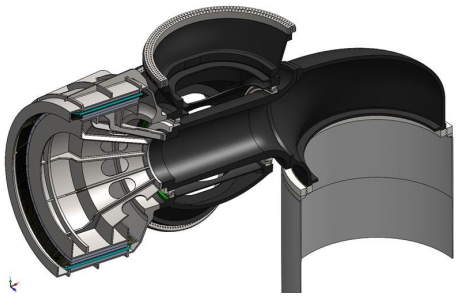

(a) Nacelle profile with kingpin axle.

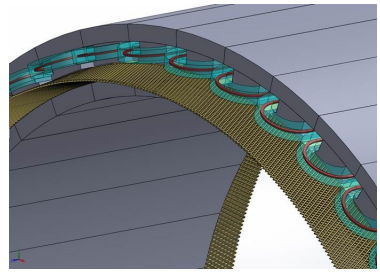

(b) Generator's rotor profile with field coils.

Figure 2.32: A single-bearing scenario of mechanical integration of the superconducting generator to the conceptual INNWIN.EU nacelle. The stationary kingpin holds both the hub and the generator. It is also possible for the generator to have a separate bearing with a lengthened kingpin. Courtesy of DNV GL.

ble scenario of mechanical integration with a single-bearing is depicted in Fig. 2.32. Note that the generator for this scenario employs modular cryostats with salient poles, which is just a particular design possibility to be examined in later chapters. This nacelle may not like large generator diameters due to the limitation of the conic angle of blades, suggesting that the generator diameter would better remain sufficiently small.

The INNWIND.EU nacelle concept will exclusively be adopted throughout the following chapters.

2.5. CONCLUSION

THis chapter has introduced and pictured a superconducting drive train for 10-20 MW direct-drive wind turbines, from superconductors to superconducting generators then to superconducting drive trains. Relevant concepts around superconducting machines, e.g. superconductivity, cooling efficiency, have been described. The integration shows that it is realistic to mount a superconducting generator in a direct-drive wind turbine.

Whatever the nacelle structure, a superconducting generator for this application has four fundamental properties:

• Synchronous machine. This choice is believed to dominate the design of superconducting machines.

• Partially superconducting. This choice may change to fully superconducting as long as either AC losses can effectively be reduced to acceptable levels or cooling technologies become sufficiently advanced to handle the AC losses in a superconducting armature winding.

• Radial magnetic flux. This choice is believed to dominate the design of superconducting machines.

• Rotating superconducting field winding. Rotating field is considered easier than rotating armature. The choice of this property may not be critical and in some cases dependent more on mechanical construction of a wind turbine nacelle.

To simplify the construction of the conceptual INNWIND.EU nacelle, the generator structure of inner armature and outer field is selected. However, this choice does not change the electromagnetic performance of the generator. In next chapters, we will therefore not be limited by this generator structure. Both inner and outer field winding can be considered.

The choice of cooling method, i.e. conduction or direct cooling, does not change the electromagnetic performance of the generator either. We assume conduction cooling with cryocoolers in the next chapters just for providing a context of cooling, as shown in Fig. 2.31, for electromagnetic studies.

3

TOPOLOGY COMPARISON BASED ON CURRENTLY AVAILABLE MgB_2 SUPERCONDUCTORS

Part of the study in this chapter has been published in:

- D. Liu, H. Polinder, A. B. Abrahamsen and J. A. Ferreira, "Topology comparison of superconducting generators for 10-MW direct-drive wind turbines: cost of energy based". *IEEE Transactions on Applied Superconductivity*, vol. 27, no. 4, pp. 1-7, June 2017.

- D. Liu, H .Polinder, A. B. Abrahamsen, E. Stehouwer, B. Hendriks and N. Magnusson, "Optimization and comparison of superconducting generator topologies for a 10 MW wind turbine applications", *International Journal of Applied Electromagnetics and Mechanics*. vol. 53, no. S2, pp. S191-S202, 2017.

- D. Liu, H. Polinder, A. B. Abrahamsen and J. A. Ferreira, "Comparison of 10 MW superconducting generator topologies for direct-drive wind turbines," 2015 IEEE International Electric Machines & Drives Conference (IEMDC), Coeur d'Alene, ID, 2015, pp. 174-180.

- D. Liu, H. Polinder, X. Wang and J. A. Ferreira, "Evaluating the cost of energy of a 10 MW direct-drive wind turbine with superconducting generators," 2016 International Conference on Electrical Machines (ICEM), Lausanne, Switzerland, 2016, pp. 320-326.

3.1. INTRODUCTION

SUPERCONDUCTING synchronous generators are drawing more attention for 10-20 MW direct-drive wind power conversion [11], because they can be lightweight and compact and reduce the levelized cost of energy (LCoE) of the wind turbine [14–16]. Due to the high magnetic field production by superconducting coils, many possibilities exist for designing a superconducting generator. The superconducting coils can be applied only in the DC field winding or also in the AC armature winding. A commonly applied approach is to use an superconducting field winding at a low temperature with a copper AC armature winding at an ambient temperature [29, 115–117]. In such partially superconducting generators, excessive AC losses in the armature winding can be avoided and the feasibility of superconducting generators increases. Among typical superconductor types, MgB_2 could be a starting point as a low-LCoE possibility. This superconductor material is usually for operating temperatures of 10-20 K. It is not as expensive as high temperature superconductors but requires less rigorous cryogenic cooling than low temperature superconductors.

For a partially superconducting generator design, many topologies can be considered from the perspective of electromagnetics. A topology differently combine iron and non-magnetic cores in the rotor back core, rotor pole core, stator tooth and stator yoke. They differ in the magnetic reluctance of an electrical machine. Choice of topology could significantly change the cost and efficiency of a superconducting generator and consequently affect the levelized capital cost of energy (LCCoE) of a wind turbine employing this superconducting generator.

This chapter considers twelve topologies employing MgB_2 in the field winding, which cover most of the applicable radial-flux possibilities. Some of them have already been proposed in the literature or industry. This chapter compares these topologies regarding the LCCoE of a 10 MW direct-drive wind turbine. This chapter only focuses on the LCCoE as the key performance indicator. The other costs, e.g. installation, operation and maintenance costs, are not taken into account since the LCCoE should be evaluated in first place to identify promising candidates which then move onto further evaluations.

Since the superconductor technology is developing fast, only using the current unit cost and critical characteristic of the MgB_2 wires may limit the perspective of comparing the topologies. The topologies that are less advantageous at present may become promising in the long run. Three scenarios are therefore investigated, assuming 1) reducing the wire cost per unit length to 1/4, 2) four times engineering critical current density and 3) the combination of both. The purpose is to check if the topologies providing the lowest LCCoE at present will be overtaken by other topologies if the properties of the MgB_2 wire significantly improve.

3.2. TOPOLOGY-RELATED DESIGN ISSUES

3.2.1. DEFINITION OF TOPOLOGY

The term of topology can be defined differently. In electrical machinery, the generalized definition of topology covers the following design options:

- Radial/axial/transverse flux.
- Inner/outer rotor/stator.
- Rotating/stationary field winding/armature winding.
- Ferromagnetic/non-magnetic core.
- Fully/partially superconducting.

Regarding superconducting machines, the choice of fully or partially superconducting is another topology issue, but we only consider partially superconducting according to the conclusions in Chapter 2.

As discussed in Chapter 2, only the radial flux is considered for superconducting generators for large wind turbines. The choice of inner or outer rotor and the choice of rotating field or armature winding do not matter unless the nacelle or cryogenic design puts limits onto the structure of the generator. Here we suppose that these two choices are not fixed but open in the rest of this thesis, because this thesis will not address the nacelle design or the cryogenic design.

Hence, only the choice of ferromagnetic or non-magnetic core remains, which can also be defined as topology in a narrow sense. In the rest of this thesis, particularly, a topology is defined as the combination of ferromagnetic and non-magnetic materials in four core components:

- Field core back,
- Field pole core,
- Armature tooth, and
- Armature yoke.

The other three design options covered in the generalized definition of topology will not be considered as topology issues anymore in the rest of this thesis.

3.2.2. DESIGN ISSUES RELATED TO TOPOLOGY

In a conventional synchronous machine with a copper field winding or permanent magnets, the core material is usually ferromagnetic, e.g. laminate steel for stator cores and solid steel for the rotor cores. The ferromagnetic material will be saturated when the magnetic flux density goes to a high level, e.g. 1.8 T. A synchronous machine is usually designed for operating with light saturation in its ferromagnetic cores. The purpose of such a design is to produce a sufficiently high magnetic flux density but to avoid negative effects caused by heavy saturation.

This design philosophy would probably change when a superconducting field winding comes into a synchronous machine for field excitation. In the supercon-

ducting field winding flows a rather high current density. e.g. 100 to 200 A/mm^2, which can excite a high magnetic flux density to, e.g., 3 T or even higher in the armature winding. With such a high magnetic flux density, the ferromagnetic core will be heavily saturated. In this case, the use of ferromagnetic cores has four main drawbacks:

• High magnetic flux density in the ferromagnetic material will induce more iron losses, especially when the electrical frequency is high.

• The magnetic flux leakage between adjacent ferromagnetic armature teeth will cause eddy currents in the copper conductors in the armature slots, if the copper conductors are not specially designed for reducing eddy currents.

• Ferromagnetic armature teeth will cause slotting effects which can induce AC losses in the superconducting field winding. Too much AC losses are not acceptable due to both cryogenic cooling capability and efficiency reduction. The slotting effects will reduce if iron teeth are saturated.

• Ferromagnetic materials are heavy so they may reduce the power density. This conflicts with the initial motivation of employing superconducting windings in a wind turbine generator to increase the power density.

It is thus needed to find an alternative material to overcome such downsides of ferromagnetic materials. Generally, this alternative material should have five properties:

• Low iron losses with a high magnetic flux density,
• Less or even no slotting effects,
• Lightweight,
• Not too expensive, and
• Mechanically strong.

From electromagnetics point of view, the suitable material can be characterized as non-magnetic materials. Here a non-magnetic material should also be non-conductive, because we do not want eddy currents in such a material either. Many composite materials are both non-magnetic and non-conductive while stainless steel, for example, is not magnetic but conductive.

Considering mass density, mechanical strength and unit cost, glass fiber G10 has been extensively applied to electrical apparatus [118]. G10 is a composite which is both non-magnetic and non-conductive. Its mass density is about 1850 kg/m^3, which is only about a quarter of the mass density of ferromagnetic steel. Mechanically, G10 is comparable to ferromagnetic steel. A comparison is summarized in Table 3.1 to show the key property differences between glass fiber G10 and ferromagnetic steel.

Using non-magnetic material, e.g. G10, in the machine cores does not definitely mean a better machine design. Despite its advantages over ferromagnetic steel, it has four main disadvantages:

Table 3.1: Property comparison between glass fiber G10 and a typical ferromagnetic steel.

	Glass fiber G10 (FR-4)	Ferromagnetic steel
Relative permeability	1	8000
Electrical conductivity	0	$2{\cdot}10^6$ S/m
Thermal conductivity	0.81 W/(m·K)	50 W/(m·K)
Tensile strength	>310 MPa	490 MPa
Mass density	1850 kg/m^3	7650 kg/m^3

• It is not magnetic. The magnetic reluctance of a machine becomes much larger if non-magnetic material replaces ferromagnetic steel. The machine thus demands more superconducting materials to excite a sufficiently high magnetic field, which can be quite costly.

• It has a poor thermal conductivity. If a non-magnetic material is applied to armature teeth, the cooling of the armature winding will need special attention. For example, indirect forced-air cooling may not be capable anymore but direct cooling would be required.

• It introduces manufacturing difficulties. Large machines have hardly employed non-magnetic cores and their manufacturing is nearly all based on the experience of ferromagnetic steel. Therefore, a design of large machines with non-magnetic cores leads to extra costs in money and time due to difficulties in manufacturing the non-magnetic core structures.

• It is generally more expensive than ferromagnetic steel. For example, the current market price of glass fiber G10 is approximately in the order of 15 €/kg while that of ferromagnetic steel laminates is only about 3 €/kg.

As a result of the above-mentioned facts, comparisons between ferromagnetic and non-magnetic cores are necessary for designing a superconducting machine. Based on such comparisons, the design process may require a few critical trade-offs between adopting ferromagnetic and non-magnetic core materials [29]. Generally, the comparison criteria can be the following characteristics for a superconducting machine:

• Cost,
• Size,
• Weight,
• Efficiency,
• Electromagnetic performance, and
• Thermal performance.

3.2.3. ISSUES ON USING FERROMAGNETIC CORES

Using ferromagnetic cores in a superconducting machine needs special attention due to the high magnetic field. Magnetic saturation, losses, forces and slotting effects are worthy of a discussion.

MAGNETIC SATURATION

A ferromagnetic core saturates in a high magnetic field while a non-magnetic core does not. It is then a question of whether to use ferromagnetic cores or not in a superconducting machine, because a superconducting field winding can produce a high magnetic field which can potentially severely saturate the ferromagnetic cores.

Ferromagnetic materials will have lower magnetic permeabilities when heavily saturated. The relative permeability of a heavily saturated ferromagnetic core will approach $\mu_r = 1$ which is the same as that of a non-magnetic material, e.g. air. However, saturation at this time instant depends on its previous state. With the same magnetic field intensity H, the magnetic flux density B has already become much higher in a ferromagnetic core than that in a non-magnetic core, as illustrated in Fig. 3.1. This shows that saturation of a ferromagnetic core does not deteriorate the excitation of high magnetic fields although the excitation is significantly limited. However, the negative effects of iron cores in high magnetic fields must not be ignored.

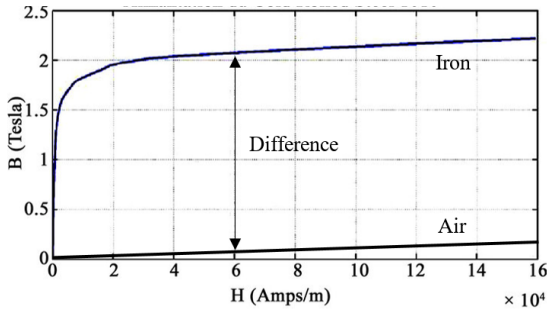

Figure 3.1: Sketch of higher magnetic flux density of iron with full saturation compared to that of air without saturation.

LOSSES AND FORCES

Negative effects could occur in ferromagnetic cores when the magnetic flux density is quite high. One effect is iron losses as a function of magnetic flux density and frequency. However, the fundamental frequency of a 10 MW direct-drive generator could be as low as 3 Hz, for example. In this case, iron losses may be very small.

Another effect is that part of the magnetic flux lines will go through the conductors, i.e. superconducting wires in the field winding and copper conductors in the armature winding. Eddy currents will be induced in these conductive parts and resulting losses could cause problems. Moreover, magnetic forces will directly be imposed on the current-carrying conductors. Hence, special designs will be necessary to suppress the induction of eddy currents and to well support these conductors. In addition, superconducting wires must be sufficiently strong to withstand large mechanical stresses.

SLOTTING EFFECTS

Besides armature winding distribution, slotting effects due to ferromagnetic armature teeth change the air gap flux density at a high frequency [119]. This air gap flux density contains space harmonics which are not synchronous with the rotor rotation. In Fig. 3.2, an example shows the space harmonics of flux density in an air gap. The left figure (Fig. 3.2a) is from a machine with non-magnetic armature teeth and the right one (Fig. 3.2b) is from the same machine with iron armature teeth instead. The spectrum shows that space harmonics contents significantly rise from using non-magnetic to using ferromagnetic armature teeth.

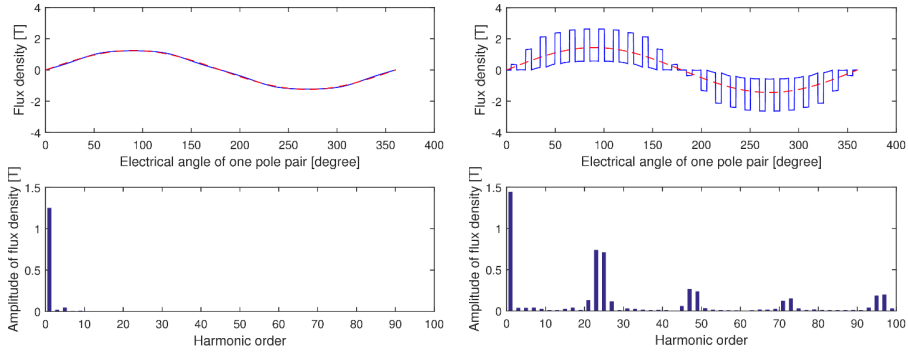

(a) With non-magnetic teeth (b) With iron teeth

Figure 3.2: Slotting effects with iron teeth compared to effects of non-magnetic teeth.

Such space harmonics can go to the region of superconducting field winding and produce AC losses in the superconducting wires and iron losses in the ferromagnetic core parts. If an electromagnetic shield is placed between the field winding and the armature winding for screening the space harmonics and protecting the superconducting wires, eddy current losses will still be produced in this shield itself. All these losses due to slotting effects could lead to reduction of the efficiency and increase of

cooling budgets.

3.2.4. INFLUENCE OF CRYOSTAT DESIGN ON TOPOLOGY

As introduced in Chapter 2, different cryostat designs are accompanied with cold or warm core concepts. The cold core concept makes the topology easy to understand: both the superconducting field winding and the field cores are located inside the cryostat, as sketched in Fig. 3.3a. The cryostat walls are located at both the inner and outer sides of the field winding and the field cores.

The warm core concept consists of two options: cylindrical cryostats or modular cryostats. The former option still uses a tube-shaped cryostat, but the inner cryostat wall separate the field pole core and the field back core. As a result, the field pole core is cold while the field back core is warm, as illustrated in Fig. 3.3b. For topology studies, it is not necessary to separate the field pole core and the field back core so they contact each other with an assumed infinitely thin cryostat wall. However, space for vacuum and thermal insulation must be left between the field winding and this infinitely thin inner cryostat wall.

The modular cryostat concept [23] can be considered as an extension of the cylindrical cryostat concept, but space for vacuum and thermal insulation must be left between one side of the field coil and its surrounding warm cores, as illustrated in Fig. 3.3c. The field pole core can therefore be warm in the center of a field coil and be made as close to the armature as allowed.

For simplification in topology studies, the warm core cylindrical concept is usually considered the same as the cold core concept. Thus, in both these cases, there is not an air gap between the field pole core and the field back core and they contact each other as a whole piece.

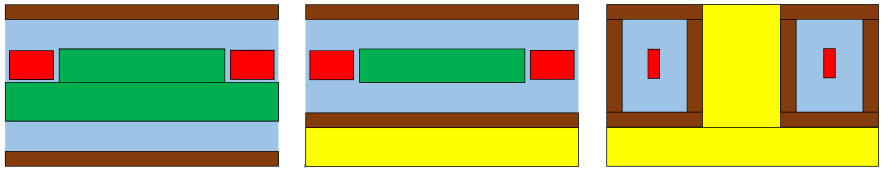

(a) Cold core (b) Warm core: cylindrical (c) Warm core: modular

Figure 3.3: Sketch of one pole for illustrating cryostat concepts. Brown: cryostat wall. Red: superconducting field winding. Green: cold core. Yellow: warm core.

3.3. OVERVIEW OF TOPOLOGIES

COMBINING ferromagnetic and non-magnetic cores in the field back core, field pole core, armature tooth and armature yoke results in 12 applicable topologies (T1-T12) in total as listed and sketched in Fig. 3.4. In this list, nine topologies T1-T3, T5-T7, and T9-T11 have a large effective air gap length due to space allocated to the wall, vacuum and thermal insulation of the used cylindrical cryostat. The other three topologies T4, T8 and T12 with salient iron poles have significantly reduced effective air gap length. Because in these three topologies, the cryostat is made modular in the shape of a racetrack and the iron pole can go as close to the stator as allowed [30, 120, 121]. Topologies T4, T8 and T12 can be regarded as the extensions of topologies T3, T7 and T11, respectively.

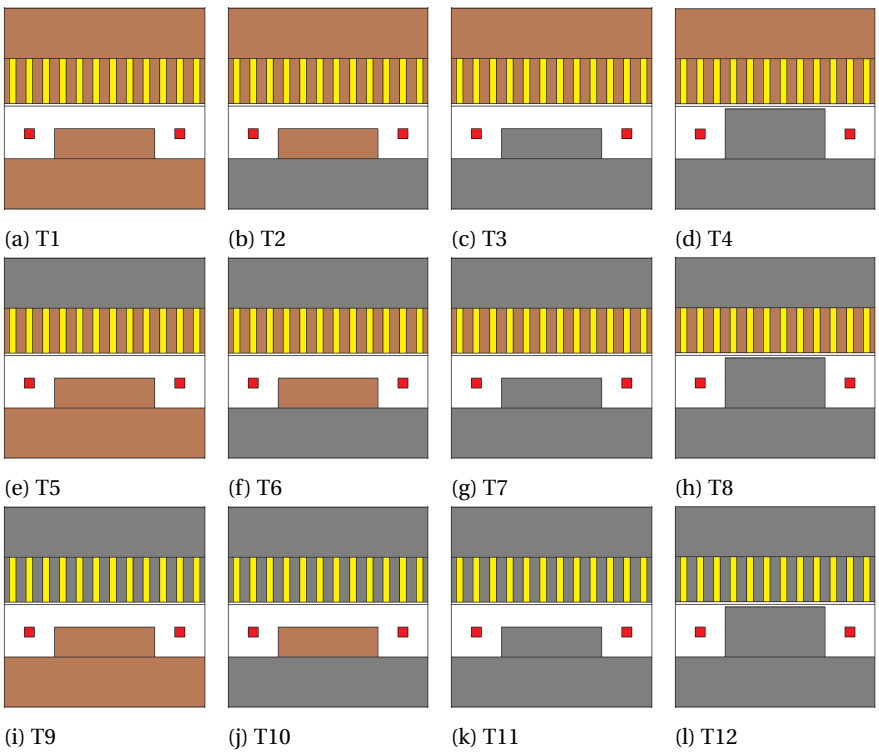

Figure 3.4: Topologies to be compared. Red: superconducting field winding. Yellow: copper armature winding. Brown: non-magnetic core. Grey: iron core.

3.3.1. NON-MAGNETIC ARMATURE CORE (T1-T4)

The first four topologies T1-T4 are with a non-magnetic armature core, as sketched in Figs. 3.4a-3.4d. Both the armature teeth and the armature yoke are non-magnetic. The magnetic field has to be confined somewhere outer the non-magnetic armature yoke or these topologies are used for an inner-armature-outer-field layout. The cooling for the armature winding could be difficult, since classic forced-air cooling used in conventional machines would probably not be sufficiently effective. Direct cooling methods would have to be applied with an increased complexity. Magnetic fluxes go through the copper conductors in the armature slots. Eddy currents and losses are therefore produced in the copper conductors. The copper conductors must be specially twisted by, e.g. Litz wires, or transposed to reduce eddy current losses. However, the non-magnetic armature teeth avoid slotting effects and therefore significantly reduce space harmonics in the air gap flux density. The most decisive fact is that these four topologies may demand a large amount of superconducting wires in the field winding to excite a sufficient flux linkage in the armature winding.

The topology T1 has fully non-magnetic cores since its field pole core and field back core are also non-magnetic. This topology is an extreme case since the magnetic circuit has no ferromagnetic part to reduce the magnetic reluctance. Thus, T1 may demand the largest length of superconducting wires among all the twelve topologies. The advantage is that the manufacturing of such non-magnetic cores can be easy, because all the core materials are the same and there are no joints between different materials. Another advantage is that this topology may result in a lightweight machine because of the lightweight non-magnetic cores.

The topologies T2 and T3 use ferromagnetic field cores instead of non-magnetic ones. The reluctance of the magnetic circuit is reduced. However, due to the fact that the armature core is purely non-magnetic, the reduction of reluctance is very limited. The manufacturing of the field core pieces could be complicated for T2, since the core has two different materials. The topology T3 is different from T2 because T3 is able to employ a whole piece of solid iron for the field core.

By using modular cryostats, the topology T4 with salient ferromagnetic poles has become possible. This topology can be regarded as an extension of T3 but can remarkably reduce the magnetic air gap length. As a result, the reluctance decreases and the demanded amount of superconducting wires will become smaller, but the effect may be very limited due to the absence of ferromagnetic cores in the armature.

These four topologies have hardly be applied in superconducting machine designs, since the ferromagnetic armature yoke which confines the magnetic flux and reduces the reluctance is absent.

3.3.2. NON-MAGNETIC ARMATURE TEETH WITH IRON ARMATURE YOKE (T5-T8)

The topologies T5-T8 have a ferromagnetic armature yoke to confine the magnetic flux within the machine, as sketched in Figs. 3.4e-3.4h. The armature yoke is usually made from silicon-steel laminates. The addition of a ferromagnetic yoke reduces the reluctance of the magnetic circuit and a smaller amount of superconducting wires is demanded for the field winding. These four topologies still have non-magnetic armature teeth so the advantages and disadvantages of such teeth still hold. In addition, the manufacturing for contacting the non-magnetic teeth and the ferromagnetic yoke remains challenging.

The topology T5 looks much more realistic than T1. In many publications, T5 is called "air core" topology. The topologies T6-T8 use ferromagnetic field cores and can significantly reduce the reluctance of the magnetic circuit. Such topologies are often applied to the designs called "air winding" machines, because the armature teeth are non-magnetic and slotting effects disappear. Again, cooling of the armature winding could be challenging and would require extra design efforts. The topology T8 can be regarded as an extension of T7 and remarkably reduces the reluctance of the magnetic circuit.

These four topologies have been more or less applied in superconducting machine designs. Taking wind energy for example, Abrahamsen [122] and Suprapower [23] employed T5 and T8, respectively, to achieve a lightweight design with MgB_2 superconductors for a 10 MW generator.

3.3.3. IRON ARMATURE CORE (T9-T12)

The topologies T9-T12 have a fully ferromagnetic armature core as sketched in Figs. 3.4i-3.4l. These topologies therefore enable the direct use of silicon-steel laminates from the stator core of conventional synchronous or induction machines. Classic forced-air cooling can directly be adopted for the armature winding, which simplifies the armature cooling system. The downsides due to ferromagnetic teeth are mainly slotting effects and resulting losses in the superconducting field winding and the ferromagnetic cores. The losses in the superconducting wires must be carefully examined, since this is about the survival of superconducting wires as well as the budget for cryogenic cooling.

The four topologies keep the armature winding design similar to the stator in conventional synchronous or induction machines. The design of the field cores are therefore made flexible. A fully non-magnetic field core is used in T9 which can provide a lightweight machine. If light weight is less important than the amount of superconducting wires, T11 and T12 could be quite desirable. T10 could be an option to be considered if a balance between weight and superconducting wire usage

is required.

The topology T12 with salient ferromagnetic poles minimizes the reluctance of the magnetic circuit and may remarkably reduce the use of superconducting wires. It looks the same as the topology of a conventional salient-pole synchronous machine. An added value of using salient poles is that the field coils can be moved farther off the armature winding in the radial direction. This feature enables reduction of the influence of magnetic field harmonics from the armature winding and teeth to the field winding. However, the losses in the superconducting wires still need to be examined for the purpose of locating the field coils at an appropriate position.

In terms of application of these four topologies, GE [20] reported a 10 MW superconducting generator design with LTS based on the topology T9, which was aiming at light weight. Xu [120] investigated the topology T12 with 2G HTS at different cryogenic temperatures for 10 MW wind turbines.

3.4. BASIC GENERATOR DESIGN PARAMETERS

THE superconducting generator for topology comparison is designed for 10 MW direct-drive wind turbine with a rated speed of 9.6 rpm. The employed superconductor is magnesium diboride (MgB_2). This type of superconductor can operate superconductingly at higher cryogenic temperatures than LTS, e.g. NbTi, Nb_3Sn. It is also less expensive than HTS. e.g. YBCO, BSSCO.

Only the field winding is superconducting with MgB_2 while the armature winding is still with copper conductors at an ambient temperature. This use of superconductivity has already been defined as partially superconducting. The basic generator design parameters are summarized in Table 3.2. These basic parameters are fixed for the upcoming topology comparison, which means their effects on the comparison results are considered insignificant.

The required torque T_n is 6% higher than the nominal torque calculated from the nominal power of 10 MW. The root-mean-squared (RMS) armature current density of 3 A/mm^2 follows the current density range recommended for large synchronous machines [123]. The armature winding fill factor is 0.6 since this is a typical number for rectangular copper conductors with consideration for appropriate twisting or transposing.

For only comparison purposes, the air gap diameter of the generator is of no importance but it should be selected in such a way that the generator can be well placed in the nacelle of a 10 MW wind turbine. For the conceptual INNWIND.EU nacelle introduced in Chapter 2, the generator diameter is considered not too large so that the hub and generator sizes fit. Here the air gap diameter of 6 m is used and assumed to accomplish such compactness. The mechanical air gap is then set to 6 mm (0.1% of the air gap diameter as a role of thumb). The distance from the

Table 3.2: Basic generator design parameters.

Basic parameter	Value
Required torque	T_n = 10.6 MNm
Air gap diameter	$d_s = 2 \cdot r_s$ = 6 m
Number of phases	$m = 3$
Number of slots per pole per phase	$q = 4$
Armature current density	J_s = 3 A/mm^2
Distance from outer field winding to air gap	h_{fg} = 40 mm
Mechanical air gap length	g = 6 mm
Armature winding fill factor	k_{fil}=0.6
Cryogenic temperature	20 K

outer field winding to the air gap contains a cryostat wall, vacuum and multi-layer thermal insulation.

The cryogenic temperature for operating the MgB_2 superconductor is 20 K which is sufficient far from the critical temperature of 39 K for MgB_2. This temperature allows for easier cryogenic cooling, compared to the operating temperature of 4 K for low temperature superconductors.

The number of slots per pole per phase q is selected based on the concerns of slot pitches and slotting effects, although its effects will not change the topology comparison results. Due to the minimum bending radius of a superconducting wire, the pole pitch should be sufficiently large. A large pole permits a relatively large number of q. However, a large number of q may result in a too small slot pitch within the fixed air gap diameter of 6 m. A small number of q can lead to more slotting effects which are not wanted by the superconducting field winding due to AC losses. The number of $q = 4$ is expected to satisfy both of the concerns. However, determining the number of q needs other studies, which is out of the scope of this chapter.

The generator has an outer armature winding and an inner field winding. This structure can be reversed and the topology comparison results will still hold. Either the armature winding or the field winding can be rotating. The superconducting field winding is operated with a 25% safety margin to its in-field critical current density. The generator axial length is obtained in such a way that the required torque is fulfilled when the air gap diameter is fixed to 6 m. The chosen material for the non-magnetic cores is glass fiber G10 whose main properties have been summarized in Table 3.1.

3.5. COMPARISON CRITERION: CAPITAL COST OF ENERGY

3.5.1. WHY COST OF ENERGY?

COST of energy is the key performance indicator for wind energy conversion. For a new technology, like superconducting generator, cost of energy is used to evaluate its feasibility of commercialization. If the cost of energy is too high, industry will not be interested.

For the purpose of topology comparison, cost of energy is also used to eliminate those too expensive or too inefficient topologies. The rest topologies can then be chosen for further investigation. Therefore, we use cost of energy as the criterion for topology comparison.

3.5.2. DEFINITION OF COST OF ENERGY

A levelized cost of energy of a wind turbine is defined by [124, 125]

$$LCoE = \frac{C_{CAPEX}}{a \cdot E_{AEP} \cdot T_{LT}} + \frac{C_{O\&M}}{E_{AEP}} + \frac{C_{Decom}(1+r)^{-T_{LT}}}{a \cdot E_{AEP} \cdot T_{LT}} \tag{3.1}$$

Where C_{CAPEX} is the total capital expenditure of a wind turbine, $C_{O\&M}$ is the annual operation and maintenance expenditures of a wind turbine, C_{Decom} is the decommissioning expenditure in the year of shutting down the wind turbine, E_{AEP} is the annual energy production, a is the annuity factor assuming an interest rate of r, and T_{LT} is the design life time of the wind turbine. In this thesis, we assume $a = 0.564$, $r = 5\%$ and $T_{LT} = 25$ years.

Although the operation and maintenance expenditures are important, C_{CAPEX} is much more sensitive for designing a superconducting drive train. There have been no experience of operating and maintaining a superconducting generator system in a wind turbine. Feasibility assessment of applying superconducting machines to wind turbines highly depends on the level of C_{CAPEX}. We can only consider C_{CAPEX} at this moment for feasibility studies, after which the operation and maintenance expenditures can be estimated and added to the calculation of cost of energy.

3.5.3. CAPITAL EXPENDITURE

A capital expenditure of a wind turbine consists of the cost of the generator system and the total cost of the other parts of the wind turbine. The generator system cost consists of the cost of the generator's active material C_{act}, the cost of the generator's supporting structure C_{str}, the cost of the generator's cryogenic system C_{cryo} and the cost of the power electronic converter C_{PE}. Now the LCCoE can be written as

$$LCCoE = \frac{C_{CAPEX}}{a \cdot E_{AEP} \cdot T_{LT}} = \frac{C_{act} + C_{str} + C_{cryo} + C_{PE} + C_{other}}{a \cdot E_{AEP} \cdot T_{LT}} \tag{3.2}$$

Choice of topologies changes C_{act}. The other costs of the wind turbine in Eq. (3.2) is assumed to be constant since they can hardly be changed by topology choice. Thus, the LCCoE can now be written as

$$LCCoE = \frac{C_{act} + C'_{other}}{a \cdot E_{AEP} \cdot T_{LT}} \tag{3.3}$$

ACTIVE MATERIAL COST

Here the active materials under consideration are

- Superconducting wires for the field winding,
- Copper conductors for the armature winding,
- Ferromagnetic material for the core, and
- Non-magnetic material for the cores.

To evaluate the level or feasibility of capital cost of energy, the first step is usually to check if the active material cost of the generator goes too high due to expensive superconducting wires. If the active material cost stays in an acceptable level, the study on other costs as well as the energy production can follow up. If the active material cost turns out to be too high, the value of using superconductivity will become questionable. Thus, we must have a range or level of the active material cost of a superconducting generator before going to evaluate the cost of energy of a wind turbine.

In this chapter, we assume the following unit costs for the active materials:

- MgB_2 superconductor: 4 €/m (based on currently available wires),
- Copper conductor: 15 €/kg,
- Iron core: 3 €/kg, and
- Non-magnetic core (glass fiber G10): 15 €/kg.

The cost of each component of the wind turbine considered in the LCCoE is given in Table 3.3. The cryogenic system cost depends on a particular cryogenic design and can hardly be estimated by electromagnetic analyses, and the cost estimation for supporting structures needs detailed mechanical analyses. Here these two costs are estimated based on a 13.2 MW LTS superconducting generator in [33].

The cost model from the INNWIND.EU project defines a reference 10 MW wind turbine and estimates the cost of each wind turbine component [11]. The balance of plant is the cost of all infrastructural and facilities of a wind farm with an exception of the turbine and all its elements. The balance of plant therefore mainly comprises of foundations, crane pads/hard standing, cabling to substation and grid, transformers and miscellaneous costs. Here this balance of plant is averaged to one turbine. The total cost excluding C_{act} is roughly 27,000 k€ which is given to Eq. (3.3) as C'_{other}. The costs of the turbine tower and the turbine foundation are assumed to be constant in Table 3.3, because the wind loads are the main design drivers. This

Table 3.3: Estimation of the other costs of the 10 MW INNWIND.EU reference wind turbine.

Parameter	Cost	Reference
Wind turbine (excl. gen. system)	7,500 k€	Cost model in [11]
Balance of plant	17,000 k€	Cost model in [11]
Power electronics C_{PE}	800 k€	Cost model in [11]
Cryogenic system C_{cryo}	600 k€	LTS SCSG in [33]
Generator supporting structures C_{str}	880 k€	LTS SCSG in [33]
Total C'_{other}	26,780 k€	-

assumption neglects the influence of generator topologies on the costs of the supporting structures of the wind turbine. Therefore, the results of this paper, especially the size and mass of different topologies, need to be exported to structure designers to assess the structural costs for each generator topology. In this paper, the resulting active material masses of the topologies will be compared with a reference mass in Section 3.7 to check if they reach low weight.

The definition of Eq. (3.3) can be applied for optimizing the electromagnetic design of a superconducting generator for the minimum LCCoE of a wind turbine. In such an application, it is not correct to eliminate the constant cost C'_{other} in Eq. (3.3), even if only C_{act} can vary and C_{act} is in fact relatively very small. Because the minimum point will be different between the LCCoEs with and without C_{other}. The constant C'_{other} added to the numerator of Eq. (3.3) changes the minimum point of $LCCoE$.

3.5.4. CALCULATION FOR ACTIVE MATERIAL COST

The procedure of calculating the active material cost follows the flow diagram in Fig. 3.5. When determining the operating current density and the electromagnetic torque per unit length, 2D FE models are used, taking into account the non-linear B-J load curve of the field coil and the non-linear B-H magnetization curve of the magnetic iron.

FINITE ELEMENT MODELING

The 2D FE model of the superconducting generator is illustrated in Fig. 3.6. Only one pole is needed for this model. The boundary condition $\frac{dA_z}{dn} = 0$ is used for both sides of the pole to model the periodicity. The outer boundary is the Dirichlet boundary $A_z = 0$ which means that no magnetic flux can leave this boundary. The domains of air are necessary since the magnetic flux can leave the domains of core. Only half of the phase coils is needed for this model and follows the order described in this

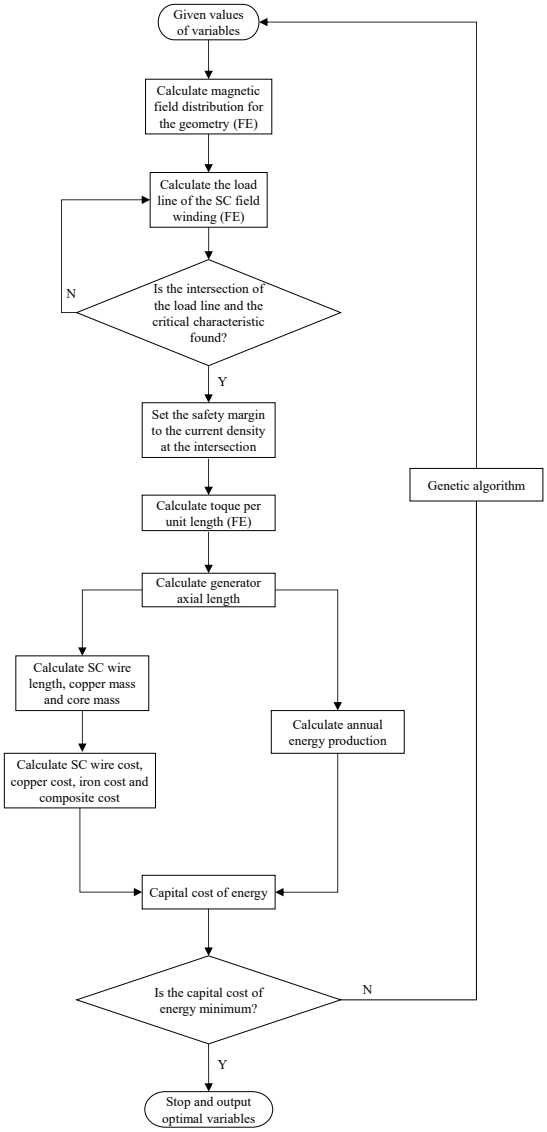

Figure 3.5: Flow diagram for calculating the capital cost of energy and implementing genetic algorithm for optimization.

figure. The material for the iron core is silicon steel NGO M-14 and its B-H curve used in the FE program (COMSOL Multiphysics) is shown in Fig. 3.7.

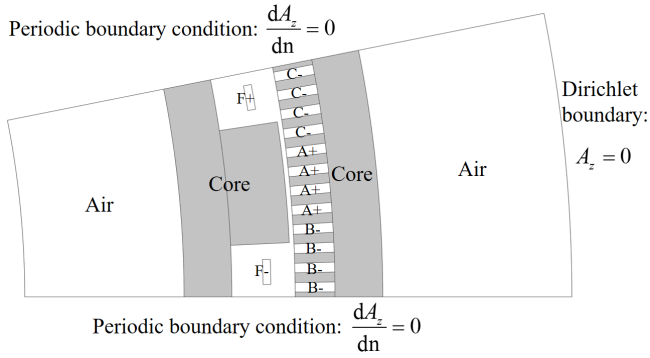

Figure 3.6: Finite element model of the generator. Only one pole needs modeling with boundary conditions.

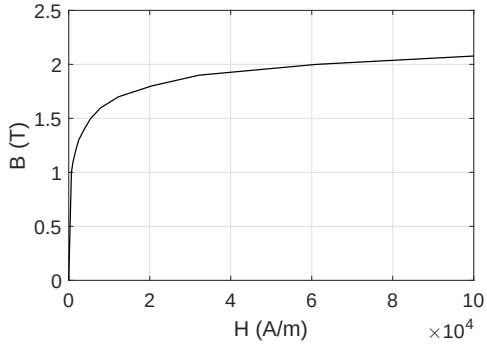

Figure 3.7: B-H curve (silicon steel NGO M-14) used in the FE simulations. Reproduced from COMSOL Multiphysics v4.4.

OPERATING FIELD CURRENT DENSITY

The operating current density of an superconducting field coil must stay below the critical current density of the superconductor wires, otherwise the wires will enter their non-superconducting states. The critical current density J_E as a function of the magnetic flux density B and the temperature T is normally provided by the superconductor wire supplier. The machine topology determines the so-called load line

which is defined here as the maximum flux density of an superconducting coil with respect to the current density flowing in an superconducting wire.

In Fig. 3.8 the critical point is indicated at which the load line (the red line) crosses the critical characteristic (the blue line with dots). The intersection is at the boundary of the superconducting state which does not tolerate small increases of the current density. A margin of 25% is therefore introduced to obtain the operating point for safe operation.

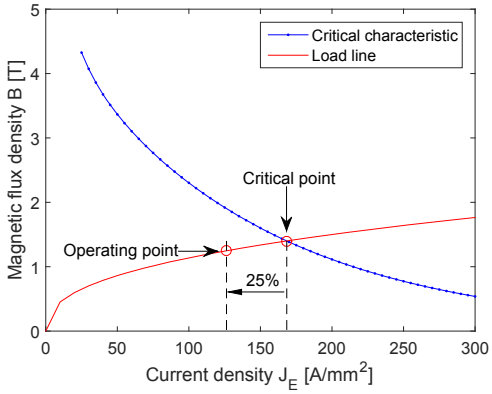

Figure 3.8: Definition of the operating point of the field current density by crossing the load line and the critical characteristic at the temperature of 20 K.

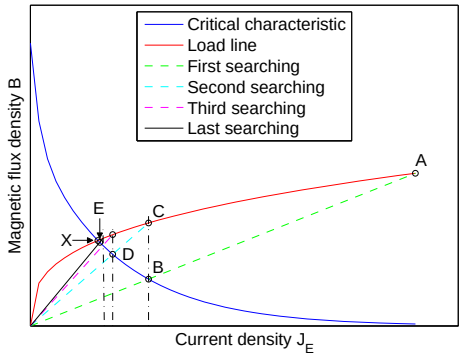

Figure 3.9: Illustration of iteratively finding the critical point of the superconducting field winding by several steps of FE computation, considering a non-linear load line.

The load line may, however, not be linear, depending on the saturation of the

iron core parts of the machine, so we cannot simply find one point on the load line and extrapolate it to the origin linearly. It would also be too time consuming to find all the points on the load line by finite element computations. Here a method is proposed to iteratively find the critical point by a small number of computations with FE models.

First of all, we must distinguish the current density in a wire $J_{E,wire}$ and the current density in a coil $J_{E,coil}$. This is because the critical characteristic given in Fig. 3.8 does not use $J_{E,coil}$ but $J_{E,wire}$ as the current density, whereas we apply $J_{E,coil}$ in the SC field coils in the FE model and compute the magnetic field. We use the corresponding $J_{E,wire}$ to establish its correlation to the maximum magnetic field B in the SC coil. With a filling factor of $k_{fil,sc}$ for the superconducting coil, the relation can be written as

$$J_{E,coil} = k_{fil,sc} \cdot J_{E,wire} \tag{3.4}$$

As illustrated in Fig. 3.9, the unknown load line in red is not linear. The critical characteristic in blue crosses the load line at point X, which needs to be found right now by a searching process. At the beginning of searching for the intersection point X, we set a uniform coil current density $J_{E,coil,A}$, which is far higher than needed, to the superconducting field coils. The computed maximum flux density in the superconducting coils is at point A which must be located on the load line. We connect point A to the origin linearly and this connecting line crosses the critical characteristic at point B. Here the current density at point B is the wire current density $J_{E,wire,B}$.

Then we give the coil current density $J_{E,coil,B}$ of point B (using the relation in Eq. (3.4)) uniformly to the superconducting coils and compute the maximum flux density of the superconducting coils which must be at point C on the load line. We connect point C to the origin linearly and this connecting line crosses the critical characteristic at point D. We iterate this process a few times, and the computed maximum flux density will finally reach point E which is close enough to point X, judged by a pre-set tolerance ε given by

$$B(k+1) - B(k) \leq \varepsilon, \quad k = 1, 2, 3, ... \tag{3.5}$$

where $B(k+1)$ is the maximum flux density of the superconducting coils for the computation $k+1$ and $B(k)$ is the maximum flux density of the superconducting coils for the previous computation k. Here we use the tolerance of $\varepsilon = 0.02$ T which is roughly 1% of the maximum magnetic field in the field coils.

This final intersection of point E is the critical point of the superconducting field winding (as seen in Fig. 3.8), which is limited by the strongest magnetic field in the superconducting field coil. The current density at point E should then be reduced by the factor of 25% to become the operating field current density, considering a

reasonable margin for safe operation. This searching process for the operating point requires only 4 to 6 iterative FE computations.

ELECTROMAGNETIC TORQUE

The electromagnetic torque obtained in a 2D FE model is the torque per unit length T_z. The generator axial length can then be calculated by

$$l_s = T_n / T_z \tag{3.6}$$

The torque T_z is an average value calculated from two stationary FE simulations. These two simulations differ in the relative position between the rotor and stator, and the phase angle of the armature current. From the first position to the second, as illustrated in Fig. 3.10, the rotor rotates with an angle of $1/(4mq)$ of a mechanical cycle while the phase current shifts by a time of $1/(4m)$ of an electrical cycle. Choosing these two positions is under the assumption that the 6_{th} time harmonic of the magnetic field contributes to the force ripples most. Then, an electrical cycle has 6 cycles of force ripples. Compared with a complete transient simulation of the torque, the error resulted from this averaging method is less than 5% and this accuracy is acceptable for this comparison study.

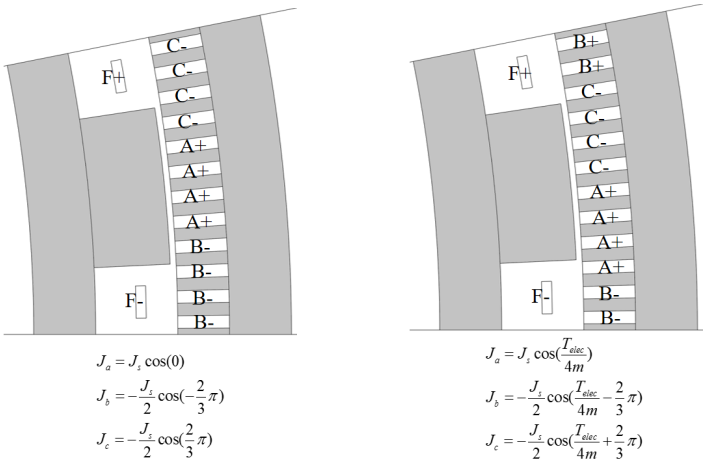

(a) The first position (b) The second position

Figure 3.10: Two positions in the FE model for calculating the average torque. The phase current density for the corresponding position is provided. T_{elec} is the time period of one electrical cycle.

3.5.5. ENERGY PRODUCTION

The energy production of a wind turbine is determined by energy losses. Here only the electrical energy exported from the generator system is considered as energy production. The losses after the generator system, e.g. cable losses, transformer losses, are not taken into account.

WIND SPEED DISTRIBUTION

The wind condition for designing 10 MW wind turbines is defined by the INNWIND.EU project [11]. The wind speed follows Weibull distribution with the following parameters:

- Average wind speed: $v_{w,avg} = 9.2$ m/s,
- Shape factor $k = 2$, and
- Scale factor $A = 10.39$.

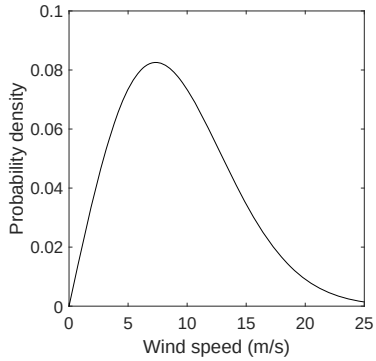

Figure 3.11: Weibull distribution of wind speed.

OPERATION OF THE WIND TURBINE

The operation of the wind turbine is characterized by power and speed.

Power The input power to the generator system P_{in} is the shaft power from the hub of a wind turbine. This power is determined by the aerodynamic power from wind:

$$P_{ad} = 0.5\rho_{air} C_p \pi r_{tr}^2 v_w^3 \tag{3.7}$$

where ρ_{air} is the mass density of air, C_p is the power coefficient of a wind turbine, r_{tr} is the turbine rotor radius, and v_w is the wind speed.

The reference wind turbine has a rotor radius of $r_{tr} = 89$ m. Its cut-in wind speed is $v_{w,cut-in} = 4$ m/s and its cut-out wind speed is $v_{w,cut-out} = 25$ m/s. Note that the

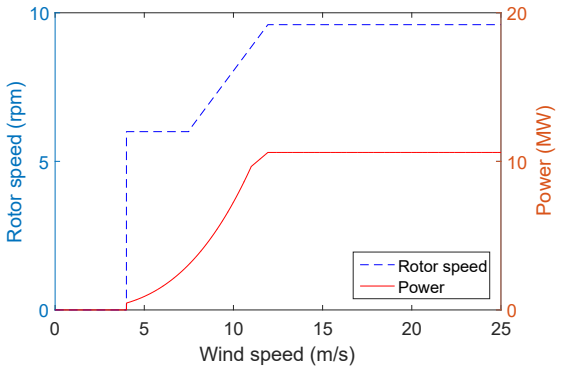

Figure 3.12: Rotor speed and power with wind speed.

rotor rotates at a constant speed of 6 rpm at the wind speed between $v_{w,cut-in}$ = 4 m/s and 7.5 m/s.

When the wind speed is smaller than the cut-in speed, the mechanical power to the drive train is zero: $P_{in} = 0$.

When the wind speed is between the cut-in and cut-out speeds and the aerodynamic power is lower than the rated power of the wind turbine $P_{WT,N}$ = 10.6 MW, the mechanical power to the drive train follows Eq. (3.7). Now the power coefficient is set to its maximum $C_p = C_{p,max} = 0.476$.

When the wind speed is between the cut-in and cut-out speeds but the aerodynamic power is higher than the nominal power of the wind turbine $P_{WT,N}$ = 10.6 MW, the blade pitch control takes action and the power coefficient drops to keep a constant rated power into the drive train:

$$P_{in} = P_{WT,N} \tag{3.8}$$

Speed The generator's rotational speed is given by

$$n = \frac{60\lambda v_w}{2\pi r_{tr}} \tag{3.9}$$

with a tip-speed ratio of $\lambda = 7.9$ and a rated speed of $n_N = 9.6$ rpm. The speed follows the operation as follows:

- If $0 < n < n_N$, then $n = 0$,
- If $n > n_N$ and $v_w < v_{w,cut-out}$, then $n = n_N$,
- If $v_{w,cut-in} < v_w < 7.5$ m/s, then $n = 6$ rpm,
- If $n > n_N$ and $v_w < v_{w,cut-in}$, then $n = n_N$, and
- If $v_w > v_{w,cut-in}$, then $n = 0$.

According to this wind turbine operation, the profiles of wind distribution, aerodynamic power and rotational speed with respect to wind speed are plotted in Fig. 3.12.

OPERATING POINT OF GENERATOR

The generator is operated under the phasor diagram given in Fig. 3.13, which is fully controlled by the power electronic converter. The control strategy is zero d-axis control with which the d-axis current of the generator remains zero and the torque is proportional to the q-axis current. The major advantage of this control strategy is relatively low copper losses in the armature winding.

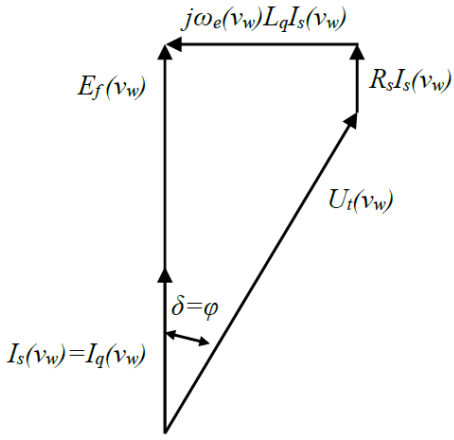

Figure 3.13: Phasor diagram of the generator operating point.

POWER LOSSES

The power flow of a superconducting drive train is sketched in Fig. 3.14. Assuming that mechanical losses, e.g. bearing and windage losses, are neglected, all the aerodynamic power reaches the generator $P_{in} = P_{ad}$. In a superconducting generator, the total power loss consist of

- Joule copper losses in the armature winding $P_{Cu,cond}$,
- Eddy current losses in the armature winding copper $P_{Cu,eddy}$, and
- Iron core losses P_{Fe}.

The losses, both DC and AC losses, in the superconducting winding are negligibly small, according to the study in [121]. Thus, these losses are not considered.

In addition, the refrigeration for cooling the cryogenic environment for superconducting wires demands a power at an ambient temperature, which can also be considered as a power loss P_{cryo}.

As a part of a generator system, a power electronic converter also produces a loss P_{conv}, which reduces the efficiency of a generator system.

The output power from a generator systems can be calculated by

$$P_{out} = P_{ad} - P_{Loss} \tag{3.10}$$

where P_{Loss} is calculated by

$$P_{Loss} = P_{Cu,cond} + P_{Cu,eddy} + P_{Fe,s} + P_{cryo} + P_{conv} \tag{3.11}$$

Joule copper losses in the armature winding The I^2R copper loss $P_{Cu,cond}$ as a function of wind speed is given by

$$P_{Cu,cond}(v_w) = 3I_s^2(v_w)R_{Cu} \tag{3.12}$$

where $I_s(v_w)$ is the phase current as a function of wind speed, R_{Cu} is the electrical resistivity per phase of the armature winding at the operating temperature of about 120 °C.

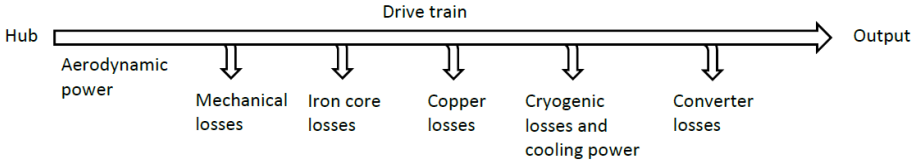

Figure 3.14: Power flow and losses in a superconducting wind turbine drive train.

Eddy current losses in the armature winding The copper loss $P_{Cu,eddy}$ due to induced eddy currents can be effectively reduced by stranding the copper conductors. Due to heavy saturation in a superconducting machine, special attention must be paid to the stranding of copper conductors. There are models which can estimate the eddy current loss in copper strands if the dimension of a strand is known. Here we use the model given in [126]:

$$P_{Cu,eddy}(v_w) = \frac{1}{24\rho_{Cu}}\omega_e^2(v_w)(a^2B_r^2 + b^2B_t^2)V_{Cu,s} \tag{3.13}$$

where $\omega_e(v_w)$ is the angular electrical frequency as a function of wind speed, B_r and B_t are the radial and tangential components of the flux density (amplitude) in a

copper conductor (or an armature slot), $V_{Cu,s}$ is the copper volume only in the stack length, and a and b are the height and width of a copper strand. In this chapter, we use fine strands for the copper conductors with $a = b = 5$ mm.

Iron core losses Iron core losses exist in iron cores but does not in non-magnetic cores which are also non-conductive. Iron core losses come from hysteresis losses and eddy current losses both of which are functions of flux density and frequency. The total iron loss per unit mass can be modeled by

$$P_{Fe}(v_w) = 2[(\frac{B_r}{1.5})^2 + \frac{B_t}{1.5})^2][k_h(\frac{f(v_w)}{50}) + k_e(\frac{f(v_w)}{50})^2] \tag{3.14}$$

where $k_h = 2$ W/kg and $k_e = 0.5$ W/kg are respectively the hysteresis loss and the eddy current loss per unit iron mass with the field of 1.5 T and the frequency of 50 Hz. B_r and B_t are respectively the radial and tangential components of the flux density (amplitude) in the iron core, and $f(v_w) = \omega_e(v_w)/2\pi$ is the electrical frequency as a function of wind speed. The factor of 2 is included in Eq. (3.14) because the flux densities do not change sinusoidally and they are not sinusoidally distributed, which increases the iron losses. In addition, manufacturing of steel laminates into a core increases the iron losses [127].

Cryogenic cooling power The cryogenic cooling power is estimated as 0.5% of the rated power of the superconducting generator. This estimation is based on the technical report by GE for a low-temperature superconducting generator design [20], which calculated the cryogenic cooling power at different wind speeds. This report shows that the cryogenic cooling power is constant with wind speed and it value is 22.5 kW. Here we assume a constant cryogenic cooling power of 50 kW at all wind speeds. This power value is more than doubled 22.5 kW to consider a margin.

Converter losses The loss of the power electronic converter is modeled based on the current flowing in the power electronic switches [127] and given by

$$P_{conv}(v_w) = \frac{P_{convm}}{31}(1 + 10\frac{I_s(v_w)}{I_{sm}} + 5\frac{I_s^2(v_w)}{I_{sm}^2} + 10\frac{I_g(v_w)}{I_{gm}} + 5\frac{I_g^2(v_w)}{I_{gm}^2}) \tag{3.15}$$

where P_{convm} is the loss in the converter at rated power (assuming 2% of the rated power of the converter), I_s is the generator side converter current, I_{sm} is the maximum generator side converter current, I_g is the grid side converter current, and I_{gm} is the maximum grid side converter current.

ASSUMPTIONS FOR CALCULATING ENERGY PRODUCTION

A few assumptions apply to the calculation of losses:

- In an iron tooth and an iron armature yoke, only the fundamental radial and tangential components of the flux density are considered.

• Iron losses in the iron field core back and the iron pole cores are neglected.

• In copper conductors of an armature winding, only the fundamental radial and tangential components of the flux density are considered.

• For reducing eddy current losses in the armature winding, the copper conductors are only stranded with small filaments. Transposing or other means is not used.

• Iron losses and copper eddy current losses are both calculated at no load.

3.5.6. OPTIMIZATION

For the purpose of fair comparison, each of the twelve topologies need to be optimized for its lowest LCCoE. This optimization will find out how low the LCCoE can achieve in each topology. Optimization usually starts with a design which may not be optimum regarding a certain objective. Here we start optimization with a random set of design variables and the initial value of these design variables makes sense. Then the optimization program will search the whole space between the upper and lower limits of the design variables, being constrained by a few geometrical conditions.

OBJECTIVE FUNCTION

The objective function of optimization is the LCCoE which has already been defined by Eq. (3.3)

$$CoE' = \frac{C_{act} + C'_{other}}{a \cdot E_{AEP} \cdot T_{LT}} \tag{3.16}$$

where the active material cost C_{act} is changeable by varying the design variables and defined by

$$C_{act}(\mathbf{V}) = C_{SC} + C_{Cu} + C_{fy} + C_{fpc} + C_{at} + C_{ay} \tag{3.17}$$

where $\mathbf{V}$ is the variables to be optimized, C_{act}, C_{SC}, C_{Cu}, C_{fy}, C_{fpc}, C_{at} and C_{ay} are the costs of active materials, superconductor wires, field back core, field pole cores, armature teeth and armature yoke, respectively. The costs are determined from the unit usage of materials of the 2D FE model and multiplied by the unit cost. The length of the end winding of field and armature coils has been taken into account. The superconducting field coil is in the shape of racetrack and thus its end winding is modeled as semi-circles. The shape of the armature coil follows the conventional copper coil shape for a three-phase distributed winding.

This objective function is minimized by a generic algorithm NSGA-II [128], [129] which has been modified to this single-objective application. The optimization starts from a random set of variables [130] and takes 50 individuals and more than 100 generations to converge.

Table 3.4: Variables for optimization.

	Variable	Boundary
x_1	Number of pole pairs p	[2, 30]
x_2	Start angle of field coil α (elec. deg)	[10, 90]
x_3	End angle of field coil β (elec. deg)	[10, 90]
x_4	Height of field coil h_f (mm)	[10, 400]
x_5	Height of armature slot h_s (mm)	[10, 400]
x_6	Height of armature yoke h_{sy} (mm)	[10, 400]
x_7	Height of field back core h_{ry} (mm)	[10, 400]
x_8	Tooth width/slot pitch b_t/τ_s	[0.3, 0.7]

VARIABLES AND CONSTRAINTS

The variables to be optimized are summarized in Table 3.4 with their upper and lower limits. The definition of these variables can be found in Fig. 3.15. The angles α and β define the dimension and the position of a superconducting field coil. The ratio of the tooth width to the slot pitch b_t/τ_s defines the width of the armature teeth, which cannot be too large or too small.

Besides the upper and lower limits, five linear constraints are imposed to the variables:

$$\alpha - \beta < 0 \tag{3.18}$$

which ensures a positive dimension of the field coils,

$$h_s - h_{sy} < 0 \tag{3.19}$$

which makes the armature yoke sufficiently thick,

$$b_{t,min} - \pi r_s b_t/\tau_s/(mpq) < 0 \tag{3.20}$$

which ensures that the armature tooth width is no less than $b_{t,min} = 2$ cm,

$$k_{fil,arm} J_s h_s (1 - b_t/\tau_s) - K_a < 0 \tag{3.21}$$

which limits the specific electrical loading below $K_a = 75$ kA/m for applying forced-air cooling to the armature winding [123], and

$$r_{bend,min} - \pi\alpha(r_s - g_{eff} - h_f)/(180p) < 0 \tag{3.22}$$

which limits the bending radius of the superconducting wires above the specified minimum bending radius $r_{bend,min} = 100$ mm. The effective air gap length is the sum of the distance from the outer field winding to the air gap and the mechanical air gap length: $g_{eff} = h_{fg} + g$.

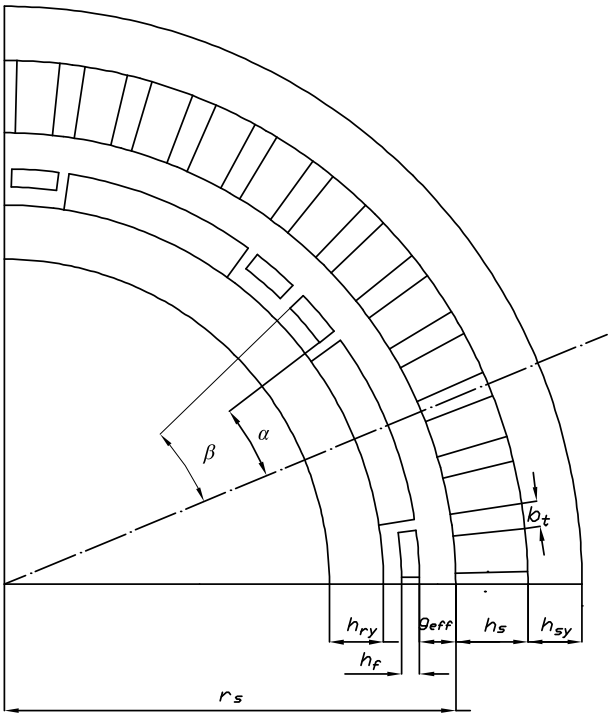

Figure 3.15: Geometrical variables and constants of the generator cross section. The symbols are defined in Table 3.2 and Table 3.4.

For the topologies T4, T8 and T12 which can employ modular cryostat, space around a superconducting field coil must be given and this space brings other linear geometrical constraints, depending on the size of the modular cryostat.

3.6. SCENARIO STUDY

3.6.1. WHY IS SCENARIO STUDY NEEDED?

SINCE superconductor technology is fast developing and superconducting generators for wind energy will take much time to become mature, only using the unit cost and performance of currently available MgB_2 superconductors could be too limited to provide long-term trends of topology comparison. Thus, three scenarios for the unit cost and performance of MgB_2 superconductors are taken into the comparison of PIs.

3.6.2. SCENARIO DESCRIPTION

The three scenarios to be studied are:

• Scenario 1 (S1): The unit cost of MgB_2 is reduced from 4 €/m to 1 €/m. This scenario considers the possible reduction of the price of MgB_2 in near future. Reduction of the price to a quarter is expected by MgB_2 suppliers (Columbus Superconductors) for certain mass production [57].

• Scenario 2 (S2): The critical current density of MgB_2 is increased to 4 times the currently available one. This scenario considers the possible enhancement of the critical characteristic of MgB_2. The order of 4 times is an assumption since MgB_2 suppliers can hardly predict it.

• Scenario 3 (S3): Both of the above. This scenario integrates both the unit cost and the critical current capability of MgB_2, which seems difficult to achieve in near future. It is an extreme case which can provide an insight of the topology comparison for future design.

As a reference, the original case (OR) based on currently available commercial MgB_2 wires (supplied by Columbus Superconductors) is used to show the present performance of the superconducting generator.

Each topology is optimized for its minimum CoE and has four sets of optimization results. The three scenarios will then be compared with each other and with the original one (OR).

The current density capabilities used in the original case and in Scenario 2 and 3 are plotted in Fig. 3.16.

3.7. RESULTS AND COMPARISON

3.7.1. OPTIMUM VARIABLES

THe LCCoE and a few resulting generator characteristics, such as the AEP, active material cost, active generator length, superconductor length and active material mass, are obtained from the twelve optimized topologies in the original case and the three scenarios.

The optimum value of the design variables is given in Table 3.5. The geometry and magnetic flux density of the optimized topologies in the original case (OR) is shown in Fig. 3.17. The topologies with more iron (T9-T12) have more pole pairs (18-24 pole pairs) than the other topologies (12-16 pole pairs). Different scenarios do not change much the number of pole pairs. The topologies with salient poles (T4, T8 and T12) have field coil pitches smaller than the pole pitches ($\beta < 90°$) since the modular cryostat occupies fixed space between two adjacent field coils.

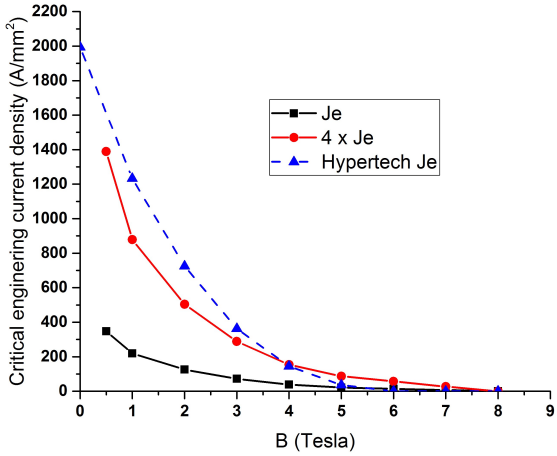

Figure 3.16: Critical current density of MgB_2 wires with respect to magnetic flux density used for the scenario study. The curve Je is the critical current density of the MgB_2 supplied by Columbus Superconductors, reproduced from [122]. The curve 4 x Je increases the original curve of Je to 4 times. Hypertech Je is reproduced from [25] and this curve was a short-term prediction in [25]. The curve of 4 x Je fits well the predicted curve of Hypertech Je.

3.7.2. COMPARISON

According to the optimization results for each of the twelve topologies for the three scenarios, the LCCoE, AEP, active material costs, active axial length, superconductor length, and active material masses can be obtained. These quantities are compared among the twelve topologies for the three scenarios, respectively, in Figs. 3.18-3.23.

LEVELIZED CAPITAL COST OF ENERGY

The LCCoE is compared among the twelve topologies for the four cases (the original case plus the three scenarios) in Fig. 3.18. In the original case, The general trend of LCCoE from T1 to T12 is decrease. The exception is T9 which has a fully ferromagnetic armature core but a fully non-magnetic field core. The topologies T1-T5 and T9 are relatively expensive in LCCoE, and T1 is the most expensive one. These 6 topologies have generally more non-magnetic cores than the other 6 topologies. The topologies T6-T8 and T10-T12 are relatively cheap in LCCoE, and T12 is the cheapest one. These six topologies have generally more ferromagnetic core than the other six topologies.

In the scenario study, all the three scenarios effectively reduce the LCCoE, especially for the topologies T1-T5 and T9 which have more non-magnetic cores. The reduction of LCCoE for T6-T8 and T10-T11 is limited. The effect is negligible for

Table 3.5: Optimum design variables resulting in lowest LCCoE for the scenarios: original (OR), 1/4 wire cost (S1), 4 times critical current density (S2) and combined S1 + S2 (S3).

	T1				T2				T3			
	OR	S1	S2	S3	OR	S1	S2	S3	OR	S1	S2	S3
p	12	12	12	12	12	12	14	12	14	12	14	12
α (°)	24	24	24	24	24	24	28	24	28	28	30	24
β (°)	90	90	90	90	90	90	90	90	90	90	90	90
h_f (mm)	16	36	10	18	14	28	10	18	16	30	10	18
h_s (mm)	60	60	60	40	74	58	64	42	68	58	64	42
h_{sy} (mm)	60	60	60	40	74	58	64	42	68	58	64	42
h_{ry} (mm)	60	60	60	40	162	182	182	62	158	190	180	58
b_t/τ_s	0.31	0.31	0.31	0.31	0.44	0.31	0.36	0.31	0.39	0.31	0.36	0.31
	T4				T5				T6			
	OR	S1	S2	S3	OR	S1	S2	S3	OR	S1	S2	S3
p	12	12	12	12	14	14	14	14	12	14	16	14
α (°)	38	40	40	26	28	28	28	28	34	28	42	30
β (°)	80	80	80	80	90	90	90	90	90	90	90	90
h_f (mm)	18	38	10	18	14	32	10	18	10	16	10	12
h_s (mm)	60	58	58	44	66	66	64	50	58	56	66	52
h_{sy} (mm)	62	58	58	44	92	114	120	52	240	228	226	206
h_{ry} (mm)	142	174	174	122	92	114	120	52	240	210	180	116
b_t/τ_s	0.31	0.31	0.31	0.31	0.37	0.37	0.36	0.36	0.31	0.36	0.41	0.36
	T7				T8				T9			
	OR	S1	S2	S3	OR	S1	S2	S3	OR	S1	S2	S3
p	14	14	16	14	12	14	14	14	18	20	20	22
α (°)	36	30	46	30	54	50	56	28	36	40	40	44
β (°)	90	90	90	90	80	78	78	78	90	90	90	90
h_f (mm)	10	16	10	12	10	24	10	12	14	34	10	18
h_s (mm)	58	56	64	52	52	54	56	50	78	100	94	100
h_{sy} (mm)	218	226	216	206	228	198	210	204	84	100	102	100
h_{ry} (mm)	222	210	178	116	222	178	196	124	84	100	102	100
b_t/τ_s	0.36	0.36	0.41	0.36	0.31	0.36	0.36	0.36	0.47	0.59	0.56	0.59
	T10				T11				T12			
	OR	S1	S2	S3	OR	S1	S2	S3	OR	S1	S2	S3
p	22	20	24	20	22	24	24	20	20	22	24	18
α (°)	48	40	58	40	56	48	64	42	66	64	66	46
β (°)	90	90	88	90	90	90	88	90	74	72	70	74
h_f (mm)	10	18	10	10	10	14	10	12	10	34	18	14
h_s (mm)	130	82	108	72	118	108	108	74	102	108	116	64
h_{sy} (mm)	134	156	124	172	130	122	122	174	122	128	126	158
h_{ry} (mm)	134	156	118	92	136	128	124	94	118	106	106	110
b_t/τ_s	0.68	0.53	0.62	0.53	0.65	0.62	0.62	0.53	0.65	0.62	0.65	0.47

T12. The scenarios are closing the difference of LCCoE among the topologies. The topologies T1-T5 and T9 become comparable to T6-T9 and T10-T12. However, the topologies with more ferromagnetic core are still cheaper in LCCoE for Scenarios 1

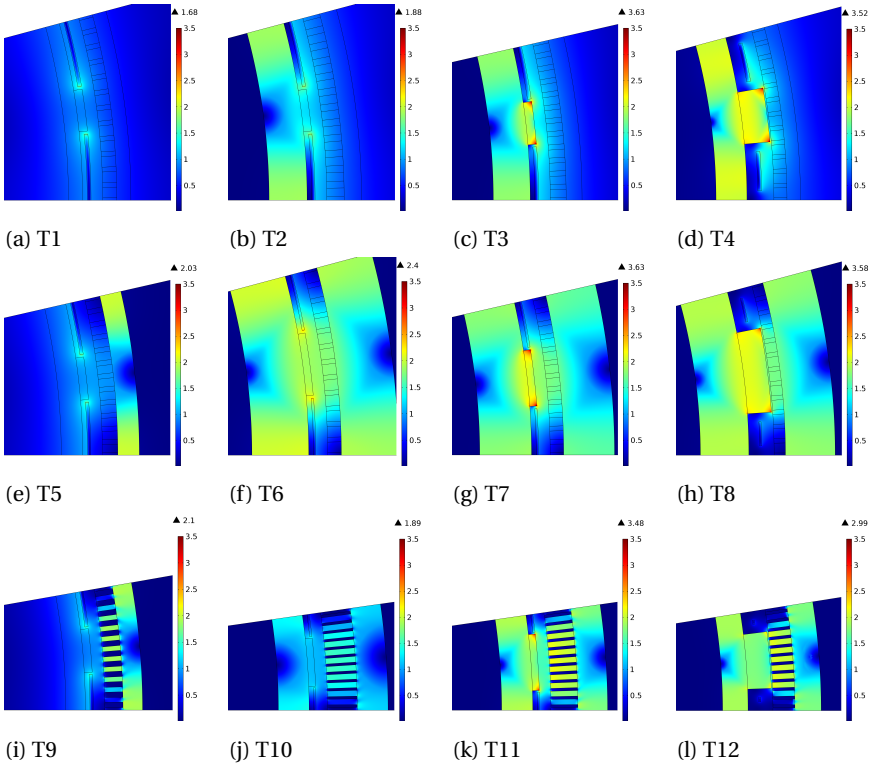

(a) T1 (b) T2 (c) T3 (d) T4

(e) T5 (f) T6 (g) T7 (h) T8

(i) T9 (j) T10 (k) T11 (l) T12

Figure 3.17: One pole of the optimized geometry and the corresponding distribution of magnetic flux density of the twelve optimized topologies in the original case (current unit cost and current density capability of the MgB_2 wire).

and 2, which are more suitable for wind energy conversion. Note that, however, the difference of topology is vanishing for Scenario 3. The topologies with more non-magnetic cores (T1-T5 and T9) will become competitive in Scenario 3.

ANNUAL ENERGY PRODUCTION

The AEP is compared among the twelve topologies for the four cases in Fig. 3.19. The information of AEP is extracted from and contained in CoE. In the original case, the general trend of AEP from T1 to T12 is increase. The exception is T9 which has a fully ferromagnetic armature core but a fully non-magnetic field core. The topologies T6-T8 and T10-T12 produce more AEP, and T12 produces the most. These 6 topologies have generally more ferromagnetic core than the other 6 topologies.

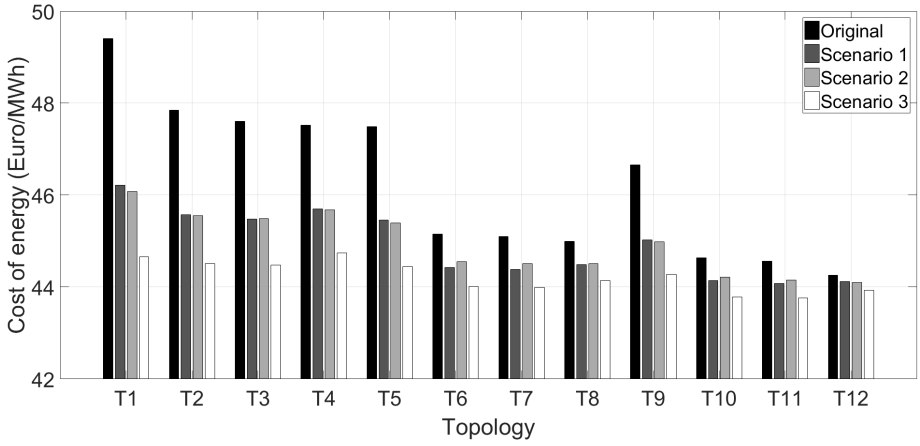

Figure 3.18: Comparison of capital cost of energy for twelve topologies.

In the scenario study, all the three scenario increase the AEP, especially for the topologies T1-T5 and T9 which have more non-magnetic cores. The effect is limited for T6-T8 and T10-T11 and negligible for T12. Like the result of CoE, the scenarios are closing the difference of AEP among the topologies. The topologies T1-T5 and T9 become comparable to T6-T9 and T10-T12. However, the topologies with more ferromagnetic core produce more energy for Scenarios 1 and 2, which are more suitable for wind energy conversion. Note that, however, the difference of topology is vanishing for Scenario 3.

ACTIVE MATERIAL COST

It is very interesting to study the active material costs for electromagnetic design of an electrical machine. Therefore, besides CoE we also compare the active material costs among the twelve topologies in Fig. 3.20. In the original case, the general trend of the total active material cost from T1 to T12 is decrease. The exception is T9 which has a fully ferromagnetic armature core but a fully non-magnetic field core. The topologies T1-T5 and T9 are relatively expensive regarding the total active material cost, and T1 is the most expensive one. These 6 topologies have generally more non-magnetic cores than the other 6 topologies. The topologies T6-T8 and T10-T12 are relatively cheap as contrast, and T12 is the cheapest one. These 6 topologies have generally more ferromagnetic core than the other 6 topologies. The fraction of the four active materials contributing to the active material cost is also shown in this figure. In most topologies, the MgB_2 superconductor takes up the majority or nearly half of the total active material cost. The cost of MgB_2 is minimized in T12 which

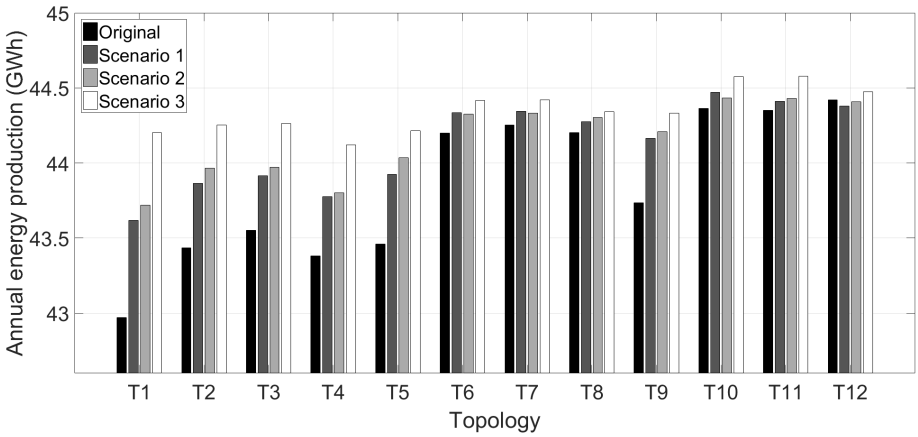

Figure 3.19: Comparison of annual energy production for twelve topologies.

makes most use of ferromagnetic cores.

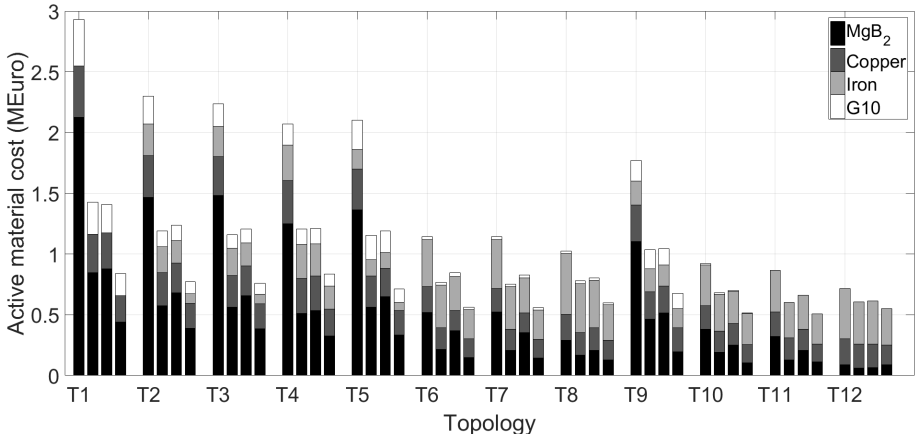

Figure 3.20: Comparison of active material costs for twelve topologies. From the left to right within a topology are original case, Scenario 1, Scenario 2 and Scenario 3.

In the scenario study, the result of active material cost is quite similar to that of CoE. The main drive of the cost reduction is the lower cost of MgB_2 since the cost of the other active materials remains with a slight difference.

ACTIVE AXIAL LENGTH

Since the air gap diameter of the generator is fixed to 6 m, the active axial length of the generator can be obtained for sizing the generator as shown in Fig. 3.21. In the original case, the topologies T6-T8 and T10-T12 result in a relatively short generator compared to the other six topologies. The shortest topology is T6 but actually the differences of length among T6-T8 and T10-T12 are very small. We can say all of the six topologies provide small generator lengths.

In the scenario study, the scenarios take effect in reducing the active axial length. Similarly, the topologies with more non-magnetic cores (T1-T5 and T9) are much more affected. Differently, Scenario 3 is not effectively closing the difference of topology in this case. The topologies with more ferromagnetic cores (T6-T8 and T10-T12) provide shorter machines.

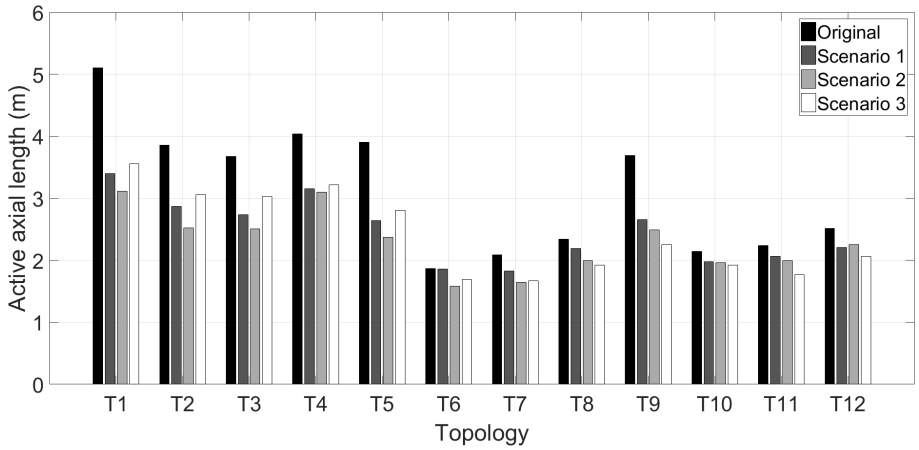

Figure 3.21: Comparison of active axial length for twelve topologies.

SUPERCONDUCTOR LENGTH

Not only does the length of used superconductor determine the active material cost, but it also indicate the difficulty in manufacturing the superconducting wire. A longer superconducting wire requires more complicated manufacturing technology and thus the manufacturing cost and wire quality may be significantly affected by the length of wire. The comparison of superconductor length in Fig. 3.22 shows clear trend.

In the original case, the topologies T6-T8 and T10-T12 require smaller superconductor lengths compared to the other 6 topologies. T12 requires the smallest length and thus has remarkable performance in reducing the length of superconductor.

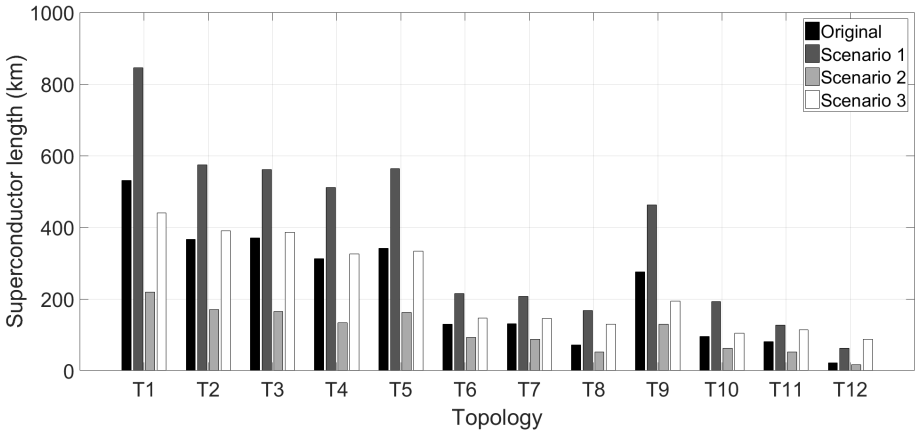

Figure 3.22: Comparison of superconductor length for twelve topologies.

In the scenario study, the result of superconductor length comparison is different from that of the above-mentioned quantities, because the unit cost or critical current density capability determines the amount of used superconductor. For example, Scenario 1 assumed a cheaper MgB_2 so the length of used MgB_2 goes much larger, but the difference is not as large as 4 times. Comparing Scenarios 1 and 2, a larger critical current density reduces the length of MgB_2 which makes sense, because less use of superconductor is needed to produce the same magnetic field intensity. From manufacturing difficulty point of view, Scenario 2 is more desirable since it results in a smaller length of superconductor.

ACTIVE MATERIAL MASS

Active material masses are also interesting for electromagnetic design. The comparison result is given in Fig. 3.23. In the original case, the topology T8 has the heaviest active material, because T8 uses a large amount of ferromagnetic iron. The trend from T2 to T12 is not so clear anymore, since the optimization has only dealt with cost and efficiency issue but the mass was not taken into account at all. From this sense, it is not correct to simply say that using ferromagnetic iron will increase the active material mass. Some topologies with more non-magnetic cores are also heavy, such as T2-T4, because they need a larger generator length to obtain the same power or torque, which brings more active materials and then a larger active material mass.

In the scenario study, the three scenarios effectively reduces the total active material mass. The comparison does not show a general trend from T1 to T12 for dif-

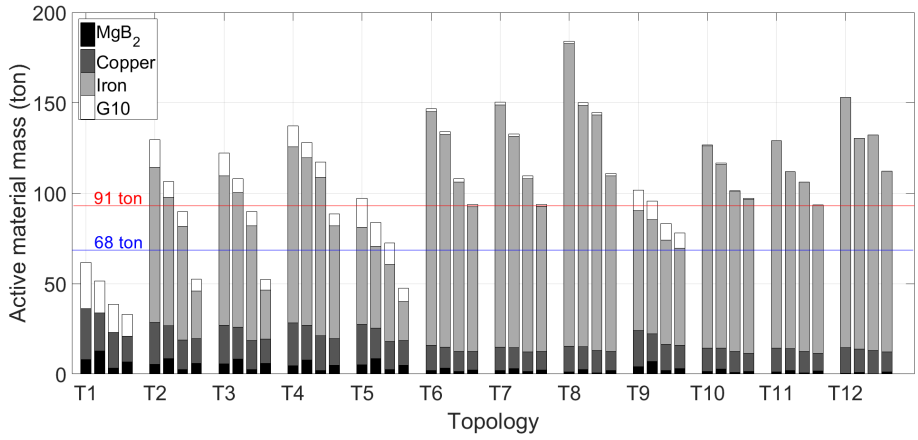

Figure 3.23: Comparison of active material mass for twelve topologies. From the left to right within a topology are original case, Scenario 1, Scenario 2 and Scenario 3. Reference low weights are shown by the red and blue lines.

ferent scenarios, but the topologies with more ferromagnetic cores tend to still be heavier than the other topologies. In addition, Scenario 3 is not effectively closing the difference of topologies.

A few reference generator masses can be introduced to define what a low weight is. One is the total mass of a 10 MW permanent magnet generator: $m_{PM} \approx 325$ ton [131]. One is the INNWIND.EU reference turbine drive train mass consisting of a medium speed gearbox and generator as well as the main shaft: $m_{innwind} \approx 227$ tons. [132]. The third is a reference total mass for a 10 MW SCSG design given in [133]. This reference mass indicates that a generator mass above 273 ton will significantly challenge the main bearing of the wind turbine rotor. The mass of 273 ton is about the average of m_{PM} and $m_{innwind}$. Therefore, this mass is used as a reference of low weight to evaluate the active material mass in Fig. 3.23. The active material mass could approximately be 1/3 to 1/4 of the generator mass (91 ton to 68 ton). This region of active material mass is also indicated in Fig. 3.23. In the original case, T1, T5 and T9 satisfy or almost satisfy 91 ton while only T1 satisfies 68 ton. None of the low-LCCoE topologies (T10-T12) meet these low weights. The scenarios result in more lightweight topologies. For example, T4, T6, T7, T10-T12 satisfy 91 tons and T1-T3 and T5 satisfy 68 ton in Scenario 3. However, the low-LCCoE topologies (T10-T12) are still far from 68 ton. The topologies that have a low LCCoE may not be good options for low weight. If low weight is essential, the topologies with more non-magnetic cores that have higher LCCoE should be considered.

3.8. DISCUSSIONS

3.8.1. LOSSES AND EFFICIENCY

PREVIOUSLY, we assumed a constant cryogenic cooling power of 50 kW, being 0.5% of the rated generator power. If sweeping this power from 0 to 1% of the rated generator power for the topology T12 in the original case, we obtain a series of generator system efficiency curves with respect to wind speeds in Fig. 3.24. The effect of the cryogenic cooling power on the efficiency mainly takes place at low wind speeds, i.e. partial load operations. If this power decreases, the partial load efficiency becomes higher. When the wind speed goes higher than the rated wind speed, the differences of efficiency become small. Due to the fact that wind turbines run at partial load most of the time, the energy production could be significantly increased by reducing the cryogenic cooling power.

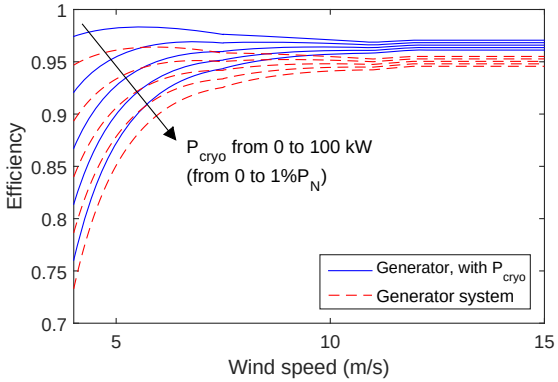

Figure 3.24: Effects of cryogenic cooling power on efficiency.

3.8.2. CONSIDERATION FOR REDUCING THE ACTIVE MATERIAL MASS

In the optimization for a minimum LCCoE, we did not consider any constraints on the active material mass. The optimization resulted in a large active material mass in some topologies with ferromagnetic cores (e.g. T6-T8). As explained before, the cost of energy is the first priority for the design of superconducting generators and the generator mass or the top head mass of the wind turbine may not be of major importance. In large wind turbines of 10-20 MW, the rotational speed of the rotor is quite low (below 10 rpm) which may cause mechanical stability issues on the turbine due to resonance. A large generator mass or top head mass may help decrease the natural frequency of the turbine and reduce the possibility of resonance.

In electrical machine design engineering, however, generator mass is always an

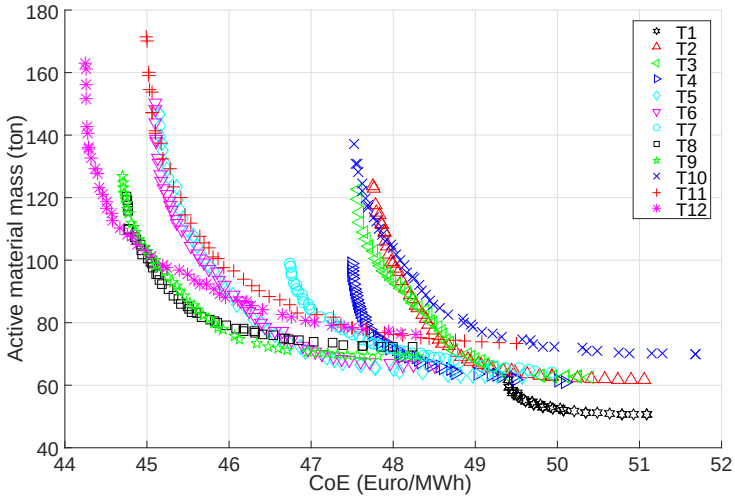

Figure 3.25: Trend of active material mass with variation of cost of energy for the twelve topologies.

important PI. The active material mass is indicative for the total generator mass, which needs consideration for evaluating an electromagnetic design. Here, we take into account the active material mass and find the conflicting relation between the total active material mass and the LCCoE for all the twelve topologies in the original case. These relations were obtained by a dual-objective optimization which uses both the total active material mass and the LCCoE as the objective functions.

The result is plotted in Fig. 3.25. This figure has the following indications:

• It shows the reachable boundaries of LCCoE and active material mass for each of the twelve topologies. For example, it is too hard for T12 to reach the total active material mass of 70 ton. The lower limit of LCCoE of T11 is about 45 €/MWh.

• With the same total active material mass, the difference or ranking of the LCCoE of the twelve topologies can be clearly observed. With the same LCCoE, the heavier or lighter topologies can be identified.

• It shows how much the LCCoE needs increasing to achieve certain reduction of the total active material mass, or how much active material mass need increasing for a lower LCCoE. For example, the total active material mass of T12 can be reduced from 160 ton to 120 ton by increasing the LCCoE by less than 1%. Some topologies have a very steep change of active material mass near the minimum LCCoE region, and a small increase of LCCoE can result in a large reduction of the active material mass. This relation in Fig. 3.25 will be useful as a design reference if the generator

mass is also critical. In this chapter, we only focus on designing for a low LCCoE and the generator mass is considered less important.

3.9. CONCLUSION

THIS chapter compared twelve topologies for superconducting generator design, regarding the key performance indicator of LCCoE for a 10 MW wind turbine. Some other generator characteristics resulting from the capital-CoE-based optimal designs are also shown. The LCCoE was estimated and modeled. Each topology was optimized for its minimum LCCoE. The LCCoE and other generator characteristics of the optimum design were then compared. With the commercial MgB_2 wire in the field winding and based on the its current unit cost and characteristic, the topologies with more iron have lower LCCoEs than the other topologies with more non-magnetic cores. The fully iron-cored topology with salient poles is most advantageous regarding the LCCoE as well as the resulting AEP, active material cost and superconductor length.

As indicated in the scenario study, reducing the unit cost to a quarter or enhancing the current density capability to 4 times of the MgB_2 wire can effectively lower the LCCoE for all the topologies, especially those with more non-magnetic cores. If both these scenarios are combined as a long-term scenario, the difference of the LCCoE between the topologies will become very small. Then the topologies with more non-magnetic cores will become comparable to those with more iron. Aiming at a lower LCCoE, however, those topologies having the most iron are still the most promising candidates for both now and the long term, although they could result in large generator masses. If low weight is required, the topologies with more non-magnetic cores should be taken into account.

4

RIPPLE FIELD AC LOSSES IN MgB_2 SUPERCONDUCTING FIELD WINDINGS

Study in this chapter has been published in:
- D. Liu, H. Polinder, N. Magnusson, J. Schellevis and A. B. Abrahamsen, "Ripple field AC losses in 10-MW wind turbine generators with a MgB_2 superconducting field winding," *IEEE Transactions on Applied Superconductivity*, vol. 26, no. 3, pp. 1-5, April 2016.

4.1. INTRODUCTION

PARTIALLY superconducting (SC) generators have SC windings in the DC field winding and copper windings in the AC armature winding. This configuration aims at avoiding excessive AC losses appearing in presently available superconductors under AC conditions [25, 26, 67].

However, the DC field winding will also be exposed to a certain AC magnetic field ripple due to time and space harmonics. In the generator design phase the AC loss caused by this ripple field needs to be evaluated to assure both the avoidance of local overheating and the operation at a tolerable overall AC loss level. Consider that the power input to the cryogenic system, as a rule of thumb, should not exceed 1% of the power rating of the turbine to ensure an overall drive train efficiency around 95% [15]. The proportion of the power for cooling the ripple field loss cannot exceed one tenth of that, corresponding to 10 kW for a 10 MW generator. This is roughly estimated based on the fact that the majority of the cooling power consumption comes from other sources, e.g. conduction and radiation of heat. The ripple field loss, which is considered as a minor heat contributor, must be kept sufficiently small.

From the ripple field point of view there are several machine designs to consider. The use of ferromagnetic or non-magnetic armature teeth is of particular interest. Whereas non-magnetic teeth require more SC wires, ferromagnetic teeth introduce slotting effects which contribute significantly to the level of the magnetic field ripple [29], [119]. From the conclusions of Chapter 3, we see fully iron-cored topologies with iron teeth show better overall performance especially lower capital CoEs. However, their iron teeth could lead to unacceptable AC losses in the SC field winding, which needs to be evaluated in this chapter.

Another important design aspect to be studied in this chapter is the possibility to use an electromagnetic (EM) shield to reduce the influence of space harmonics on the field winding. Time harmonics in the armature currents are not considered in this study, because the power electronic converter with its filters can be independently designed for a very small harmonic content.

The objective of this chapter is to determine the applicability of different design solutions in terms of AC losses by estimating the AC loss level of 10 MW wind generator designs employing an MgB_2 SC field winding. The effects on AC losses are compared between non-magnetic and ferromagnetic teeth with different numbers of slots per pole per phase. The feasibility of the fully iron-cored topology with salient poles is evaluated from the AC loss perspective. The necessity of an EM shield is also evaluated based on the obtained loss levels.

Table 4.1: Basic generator design parameters based on the optimized topologies T8 and T12 from Chapter 3.

Parameter	NMT design	IT design
Nominal power P_N	10 MW	
Nominal torque T_N	10.6 MN·m	
Rated speed n_N	9.6 rpm	
No-load line voltage V_{Nl}	3300 V	
Specific electrical loading K	75 kA/m	
Mechanical air gap length g	6 mm	
Distance from field coil to air gap	50 mm	
Cryogenic temperature	20 K	
Armature bore diameter d_s	6 m	
Axial length l_s	2.34 m	2.56 m
Pole pair number p	12	20
Frequency at rated speed f_N	1.92 Hz	3.22 Hz
Field current density J_f	150 A/mm^2	175 A/mm^2
Field coil side dimension $h_f \times w_f$	10×111 mm^2	10×20 mm^2
Specific magnetic loading B	1.00 T	0.96 T
Number of turns per field coil	462	85
Armature slot height h_s	52 mm	102 mm
Ratio tooth width to slot pitch b_t/τ_s	0.31	0.65
MgB_2 wire length in slots l_{SC}	72.05 km	21.77 km

4.2. GENERATOR DESCRIPTION

4.2.1. GENERAL DESIGN

The 10 MW three-phase generator to be studied is based on the optimized topologies T8 and T12 from Chapter 3. The generator has an MgB_2 SC field winding and employs a salient iron core for the field poles with an iron field back core. The armature yoke is also made from iron to confine the magnetic field inside the generator. Using iron cores can significantly reduce the cost and size of the generator [30], even if the iron is heavily saturated. Using salient iron poles maximally shortens the effective air gap length. The SC field coils are accommodated in modular cryostats around the salient poles. Each cryostat has only one field coil and this allows for easy maintenance and replacement of one module. Such a topology minimizes the cold mass and to some extent frees the position of the field coils in the radial direction [23].

The armature tooth material can be ferromagnetic or non-magnetic. The de-

signs with non-magnetic teeth (NMT) and iron teeth (IT) have been optimized for minimizing the capital cost of energy (CoE) of a 10 MW reference wind turbine in Chapter 3. In Chapter 3, the corresponding topologies are T8 and T12 for the NMT and the IT designs, respectively. The magnetic properties of the used armature core for the IT design are similar to those of M14 steel laminates [134]. The maximum flux density in the armature teeth for the IT design is 2.1 T. The basic design parameters of the two optimized designs are summarized in Table 4.1, and the optimal geometry of one pole of each design is plotted in Fig. 4.2 with no load flux densities.

Compared with non-magnetic teeth, ferromagnetic teeth introduce slotting effects which produce field harmonics in the field winding. However, the use of ferromagnetic teeth significantly reduces the reluctance of the machine, and therefore the generator length can become smaller [30]. To obtain a comparable generator length with non-magnetic teeth instead, much longer SC wires have to be used, as indicated in Table 4.1.

The number of slots per pole per phase q is an important factor for ferromagnetic teeth. A larger q means less slot effects but narrower teeth. The original machine design has $q = 4$ which is then modified to $q = 2$, 3 and 5 for analyzing its effects on AC losses. The number of q does not change the parameters shown in Table 4.1.

An EM shield can be used for screening the field harmonics from the armature. Usually this shield is part of a cryostat and made from a conductive metal, e.g. copper, aluminum. At the same time of screening harmonics, however, eddy current losses are induced by these harmonics. There should thus be a trade-off between the shielding effect and the eddy current loss production if an EM shield is required. The placement of the EM shield is illustrated in Fig. 4.1.

4.2.2. MAGNETIC FIELD

The magnetic field is computed without an EM shield in a 2D finite element model as shown in Fig. 4.2. This model applies a uniform current density in the field winding and the armature winding has a rated three-phase current to obtain the maximum torque. The field is a superposition of a DC field and AC field harmonics. The DC field determines the critical current density of an SC wire and the AC fields determine the AC losses. This machine model does not model the wires' superconductivity properties but only computes the external fields transverse to an SC wire.

For instance, the AC field components of the NMT design and the IT design with $q = 5$ at one point (Point M) in the field coil are illustrated in Fig. 4.3, in the form of time variation and frequency spectrum. In the NMT design only the 6th (11.52 Hz) and the 12th (23.04 Hz) harmonic appear, whereas in the IT design the 18th (57.60 Hz), 24th (76.80 Hz) and 30th (96.00 Hz) harmonics also contribute with the 6th

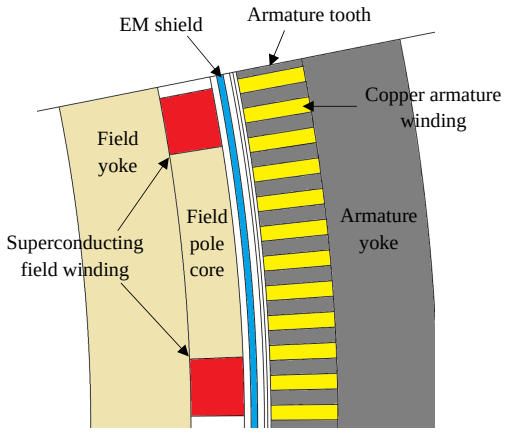

Figure 4.1: Sketch of the EM shield between the rotor and stator of a superconducting generator (taking the topology with non-magnetic rotor core as an example).

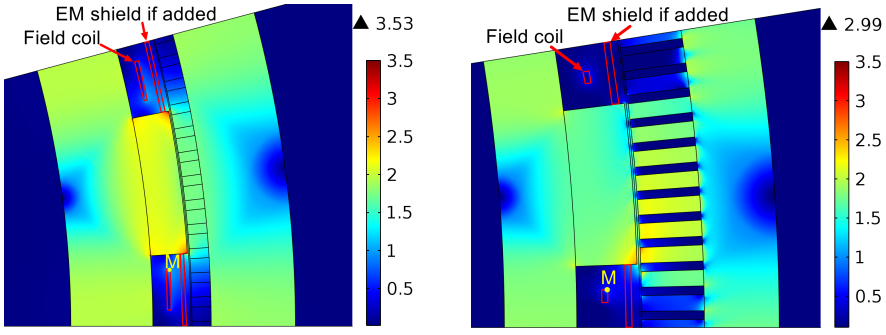

(a) NMT design

(b) IT design

Figure 4.2: Generator geometries with non-magnetic teeth (a) and ferromagnetic teeth (b). Magnetic flux density [T] in no load is shown by colorbar.

(19.20 Hz) and 12th (38.40 Hz) harmonics. In both of the designs the 6th harmonic dominates.

4.2.3. SUPERCONDUCTING WIRE

The cross-section of the employed MgB_2 wire (supplied by Columbus Superconductors [57]) is shown in Fig. 4.4a. The SC wire has 19 MgB_2 filaments embedded, and arranged approximately elliptically, in a nickel matrix. The fill factor is 21.5% and

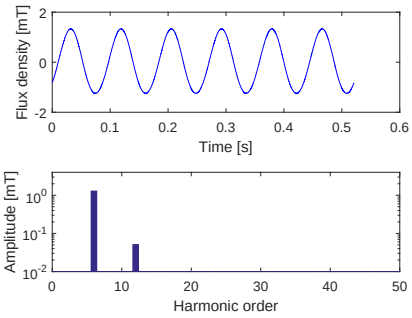

(a) NMT, radial component

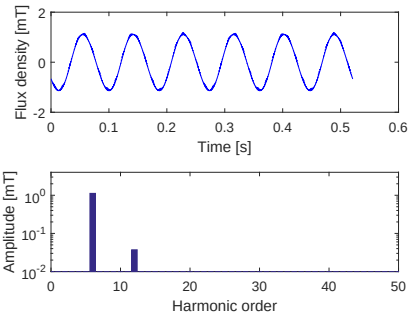

(b) NMT, tangential component

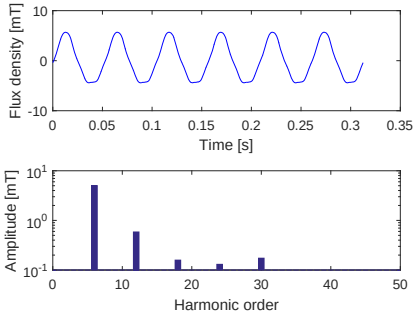

(c) IT, radial component

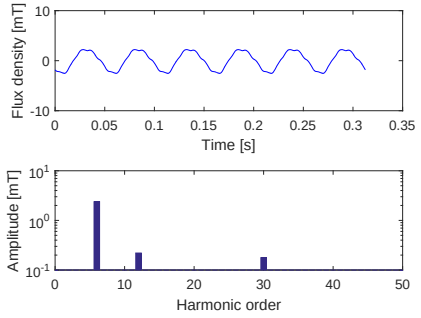

(d) IT, tangential component

Figure 4.3: AC component of flux density in one cycle and its frequency spectrum of the harmonics at Point M (marked in Fig. 4.2) in the field winding ($q = 5$).

the twist pitch is 0.3 m. The dimension is 0.5 mm x 3 mm with an additional 0.2 mm thick copper strip soldered to one longer side of the wire. The critical engineering current density for the NMT design is $J_e = 200$ A/mm^2 and for the IT design is $J_e = 239$ A/mm^2. The wires are operated with a safety margin of 25% to the critical engineering current density [122].

4.3. AC LOSS MODELING

4.3.1. APPROACH

THe models consider the AC losses produced in the SC field winding. Other losses within the cryogenic environment, i.e. losses in electrically conductive structures, are not considered.

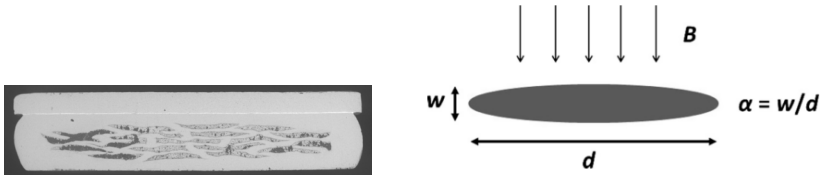

(a) (b)

Figure 4.4: Modeling of the SC wire. (a) Cross-section (3 mm wide). (b) Definition of the dimensions for the elliptical filament core region in an applied field B. B appear as perpendicular for $\alpha < 1$ and parallel for $\alpha > 1$ [32].

To estimate the AC losses due to ripple magnetic fields we apply 2D analytical hysteresis and coupling loss models as outlined below. The models are generally non-linear in magnetic field and valid for one frequency only. For the generator case, with one or a few contributing ripple frequencies, a good approximation is obtained by considering the harmonic(s) with the largest amplitude. This approximation can be supported by the following reasoning. When the ripple field is partially penetrating the superconductor, the hysteresis loss is proportional to the frequency but roughly proportional to the cube of the amplitude of the ripple field. With such partial field penetration, the coupling loss for long twist pitches is irrelevant to the frequency but proportional to the square of the amplitude of the ripple field. The AC losses are therefore much more sensitive to the amplitude than to the frequency.

To check the validity of this approximation, the AC losses will not be presented in the form of a value but a range. The loss due to the harmonic with the largest amplitude (one frequency only) is considered as the lower boundary of the loss range, and the loss due to all the most contributing frequencies are summed as the upper limit. If the range of losses turns out to be small, the harmonic with the largest amplitude can be used for estimating the AC losses.

In addition to wire dimensions and properties, the frequency and transverse magnetic field from Section 4.2 are used as input parameters to the AC loss models. As the magnetic field varies over one field coil, the cross-section of one coil is divided equally into 64 segments in which the AC loss is calculated individually. Then the results are summed to obtain the loss over the entire field coil and the entire field winding, assuming that the 2D analysis is identical along the generator length.

In our calculations we omit the end field winding, since in end winding regions longitudinal fields also exist but the slotting effect due to iron teeth becomes much weaker.

4.3.2. HYSTERESIS LOSS

Hysteresis losses are commonly modeled based on the critical state model [135], [136] and analytical expressions are available for simple geometries [137], [138]. Here we base our model on the work in [32], which in turn was based on the work by ten Haken et. al [139]. The model considers elliptical cross-sections of the filament region with arbitrary aspect ratios (see Fig. 4.4b). By setting the aspect ratio α above or below unity, magnetic fields parallel or perpendicular to the wire face are considered.

In the low field range (agreeing with this study), the loss becomes proportional to the cube of the ripple field and it becomes independent of the DC current, whereas the DC magnetic field influences the loss by its influence on the critical current (density). The hysteresis loss per unit length is:

$$P_{h0} = f A M_p B_p(\alpha) Q(B_{ac}), \tag{4.1}$$

where f is the frequency, A is the conductor area as given in Fig. 4.4b, M_p is the magnetization of the fully penetrated ellipsis, B_p is the field of full penetration depending on the aspect ratio α, and Q is the normalized energy loss per cycle of the AC magnetic flux density B_{ac} [32], [139].

The loss is calculated for parallel and perpendicular magnetic fields separately using the respective field components. These losses are then summed as an approximation which gives good accuracy in most of the winding [32].

4.3.3. COUPLING LOSS

Carr [137] developed a coupling loss model for a round wire in slowly changing magnetic fields. This model takes into account the case with a relatively long twist pitch, and therefore it can be applied to the MgB_2 wires in this study. To adapt to the shape of the wire for the model, the filament core region is approximated to be round by keeping the same cross-sectional area of the filament region. This approximation can be justified since the filaments operate in the fully coupled and low field region, where the coupling loss becomes determined by the full screening current passing the matrix twice every twist pitch (and the degree of coupling do not change with wire dimensions). The loss per unit length is given by

$$P_{c0} = \frac{8\pi^3 R_0^2 B_{ac}^2}{\mu_0^2 \sigma_\perp l_t^2}, \tag{4.2}$$

This is only valid for the frequency f of the ripple field fulfilling $\frac{1}{2\pi\sigma_\perp \mu_0 R_0^2} \geq f \geq \frac{4\pi}{l_t^2 \mu_0 \sigma_\perp}$, where l_t is the twist pitch, $R_0 = 0.463$ mm is the equivalent radius of the filament core region and $\sigma_\perp = 12.8 \times 10^7$ S/m is the transverse conductivity with no

contact resistance at 20 K. In this special case, the coupling loss is independent of frequency. The frequencies of the NMT and IT designs meet this range, so we can use Eq. (4.2) to estimate the coupling loss for the both designs.

4.4. RESULT AND DISCUSSION

Using the models Eqs. (4.1) and (4.2), the hysteresis loss and the coupling loss are calculated for the case with non-magnetic or ferromagnetic teeth and different q numbers. An EM shield is absent in all the cases. The distribution of the obtained hysteresis loss and coupling loss is plotted in Fig. 4.5 for the IT design with $q = 2$ for instance. It can be observed that one field coil side has more AC losses than the other and that more losses are produced in the regions closer to the armature.

The range of total AC losses with different numbers of q is shown in Fig. 4.6a, compared for the NMT and IT designs. The total AC loss is the sum of the hysteresis and coupling losses. Higher AC losses result from ferromagnetic teeth, but they are very small especially when q increases. The ranges of total AC losses are very small except for the IT design with $q = 2$. This proves the validity of the approximation for AC losses with a large q by using the field harmonic with the largest amplitude.

If the cryogenic cooling penalty factor at the temperature of 20 K is assumed as 1000, the required power at room temperature to cool the amount of AC losses for the IT design with $q = 2$ (the worst case in this comparison) will be no more than 9.1 kW. The currently available cryogenic refrigeration technology is capable of handling this power. Moreover, the reduction of generator efficiency due to this cooling power demand is negligibly small (less than 0.1% of 10 MW).

The employed analytical models for calculating the AC losses may not be sufficiently accurate since some assumptions and simplifications are used. If we assume a huge error of the models which increases the total AC loss by an order of magnitude, the required cryogenic cooling power for the IT design with $q = 2$ will be 91 kW which is almost 1% of the rated generator power. This cooling power may be too high. Then the number of slots per pole per phase can be increased to $q = 4$ and the cooling power will drop to only 31 kW which is about 0.3% of the rated generator power. This level of cooling power is considered acceptable in terms of both cooling system capability and sufficient efficiency.

The results also imply that it is not necessary to place an EM shield for reducing AC losses in normal operation. Firstly, with an EM shield the AC losses cannot be beneficially reduced, since the AC losses have already been very small. Secondly, placing an EM shield will introduce eddy current losses which could be much higher than the power demand for cooling the AC losses.

For testing purposes, a 10 mm thick copper shield is placed 10 mm far from the air gap, as shown in Fig. 4.2. The width of the shield occupies the width between two

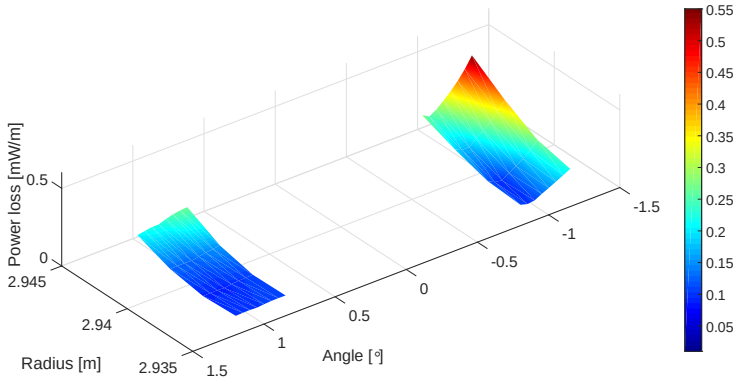

(a) Hysteresis loss

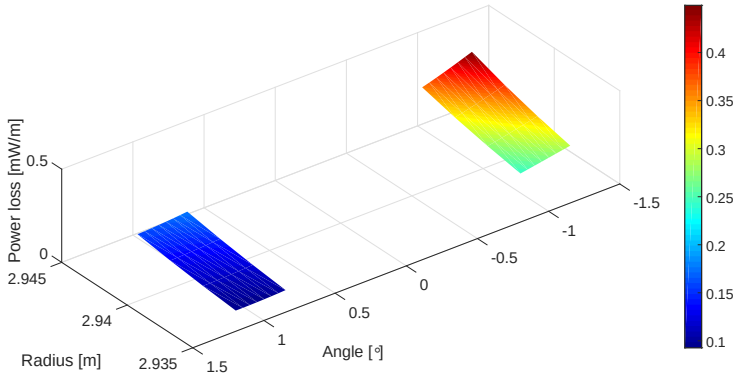

(b) Coupling loss

Figure 4.5: AC loss distribution in a field coil for the IT design, along the radial position and the circumferential angle of the generator, with $q = 2$.

adjacent poles. After adding this EM shield, the amplitudes of the five dominant field harmonics are all reduced. However, as indicated in Fig. 4.6b, the IT design with $q = 4$ and an EM shield produces an 8 kW loss in the shield, which is more than 2 times the power for cooling the corresponding AC loss (assuming a cryogenic cooling penalty factor of 1000).

Apparently, a larger q also reduces the loss in an EM shield because of less slotting harmonics. In terms of cryostat design, if conductive parts are inevitable between the field winding and the armature, the eddy current loss in such conductive parts can be reduced by using a larger q or non-magnetic teeth [119]. It is possible

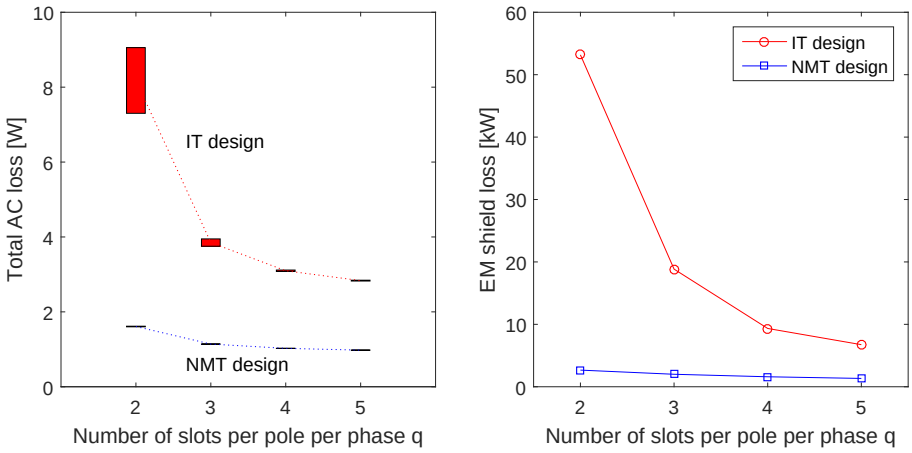

(a) Total AC losses (b) Total EM shield losses

Figure 4.6: Total AC losses and EM shield losses as a function of q.

to design an optimal EM shield for both low eddy current losses and good shielding effects, but this issue is beyond the scope of this chapter.

This low level of AC losses is obtained from the specific generator design described in Section 4.2. This design has a relatively large distance between the field winding and the armature because of the limitation of cryostat dimensions. If this distance is made smaller, the field harmonic contents will become higher and more AC losses will occur. Moreover, this design also has relatively wide teeth due to the fact that the machine optimization has found a balance between the saturation of teeth and the minimization of capital CoE.

4.5. CONCLUSION

THe models of hysteresis losses and coupling losses in a multi-filamentary strip MgB_2 wire were described and then applied to calculate the AC losses in two 10 MW SC wind generator designs. The results show

• that this generator design has a very small amount of AC losses with ferromagnetic teeth and without an EM shield, and

• that a larger number of slots per pole per phase q results in lower AC losses.

The results provide two important machine design suggestions. One is that the amount of AC losses produced by ferromagnetic teeth can be very small for an SC machine design, which implies that the fully iron-cored topology is feasible from

the perspective of AC loss production in the SC field winding. The other suggestion is that an EM shield can be unnecessary for AC loss reduction in normal operations. Conductive parts should thus be avoided as much between the field winding and the armature to minimize the induced eddy current losses. If conductive parts are inevitable, ferromagnetic teeth with a large q or non-magnetic teeth can be considered.

5

REDUCING THE SHORT CIRCUIT TORQUE

Part of this chapter has been published in:

- D. Liu, H. Polinder, A. B. Abrahamsen, and J. A. Ferreira, "Effects of armature winding segmentation with multiple converters on the short circuit torque of 10-MW superconducting wind turbine generators," *IEEE Transactions on Applied Superconductivity*, vol. 47, no. 4, pp.1-5, 2017.

- D. Liu, H. Polinder, A. B. Abrahamsen and J. A. Ferreira, "Effects of an electromagnetic shield and armature teeth on the short-circuit performance of a direct drive superconducting generator for 10 MW wind turbines", 2015 IEEE International Electric Machines & Drives Conference (IEMDC), Coeur d'Alene, USA, 2015, pp. 709-714.

5.1. INTRODUCTION

Superconducting machines usually have larger magnetic air gaps than conventional generators because of space for a cryostat or use of non-magnetic cores. As a result, the inductance becomes lower and then the short circuit torque can become as high as more than 10 times the rated torque which is too high for wind turbine constructions.

A few approaches can be considered to reduce the short circuit torque. Since the sub-transient reactance of a synchronous generator determines the peak short circuit current, an electromagnetic (EM) shield between the rotor and stator could play a role to reduce the short circuit torque. An EM shield being part of the cryostat wall, as sketched in Fig. 4.1, is recommended to be used in a superconducting (SC) machine to attenuate harmonic magnetic fields from the armature to the field winding [118]. In an EM shield which is electrically conductive, eddy currents are induced during an armature winding short circuit. The eddy currents then excite magnetic fields to oppose the change of the air gap field. This reaction determines the sub-transient reactance X_d'' of an SC synchronous machine and then the short-circuit current and torque. In general, the larger the sub-transient reactance X_d'', the smaller the short-circuit current.

In addition, ferromagnetic core or multiple armature windings could be useful to reduce the short circuit torque [33]. Using ferromagnetic core increases the inductance. Using multiple armature windings assumes that not all the armature winding but only part of it is shorted since the chance of shorting all the armature segments at the same time is too low.

Multiple or, as we call it, segmented armature windings can be realized in a wind turbine by being connected to multiple back-to-back power electronic converters, as illustrated in Fig. 5.1. Each armature winding segment is connected to an individual converter. This generator system has been proposed in the INNWIND.EU project and performance indicators are evaluated in [140].

This chapter aims at assessing the effects of EM shields and armature segmentation on reducing the short circuit torque of SC synchronous generators (SCSGs). These SCSG designs have different topologies which change the combination of iron and non-magnetic cores. The calculation of short circuit torque uses FE methods (FE) methods which can model saturation changes during a short circuit.

5.2. FOUR GENERATOR DESIGNS

Four of the twelve topologies discussed in Chapter 3 have been proposed for 10 MW SCSGs in a few recent research projects. This chapter studies four 10 MW generator designs employing these four topologies, as illustrated in Fig. 5.2.

Design A (based on the optimized topology T5 from Chapter 3) is considered

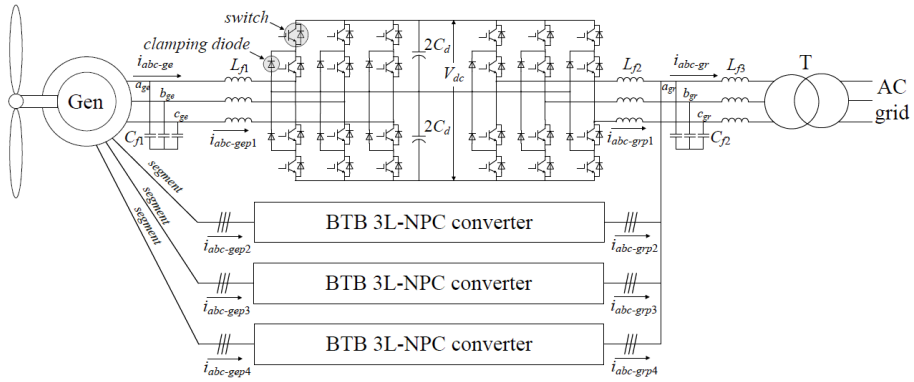

Figure 5.1: Block diagram of multiple power electronic converters for a 4-segments generator. [140]

as an air-core concept since all the cores but the armature yoke are non-magnetic. This concept is proposed in [122] for a 10 MW SCSG design. The advantage of this topology is low weight and no slotting effects. However, a large amount of SC wires is required to excite sufficient magnetic fields. Due to the non-magnetic core for the field winding, it is not possible to use salient poles.

Design B (based on the optimized topology T9 from Chapter 3) is considered as an air-rotor concept since the cores for the field winding are all non-magnetic while the cores for the armature winding are all made of steel laminates. This concept is proposed in [20] for a 10 MW SCSG design. The advantage of this topology is that laminate cores used in conventional generators can directly be used. However, a large amount of SC wires is also demanded and slotting effects exist due to iron teeth. This concept cannot use salient poles either.

Design C (based on the optimized topology T8 from Chapter 3) is considered as an air-winding concept since only the armature teeth are non-magnetic while all the other cores are made of iron. Salient poles can be used in this topology to minimize the distance between the field winding core to the armature winding. To apply this topology, modular cryostats have to be used as proposed by [23]. The main advantages of this topology are a small magnetic air gap and no slotting effects. The use of SC wires is effectively reduced compared to the designs A and B. However, non-magnetic teeth require special cooling methods since non-magnetic materials, e.g. glass fiber G10, are bad at thermal conduction.

Design D (based on the optimized topology T12 from Chapter 3) is considered as a fully iron-cored concept since all the cores are made of iron. This topology looks like conventional synchronous generators but the copper field winding is replaced

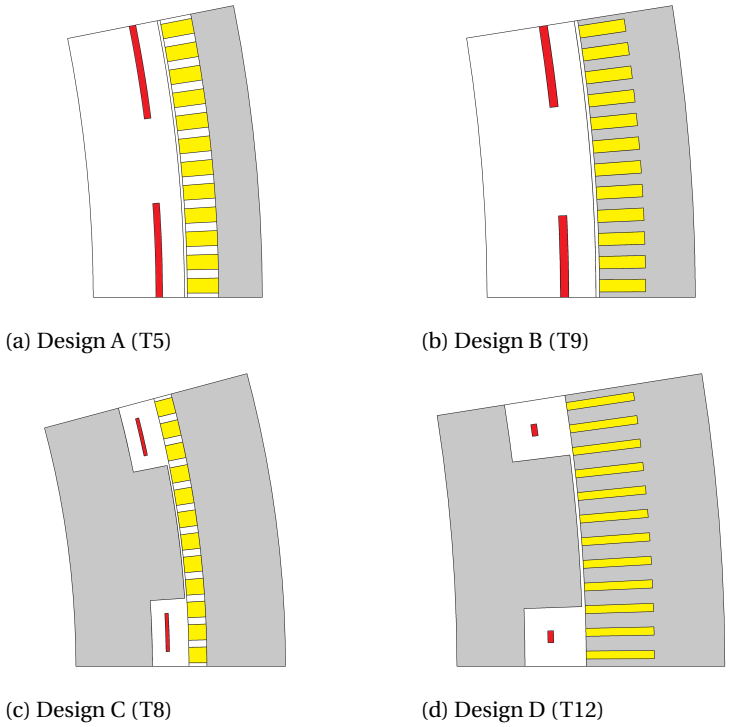

(a) Design A (T5)

(b) Design B (T9)

(c) Design C (T8)

(d) Design D (T12)

Figure 5.2: Sketch of one pole of the topology of the SCSG designs. Red: SC field winding. Yellow: copper armature winding. Gray: iron core.

by an SC winding. The steel laminates can directly used for the armature cores. Modular cryostats also have to be used to enable the salient poles. The amount of SC wires is significantly reduced compared to the designs A, B and C. The cost of this topology is thus not very high. However, this topology may be very heavy and slotting effects may cause high torque ripples. This concept has been studied in [30, 120] and Chapter 4 of this thesis from different perspectives.

Each design using MgB_2 field windings has been optimized for the minimum capital cost of energy in a 10 MW reference wind turbine as presented in Chapter 3. The optimal geometry of one pole is shown in Fig. 5.2. The design parameters are summarized in Table 5.1. The cryogenic temperature for the MgB_2 field winding is still 20 K. The electrical loading of the designs is still limited to 75 kA/m to enable forced-air cooling on the armature winding [123]. The chosen number of slots per

pole per phase $q = 4$ is both to avoid significant slotting effects and to have the armature teeth sufficiently wide.

Table 5.1: Main Parameters of Four Superconducting Generator Designs

Design	A	B	C	D
Nominal power P_N	10 MW			
Rated speed n_N	9.6 rpm			
No-load voltage V_n	1905 V			
Number of phases m	3			
Armature bore diameter d_s	6 m			
Mechanical air gap length g	6 mm			
Rated armature current density J_s	3 A/mm^2			
Slot number per pole per phase q	4			
Axial length l_s (m)	4.08	3.75	2.34	2.57
Pole pair number p	16	20	12	20
Foil coil height h_f (mm)	14	14	10	10
Foil coil side width w_f (mm)	200	139	111	20
Armature slot height h_s (mm)	66	78	52	118
Tooth width/slot pitch b_t/τ_s	0.37	0.47	0.31	0.65
Operating field current I_f (A)	206.6	197.5	239.4	280.3
Number of turns per phase N_a	128	128	110	128
Number of turns per field pole N_p	1163	810	463	85

5.3. MODELING OF SHORT CIRCUIT

THree-phase short circuits are modeled by 2D FE methods to calculate the short circuit torque. No damper winding is used outer the field winding. The model couples the computation of magnetic fields and the generator's equivalent circuit and is called field-circuit-coupled model. The field model computes the induced voltage $\frac{d\lambda_a}{dt}$, $\frac{d\lambda_b}{dt}$ and $\frac{d\lambda_c}{dt}$ over the three phases and $\frac{d\lambda_f}{dt}$ over the field winding due to the resultant air gap magnetic field (including every flux leakage). The circuit model is used to calculate the current flowing in each phase i_a, i_b and i_c and in the field winding i_f. The circuit model can be written as

$$u_a = \frac{d\lambda_a}{dt} - R_s i_a - L_{ews}\frac{di_a}{dt} \tag{5.1}$$

$$u_b = \frac{d\lambda_b}{dt} - R_s i_b - L_{ews}\frac{di_b}{dt} \tag{5.2}$$

$$u_c = \frac{d\lambda_c}{dt} - R_s i_c - L_{ews}\frac{di_c}{dt} \tag{5.3}$$

$$u_f = \frac{d\lambda_f}{dt} + R_f i_f + L_{ewf}\frac{di_f}{dt} \tag{5.4}$$

where $L_{\sigma ews}$ is the end winding inductance per phase of the armature winding, $L_{\sigma ewf}$ is the end winding inductance of the field winding, u_f is the terminal voltage of the field winding which is very small, R_s is the resistance per phase and R_f is the resistance of the field winding.

The end winding inductance per phase of the armature winding is calculated with analytical models given by [123]:

$$L_{ews} = \frac{4m}{Q} q N_s^2 \mu_0 l_w \lambda_w \tag{5.5}$$

where is the total number of slots, N_s is the number of turns per phase, and $l_w\lambda_w$ is calculated by

$$l_w\lambda_w = 2l_{ew}\lambda_{lew} + W_{ew}\lambda_W \tag{5.6}$$

where l_{ew} is the axial length of the end winding measure from the end of the stack, and W_{ew} is the coil span. λ_{lew} and λ_w are the corresponding permeance factors estimated in [123]. When the number of armature winding segments is N_{seg}, L_{ews} and R_s should be reduced to $1/N_{seg}$ time.

The end winding inductance of the field winding L_{ewf} is calculated by subtracting the inductances from 3D FE models by the inductance from 2D FE models. The resistance and the end winding inductances are summarized in Table 5.2. The field winding resistance R_f is caused by the small resistance in the current leads which are not superconducting [118].

Table 5.2: Resistances and End Winding Inductances

Design	A	B	C	D
End winding inductance L_{ews} (mH)	1.23	0.78	1.61	0.78
End winding inductance L_{ewf} (H)	15.2	10.2	8.6	2.4
Resistance R_s (mΩ)	54.1	48.1	34.7	36.4
Resistance R_f (mΩ)	20	20	20	20

The short circuit torque can be so high that the speed of an SCSG drops fast during a short circuit. The rotation of the generator is governed by

$$T_m - T_e = J\frac{d\omega_m}{dt} \tag{5.7}$$

where T_m is the mechanical torque driving the generator by the wind turbine. Since before the short circuit is there no load, this torque can be assumed to be $T_m = 0$ during the short circuit. T_e is the electromagnetic torque produced by the generator, and ω_m is the rotational speed of the generator. The moment of inertia J is estimated with a scaling function given in [141]:

$$J = \frac{14500}{9} P_N^{1.2} R_{tr}^2 \tag{5.8}$$

where P_N is the nominal power of the wind turbine in MW and R_{tr} m is the radius of the wind turbine rotor. In this chapter, we use a 10 MW reference wind turbine with a rotor diameter of 178 m [11].

The short circuit occurs in such a way that the generator's three phases are shorted at the terminal by applying zero voltages to u_a, u_b and u_c after a no-load operation of one electrical cycle. For assessing the effects armature winding segmentation on the short-circuit torque, no-load operation is sufficient which also simplifies FE modeling.

5.4. EFFECTS OF EM SHIELD

An EM shield is electrically conductive and usually the outer part of a cryostat wall. It cannot be placed too close to the SC field winding since it will introduce significant increase of thermal loads to the 20-K temperature dewar of the cryostat. Furthermore, the thickness of the EM shield cannot be too large. Otherwise the cryostat wall will push the field winding farther away from the armature winding to remain the same thermal insulation performance. This increase of distance of the field winding may not too much affect the topologies with salient iron pole but it will significantly affect the other topologies. As a result, four cases regarding the EM shield are compared:

- Case 1: the EM shield is placed just next to the 6-mm mechanical air gap and its thickness is 10 mm.

- Case 2: the EM shield is placed just next to the 6-mm mechanical air gap and its thickness is 20 mm.

- Case 3: the EM shield is placed 10 mm off the 6-mm mechanical air gap and its thickness is 10 mm. This case is chosen for comparison but it is less practical since the EM shield may go to the space of a lower temperature. The generated heat in the EM shield may significantly increase the thermal loads within the cryostat.

- Reference case: no EM shield is used.

The material of the EM shield is copper. Its conductivity is set to be 42.9 MS/m, assuming a working temperature of 120 °C. Using this conductivity assumes that the outer cryostat wall operates in a room-temperature environment since it is close to the mechanical air gap.

RESULTS

Designs A and B are investigated. The electromagnetic torques during the short circuit (five electrical cycles of rated frequency) in the four cases for Designs A and B are shown in Fig. 5.3. The effects of EM shield on reducing the peak torque are compared in Fig. 5.4. The effects of EM shield in Cases 1 and 3 on reducing the peak torque are both very small. Case 2 with a thicker EM shield shows better effects which are however still quite insufficient if a peak torque of about 3 p.u. is required.

From these results, using an EM shield does not effectively reduce the peak torque during a short circuit. A thinker EM shield may be more effective but a much thicker shield is not realistic due to space limitation.

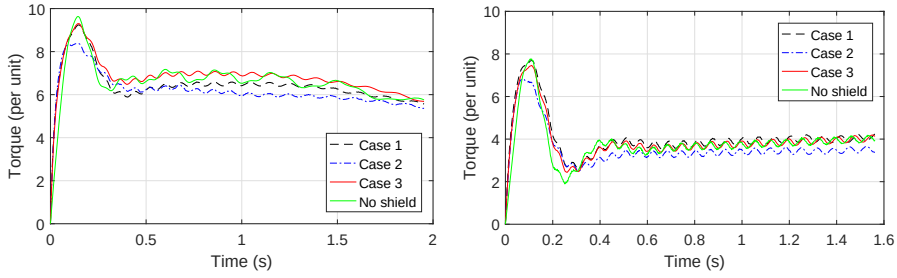

(a) Designs A (b) Designs B

Figure 5.3: Effects of EM shield on short circuit torque of Designs A and B during the short circuit for five electrical cycles of rated frequency in four cases.

5.5. ARMATURE SEGMENTATION

5.5.1. CHOSEN SCHEME OF ARMATURE SEGMENTATION

IN this chapter, the armature winding is segmented in such way that certain pole pairs belong to each segment and these pole pairs of one segment are evenly distributed along the generator circumference. The numbers of pole pairs of the four SCSG designs allow the number of segments to be 2 or 4. The segmentation way for the design D is sketched in Fig. 5.5 for 2 and 4 segments, for example. The pole pairs with S1 is connected to an individual converter and the pole pairs with S2 is connected to another individual converter, and so on.

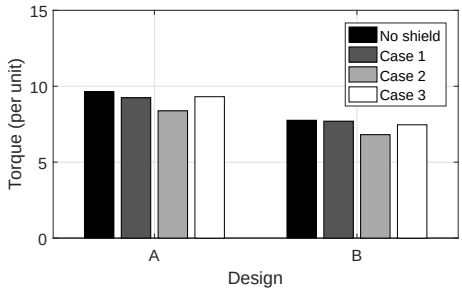

Figure 5.4: Effects of EM shield on peak torque of Designs A and B in four cases.

Evenly distributing the segments and their own pole pairs makes sure symmetry along the generator circumference. The purpose is to avoid significant unbalanced forces during a short circuit.

Short circuits at the armature winding terminals are usually caused by the failure of power electronic switches used in the converters. By dividing the armature winding into a few identical segments, the chance of a three-phase short circuit on the whole generator is greatly reduced. Since the probability of a three-phase short circuit in a non-segmented generator is small, the probability of three-phase short circuits occurring in all segments of a segmented generator at the same time is much smaller [33]. Thus, this chapter only examines the case when a three-phase short circuit only occurs to one of the armature winding segments, since the chance for it to happen is higher than the other cases.

5.5.2. FINITE ELEMENT MODELING OF ARMATURE SEGMENTATION

This chapter aims at assessing the feasibility of applying armature segmentation to reduce the short circuit torque. A 2D FE model is used to simulate the armature segmentation with two assumptions that simplify the problem.

ASSUMPTIONS

In this chapter, two assumptions are made for modeling the armature segmentation by FE methods:

• The armature winding has a single layer. This means that the overlapping of armature coils between adjacent segments is neglected in the slots.

• The end winding is neglected. This means that the overlapping of armature coils between different segments is neglected at the winding end.

These two assumptions result in independent armature segments and enable 2D transient FE modeling of short circuits. However, large practical power generators

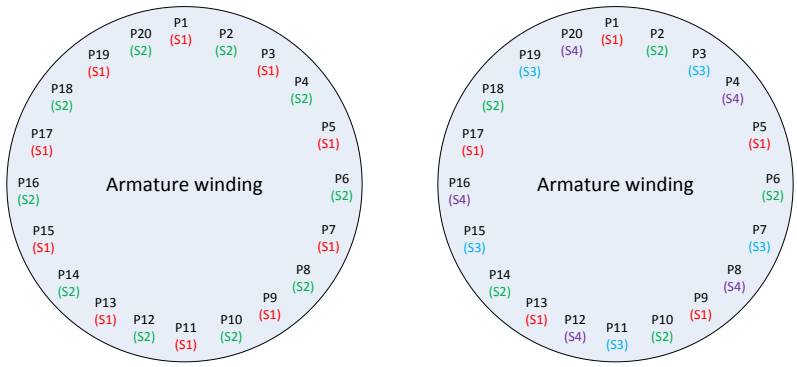

(a) 2 segments (b) 4 segments

Figure 5.5: Sketch of segmentation and pole pair distributions for Design D. P- pole pair numbering. S- armature winding segment numbering.

5

usually apply double-layer windings. In addition, armature coils at the end winding have overlapping. In future work, these practical issues should be taken into consideration in the model. This chapter is just a starting point for studying the feasibility of armature segmentation for reducing the short circuit torque. If this study with these assumptions did not give effective reduction of the short circuit torque, it would not be needed to take further steps to assess this method. This is because dependent armature segments will introduce coupling of adjacent segments and weaken the reduction of short circuit torque.

MODELING

The FE model is illustrated in Fig. 5.6, using Design D with two armature segments as an example. The healthy segment and the faulted segment are adjacent. Since only one segment is faulted, the faulted segment is followed by a healthy segment as seen from the SC field winding. If the number of segment becomes four, the faulted segment will be followed by three healthy segments.

5.5.3. RESULTS

The FE short circuit model simulates five electrical cycles of the rated frequency. Figure 5.7 shows the current waveform of phase A of Design A, for instance, with and without armature segmentation. The peak currents remain in the same level in all the three cases. This result matches the rough estimation by $I_{peak} \propto (E_f / X_l)$, where E_f is the no-load voltage and X_l is the leakage reactance. When the number of armature segments is N_{seg}, the no-load voltage and leakage reactance of each

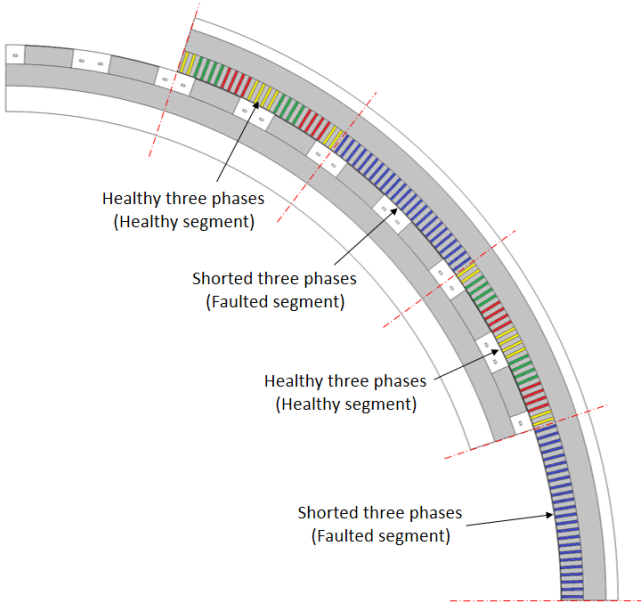

Figure 5.6: Modeling of armature segmentation in the FE model for short circuit simulation. Design D with two segments is shown as an example.

segment become E_f/N_{seg} and X_l/N_{seg}, respectively. Therefore, the peak current I_{peak} remains almost the same. The change of frequency is due to the decrease of rotational speed caused by the short-circuit torque.

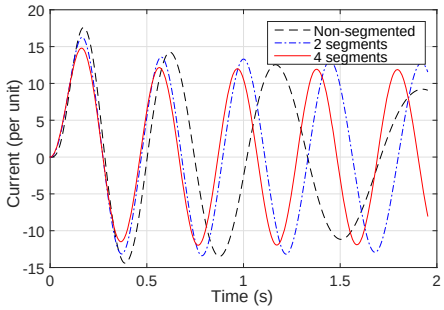

Figure 5.7: Current of phase A of Design A with $N_{seg} = 1$, 2 and 4.

The electromagnetic torque T_e of the four SCSG designs are calculated in the

cases of non-segmented, 2-segments and 4-segments armature windings. The torque during the short circuit in each case is shown in Fig. 5.8. The torque during the whole short circuit process can effectively be suppressed by armature winding segmentation. In the cases with armature winding segmentation, the short circuit torque has large ripples. This is a result of the field winding which is not segmented. p/N_{seg} of the field winding has to pass once the shorted segment every electrical cycle and all field poles pass healthy and shorted segments alternately, where N_{seg} is the number of segments. As a result, large ripples are induced in the field current, which then produce torque ripples.

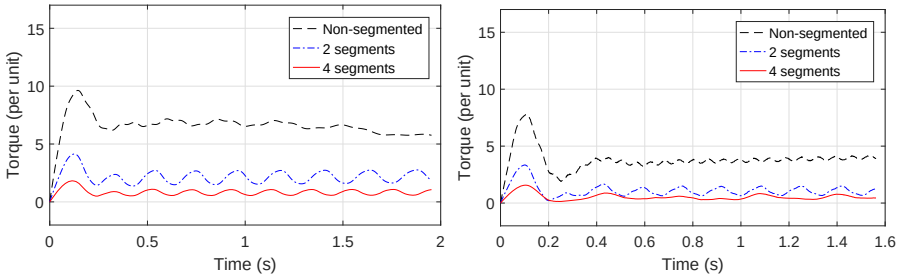

(a) Designs A (b) Designs B

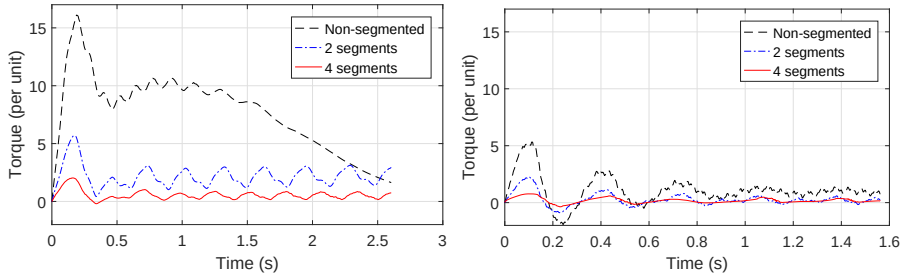

(c) Designs C (d) Designs D

Figure 5.8: Effects of armature segmentation on short circuit torque of Designs A, B, C and D during the short circuit for five electrical cycles of rated frequency.

The peak torque is compared in Fig. 5.9. These results show that segmentation of the armature winding effectively reduces the short-circuit torque. If the number of segments is N_{seg}, the peak torque of the segmented SCSG is even a bit lower than $1/N_{seg}$ the peak torque of the non-segmented SCSG. Like the peak current, these results of peak torque match the rough estimation by $T_{e,peak} \propto (E_f^2/X_l)$. Normally, the

mechanical constructions for a wind turbine drive train are designed to withstand 3 times the rated torque. As the results show, dividing the armature winding into 4 segments can meet this requirement. With 2 segments, the peak torque is still too high.

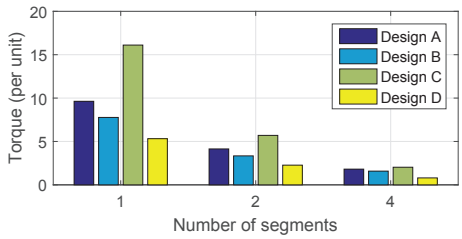

Figure 5.9: Effects of armature segmentation on peak torque of Designs A, B, C and D with N_{seg} = 1, 2 and 4.

Designs B and D with iron armature teeth show lower peak torques than Designs A and C with non-magnetic teeth. Because of no damper winding, the peak torque is only determined by the armature leakage inductance. Design C has a small leakage inductance in the armature winding because the salient pole and the short armature teeth together reduce the slot leakage flux. In Designs B and D, the saturated iron teeth result in more slot leakage flux and their peak torques are therefore lower.

The speed change of the generator during the short circuit is shown in Fig. 5.10. The speed is governed by Eq. (5.7) and determined by the electromagnetic torque T_e. With no segmentation, the speed decreases fast in Designs A and C. With segmentation, the speed decreases become much smaller. Using 4 segments results in a very gentle deceleration.

5.6. CONCLUSION

Excessively high short circuit torques could be suppressed in a few ways for SCSGs. This chapter assessed two approaches. One was making use of the EM shield which is part of the cryostat. The other divided the armature winding into a few identical segments. Four 10 MW SCSG designs differing in topologies were examined: two for the approach of using EM shield while four for the approach of armature segmentation. 2D finite element models were built to simulate the short circuit. The results show that the peak torque was not effectively reduced by using an EM shield if considering reasonable positions and thicknesses of the EM shield. However, the peak torque can effectively be suppressed by armature segmentation if one segment encounters a three-phase short at the terminal. Four segments are

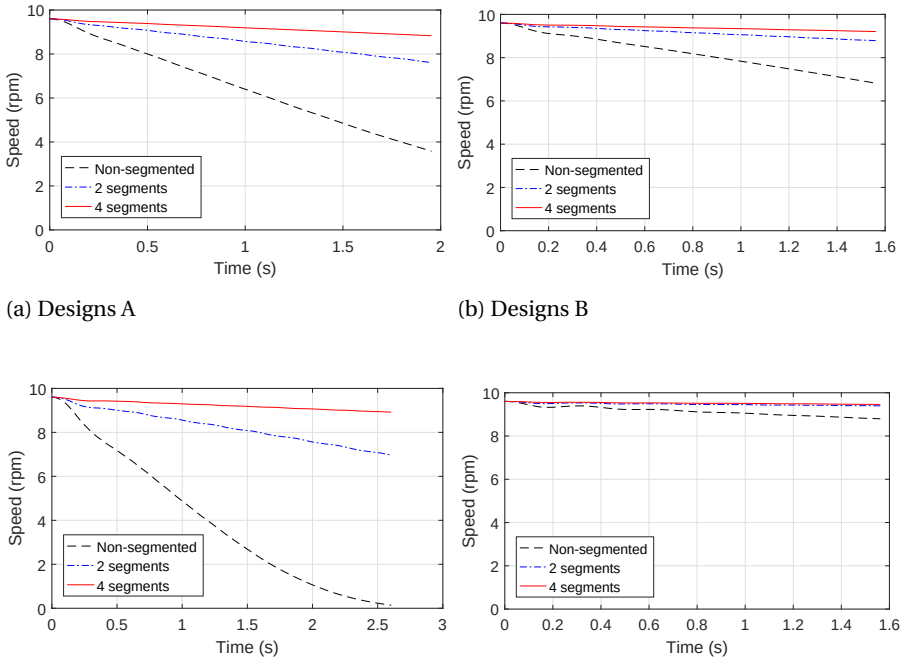

(a) Designs A

(b) Designs B

(c) Designs C

(d) Designs D

Figure 5.10: Speed change of Designs A, B, C and D during the short circuit for five electrical cycles of rated frequency.

more effective than two segments. More segments may be needed to meet the requirement of mechanical constructions of a wind turbine drive train, although additional costs due to multiple converters would be introduced.

In this chapter, we assumed that each armature segment is independent of the others by assuming a single-layer armature winding without the end winding. However, dependent segments with a double-layer armature winding with overlapping end windings are more often in practice. Dependent segments could weaken the effects of segmentation on reducing the short circuit torque. Dependent segments will be modeled and studied in the future work.

6

COMPARING SUPERCONDUCTING GENERATORS AND PERMANENT MAGNET GENERATORS

Part of the study in this chapter has been published in:
- D. Liu, H. Polinder, A. B. Abrahamsen, X. Wang and J. A. Ferreira, "Comparison of superconducting generators and permanent magnet generators for 10-MW direct-drive wind turbines," International Conference on Electrical Machines and Systems (ICEMS), Chiba, Japan, 2016.

6.1. INTRODUCTION

From Chapters 3, we found that the topology T12 with full iron cores and salient iron poles have lower capital CoEs and better overall performance. From Chapter 4, we found that iron teeth used in T12 do not produce unacceptable AC losses in the MgB_2 field winding. From Chapter 5, we found that the short circuit torque can effectively be suppressed by armature segmentation. Therefore, we can design a superconducting synchronous generator (SCSG) based on the topology T12 since T12 can now be considered most feasible for 10 MW direct-drive wind turbines. This design should be compared with a permanent magnet generator (PMSG) for evaluating its competitiveness.

At this moment, however, the technology readiness level of SCSGs for large wind turbines is so low that commercialization of such novel generators has not been realized yet. Comparing superconducting generators with technically mature PMSGs may not be fully fair, but it will be very interesting to compare their performance based on the same design and optimization method. Such comparisons are expected to provide feasibility insights for commercialization of SCSGs and to draw attention from the wind energy industry.

The objective of this chapter is to compare SCSGs and a PMSGs for 10 MW direct-drive wind turbines. Firstly we design an SCSG and a PMSG through the same design and optimization method for the minimum capital cost of energy (CoE) as developed in Chapter 3. Both the designed generators operate with the same wind turbine, wind condition and phasor diagram, and the optimization combines finite element (FE) and analytical models. Then this chapter compares the performance and important characteristics of the two generator designs with each other and another PMSG design available in the literature [131]. This PMSG design is compared as a reference since it employed a different design method established before. The quantities for comparison are: generator sizes, capital CoE of the wind turbine, annual energy production (AEP), and generator active material costs and masses.

6.2. GENERATOR DESIGN

6.2.1. GENERAL PARAMETERS

An SCSG and a PMSG are designed under the same conditions for the 10 MW reference direct-drive wind turbine used in previous chapters. The rated rotational speed is 9.6 rpm. The generator is directly connected to a back-to-back power electronic converter through a no-load line voltage of 3300 V. The generator parameters are listed in Table 6.1.

The diameter of the generator is not easy to decide. It is always a question whether to enlarge the diameter to around 10-m or to limit the diameter to a com-

Table 6.1: General characteristics of the 10 MW generator.

Parameter	Value
Nonimal torque	T_n = 10.6 MNm
No-load line voltage	3300 V
Air gap diameter	D_s = 6 m or 10 m
Armature winding type	Distributed
Rated RMS amature current density	J_s = 3 A/mm^2
Armature winding fill factor	k_{fil}=0.6

pact level (e.g. 6 m) for both the generator types. The diameter of 10 m or even larger has been extensively proposed for 10 MW direct-drive PMSGs [131, 142, 143] while a smaller diameter is considered to take more advantage of superconductivity for an SCSG.

This chapter considers both 6 m and 10 m as the air gap diameter of the SCSG and the PMSG. The diameter of 6 m may be too small for PMSGs, but it could indicate whether superconductivity is beneficial for reducing generator sizes and weights. Accordingly, the air gap length is set to 0.1% of the diameter, which is 6 mm for 6 m diameter and 10 mm for 10 m diameter.

The electrical loading of the armature winding is constrained below 75 kA/m to enable the use of forced air cooling for the stator. Direct cooling is costly and water cooling is complex for the wind turbine nacelle.

Two PMSG designs were proposed in [131] (for pitch control and active speed stall control, respectively) for a slightly different 10 MW wind turbine. The air gap diameter was 10 m. We select the pitch control design for the comparison in this chapter since most new wind turbines adopt pitch control nowadays. The generator design can be found in [131] in great detail.

6.2.2. OPERATION OF WIND TURBINE AND GENERATOR

The operation of the wind turbine and the phasor diagram for the generator operation have been introduced in Chapter 3. This chapter applies the same operations as described in Section 3.5.5.

6.2.3. SCSG

The SCSG design comes from the optimization results in Chapter 3 based on the unit cost and performance of currently available MgB_2 wires (the original case). The optimized topology T12 is chosen since it provide the best overall performance especially a lowest capital CoE. In Chapter 4, this SCSG design refers to as the IT de-

sign. In Chapter 5, this SCSG design refers to as the Design D. This SCSG design has an air gap diameter of 6 m. By using the same design and optimization method, we obtained the SCSG design with an air gap diameter of 10 m. One pole of the SCSG with the notation of optimization variables is sketched in Fig. 6.1.

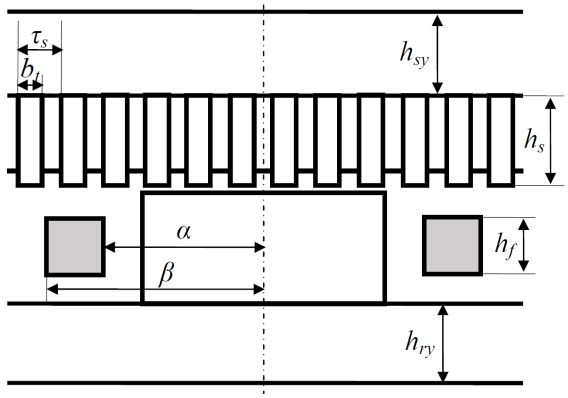

Figure 6.1: Sketch of one pole of an SCSG with the notations of the optimization variables. The gray blocks are the superconducting field coil accommodated in a modular cryostat. The space left around the field coil is fixed and occupied by the modular cryostat.

6.2.4. PMSG

The PMSG has surface-mounted permanent magnets on the rotor. The remanent magnetic flux density of the magnets is $B_r = 1.2$ T. The number of slots per pole per phase in the stator is set to $q = 2$ to allow for smaller pole pitches and achieve low losses in the magnets. One pole of the PMSG with the notation of optimization variables is sketched in Fig. 6.2.

The PMSG optimized in this chapter is referred to as PMSG-O and the referenced PMSG designed in [131] is referred to as PMSG-R. The PMSG-R design from [131] has an armature slot filling factor of 0.65 instead of 0.60. To constrain the electrical loading no higher than 75 kA/m and the armature tooth no narrower than 2 cm ($b_t \geq 20$ mm), we adjust the original design a bit: the slot height increases from 80 mm to 106 mm, and the ratio of armature tooth width to slot pitch increases from 0.50 to 0.61. The armature filling factor is changed to 0.60. Other design parameters remain the same. This adjustment makes sure that all the generator designs to be compared comply with the same conditions and constraints.

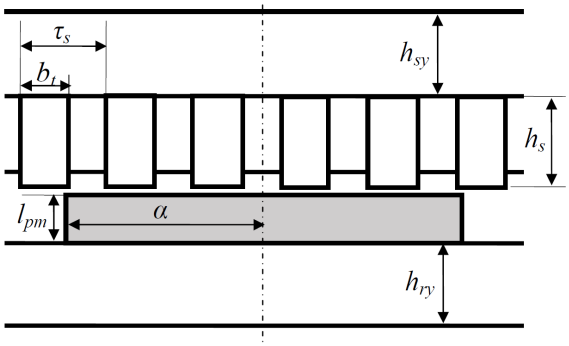

Figure 6.2: Sketch of one pole of a PMSG with the notations of the optimization variables. The gray block is the permanent magnet.

OPTIMIZATION

The optimization for the PMSGs is almost the same as that for the SCSGs except the following points:

- The objective function of the capital CoE now becomes

$$CoE = \frac{C_{CAPEX}}{a \cdot E_{AEP} \cdot T_{LT}} = \frac{C_{act}(X) + C_{str}(X) + C_{PE} + C_{other}}{a \cdot E_{AEP} \cdot T_{LT}} \tag{6.1}$$

where the cryogenic cooling power C_{cryo} has disappeared, and X is the set of optimization variables. For optimizing the SCSGs, the structural mass C_{str} is assumed to be a constant (as explained in Chapter 3). For optimizing the PMSGs, C_{str} is no more a constant but can be roughly estimated by scaling functions. The scaling function used in this chapter is based on the PhD thesis by Shrestha [27]. This PhD thesis developed scaling functions for structural mass as a function of the rated power and the aspect ratio of PMSGs. Since the 10 MW PMSG design in [131] is used as the reference for the scaling function, only the aspect ratio is taken into account in the scaling. In this chapter, the single bearing concept is chosen for the PMSG. The mechanical structure of this concept consists of beams and cylinders in the rotor and stator. Since the cost of the structure is proportional to the mass of the structure, the mass in the original scaling function is now replaced by the cost.

The scaling function for the cost of beams is given by

$$\frac{C_{beam}}{C_{beam,ref}} = (\frac{k_{asp,ref}}{k_{asp}})^{\frac{1}{3}} \tag{6.2}$$

where C_{beam} and $C_{beam,ref}$ are the structural beam costs of the PMSG to be optimized and the reference PMSG, respectively, and k_{asp} and $k_{asp,ref}$ are the aspect

ratios of the PMSG to be optimized and the reference PMSG, respectively.

The scaling function for the cost of beams is given by

$$\frac{C_{cy}}{C_{cy,ref}} = (\frac{k_{asp,ref}}{k_{asp}})^0 = 1 \tag{6.3}$$

where C_{cy} and $C_{cy,ref}$ are the structural cylinder costs of the PMSG to be optimized and the reference PMSG, respectively.

In this PhD thesis, Shrestha also estimated the ratio of the beam mass to the cylinder mass for the single bearing concept for different generator power ratings. For 10 MW, this ratio is about 4.5. Therefore, the ratio of the beam cost to the cylinder cost is also about $C_{beam}/C_{cy} = 4.5$. As a result, the scaling function for the structural cost for a 10 MW PMSG can be given by

$$\frac{C_{str}}{C_{str,ref}} = 0.818(\frac{k_{asp,ref}}{k_{asp}})^{\frac{1}{3}} + 0.182 \tag{6.4}$$

where $C_{str,ref}$ is the structural cost of the reference PMSG. The reference PMSG-R has a structural cost of $c_{str,ref} = 780$ k€ and an aspect ratio of $k_{asp,ref} = 0.16$ [131].

In this chapter, we assume that the unit cost of permanent magnet (NdFeB) is 50 €/kg. The cost of components of the 10 MW reference wind turbine for calculating C_{other} is estimated in Table 6.2. The energy production is obtained through calculating the power losses in the PMSGs. Compared to SCSGs, PMSGs do not have the cryogenic cooling power P_{cryo} and the eddy current loss in the armature copper conductors $P_{Cus,eddy}$ (as given in Eq. (3.13)).

Table 6.2: Cost estimation for the 10 MW reference wind turbine with SCSGs and PMSGs.

Component	Estimated cost		
Generator type	SCSG	PMSG-O	PMSG-R
Wind turbine (exl. generator)	7,500 k€		
Balance of plant	17,000 k€		
Power electronics C_{PE}	800 k€		
Cryogenic system C_{cryo}	710 k€(6 m), 600 k€(10 m)	n/a	n/a
Generator structural material C_{str}	500 k€(6 m), 700 k€(10 m)	To be optimized	780 k€
Generator active material C_{act}	To be optimized	To be optimized	620 k€[†]

[†]The unit cost of permanent magnets is adapted from 25 €/kg to 50 €/kg.

Table 6.3: Optimization variables and their optimal values.

		SCSG		PMSG-O		PMSG-R†
	Air gap diameter D_s (m)	6	10	6	10	10
	Generator active length l_s (m)	2.56	1.15	4.67	1.53	1.74
x_1	Pole pair number p	20	38	74	94	160
x_2	Inner pole span angle α (electrical degree)	66	66	62	72	73
x_3	Outer pole span angle β (electrical degree)	74	72	n/a	n/a	n/a
x_4	Field coil height h_f or magnet length l_m (mm)	10	10	18	28	20
x_5	Armature slot height h_s (mm)	102	114	98	118	80
x_6	Armature yoke height h_{sy} (mm)	122	114	50	60	40
x_7	Field yoke height h_{ry} (mm)	118	108	26	38	40
x_8	Ratio of armature tooth width to slot pitch b_t/τ_s	0.65	0.65	0.58	0.65	0.61

†These variables are not from optimization but from the design parameters provided in [131]. The generator active length and the ratio of tooth width to slot pitch are adapted to the electrical loading of 75 kA/m.

6.3. COMPARISON

THe optimal values of the optimization variables are listed in Table 6.3. The benefit of using superconductors to reduce the generator size can be observed but is small for the same diameter. The SCSGs need thicker stator and rotor yokes to reduce the capital CoE while the PMSGs show a feature of smaller outer diameters. With the optimized geometry, the SCSGs use resulting field current densities in the MgB_2 wire of 175 A/mm^2 for both D_s = 6 m and 180 A/mm^2 for D_s = 10 m.

The optimal SCSG and PMSG-O have had their respective minimum capital CoEs and are compared in Fig. 6.3 with each other and with the PMSG-R design. The capital CoE of the PMSG-R design is calculated with the identical assumptions and conditions for the SCSG and PMSG-O designs. For the same generator diameter, the SCSGs have higher capital CoEs than the PMSGs. For the SCSGs and the PMSGs, respectively, the larger diameter reduces a bit the capital CoE.

The AEP, used to indicate the capacity factor (CF) of a wind turbine, is extracted from the capital CoE and compared in Fig. 6.4. All the generators have CFs over 0.5. For the diameter of 6 m, the SCSG and the PMSG-O have almost the same AEP. When the diameter increases to 10 m, both the PMSG-O and PMSG-R produce more energy than the SCSG.

The total generator material cost is compared in Fig. 6.5 which breaks down the total cost into the active material, structural material and cryostat costs. The PMSGs have almost the same generator cost for both the diameters. For the SCSG, the larger diameter slightly reduces the generator cost. Compared with the PMSGs, the SC-

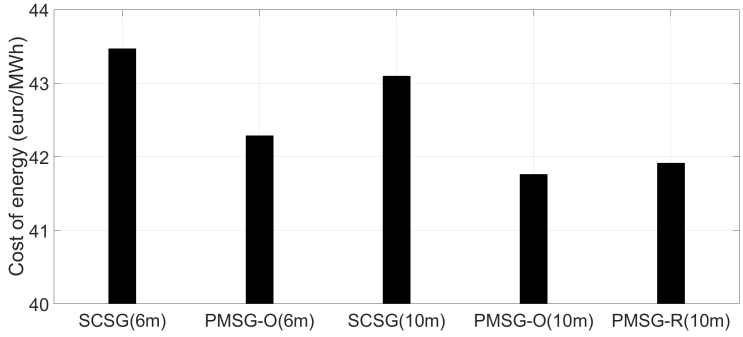

Figure 6.3: Capital CoE for SCSGs, PMSG-Os and PMSG-R.

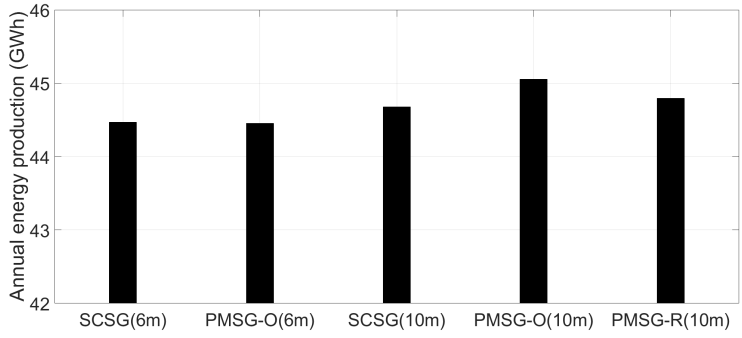

Figure 6.4: AEP for SCSGs, PMSG-Os and PMSG-R. The resulting capacity factors are 0.507, 0.507, 0.510, 0.514 and 0.511, respectively.

SGs have higher generator costs. The 10-m SCSG even has a higher generator cost than the 6-m PMSG. Further cost breakdown for the generator's active material cost shows the reason in Fig. 6.6. The SCSGs show their great advantage of reducing the active material cost as the required amount of permanent magnets for the PMSGs is rather costly. However, the cryostat used for the SCSGs significantly increases the total generator cost.

The generator's active material mass, resulting from the optimization merely for the capital CoE, is compared in Fig. 6.7. Due to the great amount of iron used to reduce the capital CoE, the SCSGs are rather heavy in this comparison, especially with the air gap diameter of 6 m. The SCSGs do not show effective mass reduction which should have benefited from using superconductors. Using lightweight core materials may help as discussed in Chapter 3. The PMSGs have small weights with

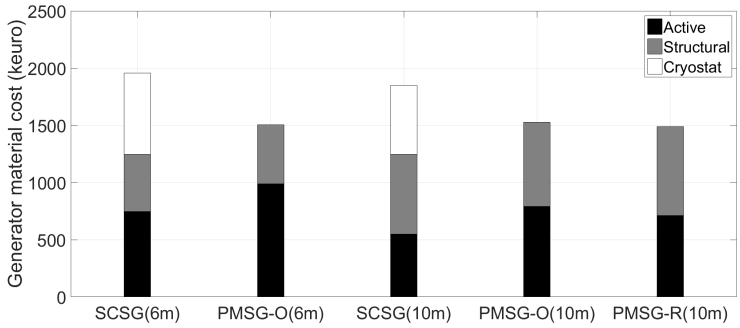

Figure 6.5: Generator material costs for SCSGs, PMSG-Os and PMSG-R.

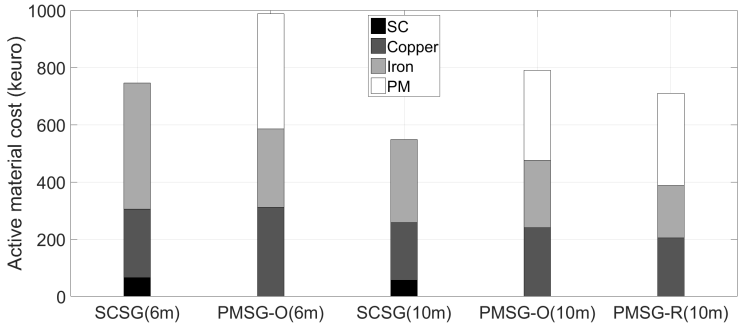

Figure 6.6: Active material costs for SCSGs, PMSG-Os and PMSG-R.

small pole pitches as expected.

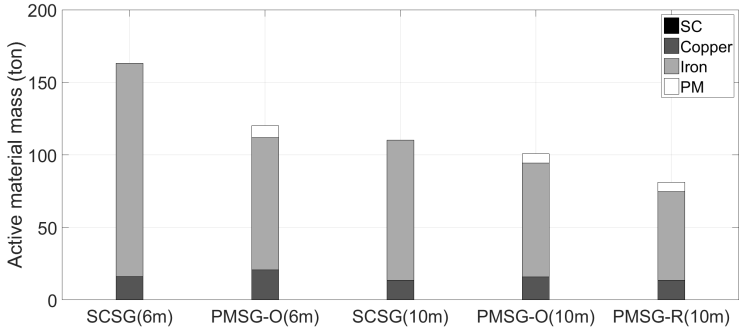

Figure 6.7: Active material masses for SCSGs, PMSG-Os and PMSG-R.

6.4. CONCLUSION

THis chapter aimed to compare novel SCSGs and conventionally employed PMSGs for 10 MW direct-drive wind turbines. The method of modeling the costs and losses have been presented with certain assumptions and constraints. Regarding the capital CoE and the total generator cost, the SCSGs are still more expensive than their PMSG counterparts. If installation, operation and maintenance costs and reliability issues related to (cooling) superconductors are taken into consideration, the SCSGs will become even more expensive. Furthermore, the SCSGs do not have the advantages of low weight over the PMSGs when the capital CoE is considered as the primary design objective. In summary, the SCSGs seem not competitive yet at the moment. It is needed to look for significant advantages which will make SCSGs sufficiently attractive in the wind energy industry.

7

POTENTIAL OF PARTIALLY SUPERCONDUCTING GENERATORS

Study in this chapter has been accepted by IEEE Transactions on Applied Superconductivity for publication:
- D. Liu, H. Polinder, A. B. Abrahamsen and J. A. Ferreira,"Potential of partially superconducting generators for large direct-drive wind turbines."

7.1. INTRODUCTION

THis chapter aims at assessing the potential of partially superconducting (SC) generators for 10 MW direct-drive wind turbines. Partially SC generators can be designed based on the properties of currently available SC materials, like what have been done in Chapter 3 and Chapter 6. However, the designs proposed in the literature have been facing various challenges, such as large amounts of costly SC materials [20, 122], low efficiencies [20, 23, 120–122], large diameters [23, 120] or large active material weights (Chapter 6 of this thesis and [23]). These designs partly or entirely use iron cores, which tend to increase the generator weight [20, 23, 120, 121]. Large air gap diameters with more poles can be adopted to reduce the weight [23, 120]. However, this approach increases the generator and nacelle sizes and challenges the mechanical construction [27]. To reduce the diameter, higher electrical loadings may be used but the results are higher copper losses and lower efficiencies [23, 120]. As concluded in Chapter 6, the partially SC generators are not competitive yet if the cost or cost of energy is chosen as the primary design objective. Other design objectives are therefore needed to show the advantages of SC generators.

A partially SC generator has a much wider range of field excitation than permanent magnet and copper-field-winding generators. Moreover, the superconductor technology is developing rapidly. Thus, it does not make sense to base SC generator designs only on the properties of currently available superconductors. It is therefore interesting to evaluate the potential performance of an SC generator by disregarding the superconductor type, eliminating the limitation of critical characteristics and increasing the current density capability of the superconductors. We can then find out the required superconductor types that meet the magnetic field level and required current density for achieving certain high generator performance.

The objective of this chapter is to find the potential of partially SC generators. Such generators can only be attractive if they have significant advantages over permanent magnet synchronous generators (PMSGs). Typically, a PMSG has shear stresses in the order of 53 kPa and efficiencies of 96%. Therefore, it is investigated what excitation is required to obtain a doubled shear stress of 106 kPa and an efficiency of 98%. Other generator characteristics, such as normal stress, stack length and active material mass, are also investigated to show the effects of increasing the excitation. Commercial superconductors, i.e. low- and high-temperature superconductors and MgB_2 superconductors are evaluated to meet the magnetic field and field current density resulted from the required excitation.

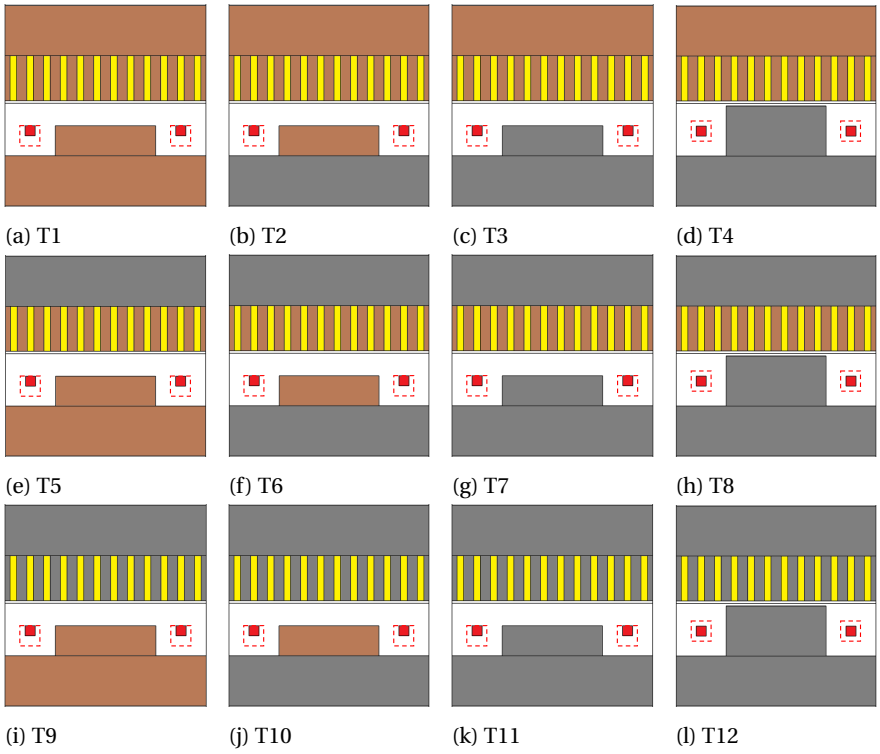

Figure 7.1: Twelve topologies to be compared. Red: SC field winding. Yellow: copper armature winding. Brown: non-magnetic core. Gray: iron core. The dashed boxes are the contours for a larger coil.

7.2. GENERATOR TO BE STUDIED

The partially SC generator for the study in this chapter is the same one as used in Chapter 3: a 10 MW direct-drive wind turbine with a rated speed of 9.6 rpm. The rated torque is therefore about 10 MN·m [11].

7.2.1. TWELVE TOPOLOGIES

The topologies to be studied in this chapter are the same as the twelve topologies studied in Chapter 3. The sketch of these topologies is repeated here in Fig. 7.1 with dashed red boxes indicating a larger coil area to be studied in this chapter.

7.2.2. DIMENSIONING

One pole of the SC generator is dimensioned as illustrated in Fig. 7.2. Then this single pole can be applied to different generator diameters. The size of the generator is then determined by the number of poles according to specific requirements.

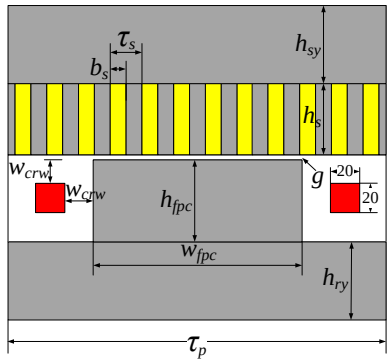

Figure 7.2: Sketch of dimensioning parameters of one pole.

The basic generator design and pole dimensioning are rough but generalized for all the topologies. The design parameters are set to achieve realistic designs although they may affect each topology a bit differently. Since the purpose of topology comparison is to show trends with the excitation currents and then no optimization is involved, the basic design which provides the same conditions is considered acceptable for performance comparison.

The pole pitch is set to $\tau_p = 0.4$ m and three reasons support this choice:

• According to the design proposals available in the literature, pole pitches between 0.379 m [20] and 0.660 m [23] are all possible.

• The comparison study in Chapter 3 for a low cost of energy has shown that the pole pitch lies between 0.4 m and 0.7 m for different topologies. The generator design resulting in the lowest cost has a small pole pitch about 0.4 m.

• The pole pitch should be larger than the minimum bending diameter of the superconductor which differs from type to type. It is thus not allowed to wind an SC field coil with a very small pole pitch.

The mechanical air gap length of the machine is $g = 10$ mm which is roughly around 0.1% of possible air gap diameters. In the rotor, the pole core width is assumed to be $w_{fpc} = 0.5\tau_p = 0.2$ m. The heights of the rotor back core and the stator yoke are thus equally set to $h_{ry} = h_{sy} = 0.5 w_{fpc} = 0.1$ m. The pole core height is $h_{fpc} = 60$ mm for topologies T1-T3, T5-T7 and T9-T11, and $h_{fpc} = 100$ mm for topologies T4, T8 and T12 (the difference of 40 mm is due to the extension of the

pole core). The cryostat wall thickness with thermal insulations occupies w_{crw} = 40 mm, which makes the effective air gap length of T1-T3, T5-T7 and T9-T11 become g_{eff}=$g + w_{crw}$ = 50 mm.

In the stator, the number of phases is $m = 3$. The number of slots per pole per phase is $q = 4$. The ratio of slot width to slot pitch is $b_s/\tau_s = 0.5$ (an equal fraction for a slot and a tooth). The slot height of $h_s = 84$ mm is determined for achieving an electrical loading of 75 kA/m for forced-air cooling [123], with the rated current density in the stator winding being $J_s = 3$ A/mm^2 (RMS value). The armature current density of $J_s = 3$ A/mm^2 is usually a starting point for designing a large electrical machine [144]. Many designs of SC generators for wind turbines in the literature have used this current density or slightly lower [20, 23, 120, 122]. However, the efficiency of these designs may not be high. A lower current density could be used to improve the efficiency. Therefore, this study will also investigate $J_s = 2$ A/mm^2 and compare it with $J_s = 3$ A/mm^2. Accordingly, the slot height is adjusted to $h_s = 126$ mm for $J_s = 2$ A/mm^2 to maintain the electrical loading of 75 kA/m.

The excitation or excitation current NI is calculated by the current density J_f multiplied by the cross-sectional area of the field coil A_f. In this paper, the cross-sectional dimension of one side of an SC field coil is fixed to 20 mm by 20 mm. As a result, the excitation is only determined by the current density applied in the SC field winding. However, only the excitation, which is equal to the area of $A_f = 400$ mm^2 multiplied by the current density J_f, takes effect for calculating the performance indicators and generator characteristics. Therefore, we do not need to know specifically either the current density or area until the feasibility of superconductors is evaluated, which will be presented in Section 7.6.

7.2.3. MODELING METHODS AND GENERATOR OPERATION

The performance indicators and generator characteristics are modeled and calculated regarding their relation with the excitation current for the twelve topologies. 2D finite element (FE) models have to be used to calculate the magnetic field because this study involves the linear low field region, the non-linear medium field region and the linear high field region of the B-H curve of iron (Fig. 3.7). Then these quantities are calculated with analytical equations.

For calculating all these quantities, the generator is operated in such a way that the armature magnetic field is perpendicular to the excitation field. In the d-q reference frame, this operation corresponds to the zero d-axis current control.

7.3. PERFORMANCE INDICATORS

The shear stress and efficiency (or total loss) are performance indicators for assessing a generator.

7.3.1. SHEAR STRESS

The shear stress σ_t is used for sizing an electrical machine by

$$T_e = \frac{\pi}{2}\sigma_t D_s^2 L_s, \tag{7.1}$$

where T_e is the electromagnetic torque, D_s is the air gap diameter, and L_s is the stack length. The shear stress needs to be calculated first of all. In 2D FE models, the shear force per unit length on one pole F_t is calculated with the Maxwell stress tensor by

$$F_t = \frac{1}{\mu_0}\int_{l_1=0}^{l_2=\tau_p} B_r B_t dl \tag{7.2}$$

where τ_p is the pole pitch, and B_r and B_t are the radial and tangential components of the air gap flux density.

The shear force F_t is an average value calculated from two stationary FE simulations. These two simulations differ in the relative position between the rotor and stator, and the phase angle of the armature current. From the first position to the second, the rotor rotates with an angle of $1/(4mq)$ of a mechanical cycle while the phase current shifts by a time of $1/(4m)$ of an electrical cycle. Choosing these two positions is under the assumption that the 6_{th} time harmonic of the magnetic field contributes to the force ripples most. Then, an electrical cycle has 6 cycles of force ripples. Compared with a complete transient simulation of the shear force, the error resulted from this averaging method is less than 3%. Since the aim of this study is just to find trends, this accuracy is acceptable. This method is the same as used in Section 3.5.4 in Chapter 3.

Then the shear stress σ_t is obtained by averaging F_t over the pole pitch τ_p:

$$\sigma_t = \frac{F_t}{\tau_p} \tag{7.3}$$

The effects of excitation currents on the shear stress of the twelve topologies are shown in Fig. 7.3. At low excitation, the shear stress increases fast when the excitation increases. Saturation starts to play a role with a higher excitation and the increase of shear stress becomes slow. Finally, the relative permeability of iron becomes $\mu_r \approx 1$ with a significantly high excitation, and the shear stress varies linearly.

The twelve topologies, in general, follow the trend: the shear stress becomes higher from T1 to T12. With a very high excitation, the shear stress of all the topologies finally becomes parallel with each other. This result implies that using iron cores can effectively increase the shear stress even though it is saturated.

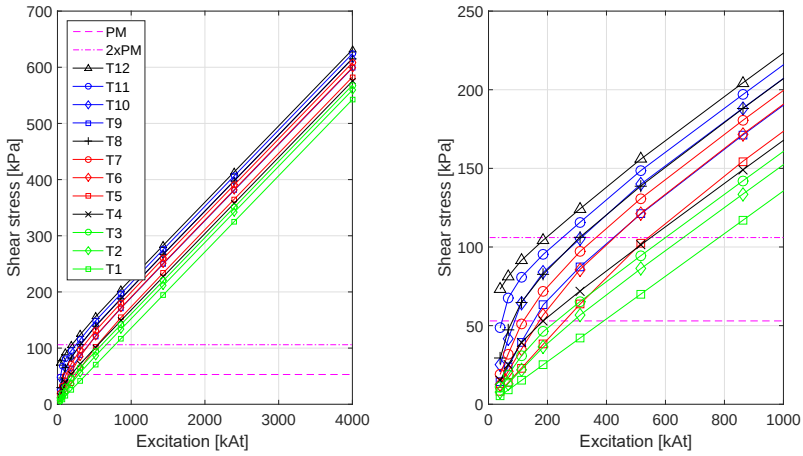

(a) Full range

(b) Zoom in (low excitation)

Figure 7.3: Shear stress with respect to excitation currents of the topologies T1-12. Dashed horizontal lines indicate the typical shear stress of a PMSG (lower) and twice the PMSG generator level (upper).

The typical shear stress of a PMSG generator is about 53 kPa which is also plotted in Fig. 7.3. This number is estimated by considering an air gap magnetic field of 1 T (amplitude) and an electrical loading of 75 kA/m (RMS). If we want to achieve a doubled shear stress, i.e. 106 kPa, as indicated in Fig. 7.3, the excitation must be sufficiently high. However, the difficulty in reaching 106 kPa is quite different for the twelve topologies. The topologies with more iron show higher shear stresses than the others. The topology T12 achieves 106 kPa much more easily than T1. For 106 kPa, T12 requires the excitation of 200 kAt while T1 requires 800 kAt. The other topologies lie in between.

7.3.2. EFFICIENCY AT RATED LOAD (SIMPLIFIED LOSS MODEL)

An efficiency is actually dependent on the torque, speed and machine size. However, calculation of efficiency can be simplified if armature copper Joule losses are dominant and other losses, such as iron losses and copper eddy current losses, are neglected. Such simplification can facilitate basic observation of how efficiency is related to the key variables.

The total loss primarily comes from the copper loss in the armature winding and the core loss in the iron, if the cooling power consumption is not taken into account. The copper loss consists of Joule losses and eddy current losses. For the purpose of making an efficiency independent of the power rating, the iron loss can

be assumed to be negligible due to the low frequency of the direct-drive generator. The copper eddy current loss can also be assumed to be negligible by assuming very fine stranding of copper filaments. Therefore, only the Joule loss is left in efficiency calculation. Then the efficiency η can be calculated by:

$$\eta = 1 - \frac{C \cdot J_s^2 (1 + \frac{L_{ew}}{L_s})}{\sigma_t v} \tag{7.4}$$

where L_{ew} is the length of one end of an armature winding turn, L_s is the stack length, J_s is the RMS current density in the armature winding, σ_t is the shear stress calculated from Eq. (7.3), and v is the relative linear speed between the generator rotor and stator. The constant C is defined as

$$C = \rho_{Cu} h_s k_{fil} (\frac{b_s}{\tau_s}) \tag{7.5}$$

where ρ_{Cu} is the resistivity of copper, k_{fil} is the fill factor of the armature slots, and h_s, b_s and τ_s have been defined in Section 7.2.2. From Eq. (7.4), it is clear that the efficiency can be increased by reducing the armature current density J_s or the ratio of end winding length to stack length L_{ew}/L_s, or by increasing the linear speed v.

The efficiencies at rated load with an armature current density of $J_s = 3$ A/mm^2 are plotted in Fig. 7.4, assuming the end winding length is much smaller than the stack length whereby the term L_{ew}/L_s is neglected in Eq. (7.4). The topologies T1 and T12 are shown as two extreme cases (fully non-magnetic compared with fully iron-cored with salient poles). In Fig. 7.4, T12 is much more efficient than T1 in the excitation region lower than e.g. 1000 kAt. With a higher excitation, the differences become small. This result matches the comparison of shear stress σ_t in Fig. 7.3 since T12 has much higher shear stresses than T1. This result also implies that using more iron cores can effectively increase the generator efficiency, especially when the excitation is limited.

7.3.3. LOSSES AT RATED LOAD (DETAILED LOSS MODEL)

For calculating all the losses, we use the rated torque of $T_e = 10$ MN·m and the rated angular speed of $n_N = 9.6$ rpm. Three air gap diameters $D_s = 6.11$ m, 10.19 m and 14.26 m are compared which cover the range of commonly applied diameters proposed in the literature. These diameters contain 48, 80 and 112 poles, respectively, as a result of the fixed pole pitch of $\tau_p = 0.4$ m defined in Section 7.2.2.

Three types of losses are usually considered and calculated in an electrical machine:

- Copper Joule loss (I^2R loss)
- Copper eddy current loss

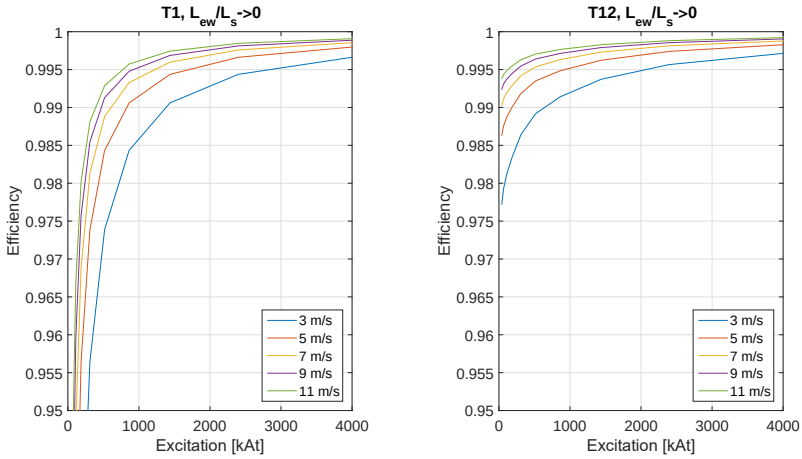

(a) T1 (b) T12

Figure 7.4: Efficiency of topologies T1 and T12 with $J_s = 3$ A/mm^2, when only armature copper Joule losses are considered and $L_{ew}/L_s \to 0$ is assumed in Eq. (7.4).

• Iron loss

In Section 7.3.2, the first loss has been calculated and the latter two losses were neglected, because the power rating and the generator size were both assumed unknown. In this section, we have set a rated power and three air gap diameters so we can then calculate all these three losses.

A few assumptions are made for calculating these losses:

• Iron will saturate when the excitation becomes high. Under heavy saturation, the hysteresis loop can be illustrated in Fig. 7.5. We may increase the excitation to such a high level that iron is fully saturated. Thus, the most important assumption for iron losses is that the relative permeability of iron becomes $\mu_r = 1$ after the magnetic flux density is over a particular value. Here we assume this value to be $B_{hys} = 2.5$ T. This assumption also implies that the area of the hysteresis loop reaches its maximum at $B_{hys} = 2.5$ T at point U (also point X). With a higher magnetic field, the area of the hysteresis loop will not expand anymore.

• The copper eddy current loss is calculated only in the stack length without the end winding. This allows for 2D analyses with an acceptable accuracy. For calculating the copper Joule loss, the end winding is included.

• The rotor iron is assumed to be loss free, so iron losses only occur in the stator iron cores.

• In the calculation of losses due to an alternating magnetic field, only the fun-

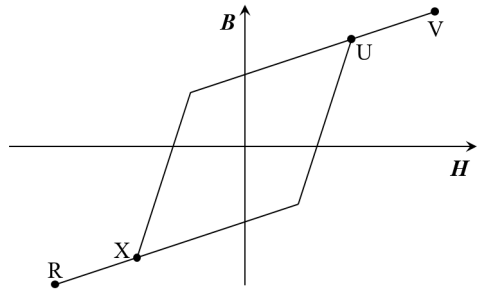

Figure 7.5: Hysteresis loop of iron with heavy saturation. The area of hysteresis loop become maximum and constant when the magnetic field is above B_{hys} at the point of U (also X). The relative permeability becomes $\mu_r = 1$ from U to V and from X to R.

damental components of the field are used.

COPPER LOSSES

The copper Joule loss $P_{Cu,joul}$ can easily be calculated. However, the calculation for the copper eddy current loss is a bit complicated since it is a function of the magnetic flux density and the fineness of stranding or transposing. Here only stranding is employed and modeled while the transposing is not. The copper eddy current loss can be expressed by [126]

$$P_{Cu,eddy} = \frac{1}{24\rho_{Cu}}\omega^2(a^2\hat{B}_r{}^2 + b^2\hat{B}_t{}^2)V_{Cu,s} \tag{7.6}$$

where ω is the angular electrical frequency, $\hat{B}_r$ and $\hat{B}_t$ are the radial and tangential components of the flux density (amplitude) in the copper conductor respectively, $V_{Cu,s}$ is the copper volume only in the stack length, and a and b are the height and width of a copper strand. We assume very fine strands for the copper conductors with $a = b = 1$ mm.

IRON LOSSES

The eddy current loss per unit iron mass is basically calculated by [127]

$$P_{Fe,eddy} = 2k_e(\frac{f}{50\text{ Hz}})^2[(\frac{\hat{B}_r}{1.5\text{ T}})^2 + (\frac{\hat{B}_t}{1.5\text{ T}})^2] \tag{7.7}$$

where $k_e = 0.5$ W/kg is the eddy current loss per unit iron mass with the field of 1.5 T and the frequency of 50 Hz, B_r and B_t are the radial and tangential components of the flux density (amplitude) in the iron core respectively. Equation (7.7) applies to both the stator iron teeth and the stator iron yoke.

The hysteresis loss per unit iron mass is calculated by

$$P_{Fe,hys} = 2k_h(\frac{f}{50\text{ Hz}})(\frac{B_{norm}}{1.5\text{ T}})^2 \tag{7.8}$$

where k_h = 2.0 W/kg is the hysteresis loss per unit iron mass with the field of 1.5 T and the frequency of 50 Hz, B_{norm} is the norm of the flux density (peak value) in the iron core. Equation (7.8) applies to both the stator iron teeth and the stator iron yoke.

The factor of 2 is included in Eqs. (7.7) and (7.8) because the flux density distribution contains harmonics, which increases the iron losses. In addition, manufacturing of steel laminates into a core increases the iron losses [127]. This factor is approximated to range from 1.6 to 2.0 according to [123].

The hysteresis loss per unit volume is the area of the hysteresis loop multiplied by the frequency. When the applied magnetic field exceeds the upper field of the maximum hysteresis loop (e.g. B_{hys}), the hysteresis loss per unit volume per electrical cycle will become constant as the area of the maximum hysteresis loop. This maximum loop implies that the hysteresis loss has an upper limit even if a higher magnetic field can be imposed on the iron.

This upper limit also leads to the fact that it is not convenient anymore to separate the field into two orthogonal components because it is hard to define the upper limit in either of the orthogonal components. By using the norm of the flux density, the upper limit can be assumed to be B_{hys} = 2.5 T, above which the hysteresis loss remains maximum and constant.

The total iron loss in the stator P_{Fes} is therefore given by

$$P_{Fes} = P_{Fe,eddy} + P_{Fe,hys} \tag{7.9}$$

TOTAL LOSS

The total loss P_{loss} is obtained by adding up the three losses:

$$P_{loss} = P_{Cu,joul} + P_{Cu,eddy} + P_{Fes} \tag{7.10}$$

The effects of excitation on the total loss are shown in Fig. 7.6 for two armature current densities and three air gap diameters. The dashed lines of 3% and 2% of the rated power of 10 MW are also plotted to indicate two reference loss levels for an SC generator. A loss of 2% plus a cryogenic cooling power of roughly 0.5% results in a higher efficiency (97.5%) compared to a PMSG (96%) [145].

Compared to the study on the efficiency in Section 7.3.2, the total loss here consists of not only copper Joule losses but also iron losses and copper eddy current losses. The latter two losses are functions of the frequency or the number of poles

and the amplitude of magnetic fields according to Eqs. (7.6)-(7.8). As a result, a larger air gap diameter, i.e. a larger linear speed v, does not definitely mean a lower total loss anymore. For the case of $D_s = 14.26$ m as shown in Fig. 7.6, the total loss turns reversely to go higher when the excitation reaches a very high level, e.g. 1000 kAt with $J_s = 2$ A/mm^2. This is mainly a result of a higher copper eddy current loss together with a higher iron loss due to such a high excitation and frequency. For the same diameter of $D_s = 14.26$ m, the total loss cannot even reach the 2%-loss level with $J_s = 3$ A/mm^2 no matter how far the excitation increases. Reducing the armature current density to $J_s = 2$ A/mm^2 makes it possible to achieve 2% but only in a small range of excitation. This result implies that reducing the armature current density apparently reduces the total loss while increasing the air gap diameter may not.

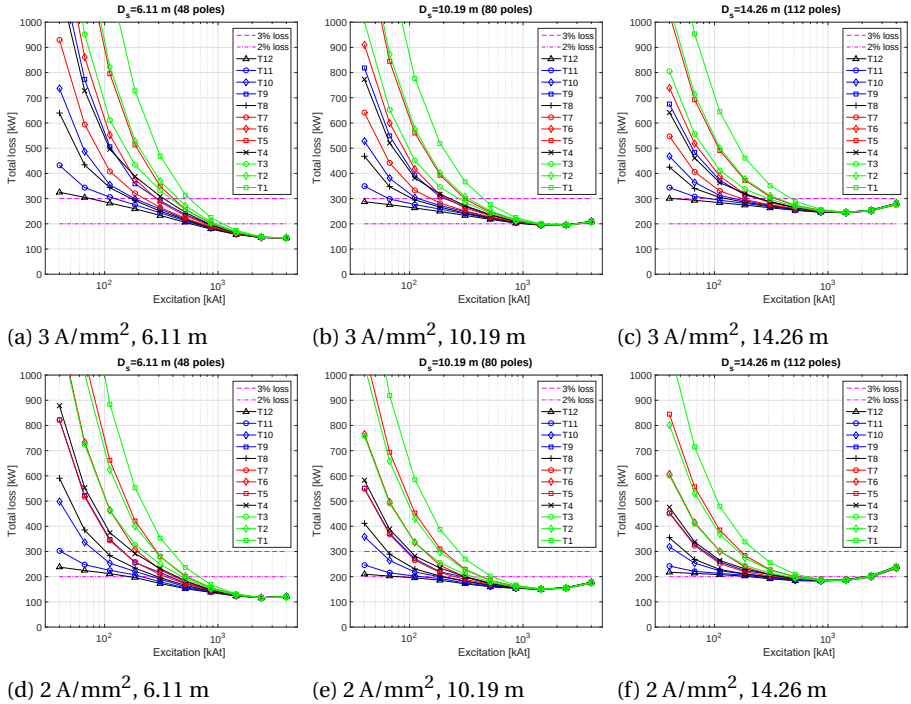

(a) 3 A/mm^2, 6.11 m (b) 3 A/mm^2, 10.19 m (c) 3 A/mm^2, 14.26 m

(d) 2 A/mm^2, 6.11 m (e) 2 A/mm^2, 10.19 m (f) 2 A/mm^2, 14.26 m

Figure 7.6: Total loss of topologies T1-T12 with respect to excitation currents for diameters of 6.11 m, 10.19 m and 14.26 m as well as current density of $J_s = 3$ A/mm^2 and $J_s = 2$ A/mm^2. The horizontal dashed lines indicate loss levels of 2% and 3%, respectively.

The topologies with more iron cores, e.g. T9-T12, reach the 2%-loss level more

easily than the topologies with more non-magnetic cores, e.g. T1-T4. The other topologies lie in between. At low excitation, e.g. below 200 kAt, the total loss of the topologies is considerably different. The topologies of T11 and T12, are much more efficient than the other topologies. However, the difference becomes much smaller when the excitation increases significantly, since heavy saturation makes the magnetic circuit similar for all the topologies and produces more iron losses in the topologies with iron stator cores.

7.4. GENERATOR CHARACTERISTICS

THe generator characteristics, such as normal stress, stack length and active material mass, are calculated to show the trend of increasing the excitation current. For calculating the normal stress, it is not needed to know the rated torque, rated speed and air gap diameter. For calculating the other generator characteristics, we use the rated torque of T_e = 10 MN·m and the rated angular speed of n_N = 9.6 rpm. Three air gap diameters D_s = 6.11 m, 10.19 m and 14.26 m are compared.

7.4.1. NORMAL STRESS

The normal stress σ_r indicates the attractive force between the rotor and stator and influences the structural mass which contributes to the total generator mass. Here we only estimate the normal stress at no load, because the armature load current contributes much less to the normal stress than the field current in a partially SC generator. For example, the fraction is only about 1% for the topology T12. This no load means that no force is produced by armature currents and the normal force is only produced between field currents and stator iron cores.

Firstly we calculate the resultant normal force on one pole F_r with the Maxwell stress tensor by

$$F_r = \frac{1}{2\mu_0} \int_{l_1=0}^{l_2=\tau_p} (B_r^2 - B_t^2) dl \tag{7.11}$$

Although not uniformly distributed over one pole, the normal stress σ_r can be calculated by averaging F_r over one pole:

$$\sigma_r = \frac{F_r}{\tau_p} \tag{7.12}$$

The average normal stress between the rotor and stator is plotted in Fig. 7.7 with respect to the excitation current, assuming an unchanged air gap length. As an example, the normal stress of a PMSG (200 kPa) is also indicated in both of the subfigures for comparison [27]. The topologies with iron stator teeth (T9-T12) have

higher normal stresses than the topologies with non-magnetic stator teeth (T5-T8). In the topologies with an ironless stator (T1-T4), the normal stress is $\sigma_r = 0$.

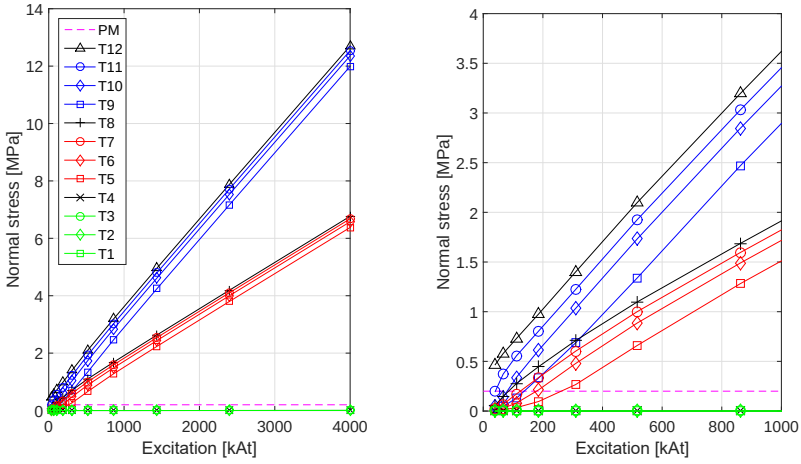

(a) Full range

(b) Low AT range

Figure 7.7: Average normal stress (attractive force density) per pole between the rotor and stator with respect to excitation currents. The horizontal dashes line indicates the typical level of a PMSG.

With a higher excitation, the normal stress becomes much greater in the topologies with iron stator teeth (T9-T12) or iron stator yoke (T5-T8). These normal stresses are much higher than those of a PMSG machine. As a result, the mechanical structure must be designed to support the rotor and stator under such high normal stresses. High normal stresses will thus be a significant challenge if a higher excitation has to be used for a high shear stress and a low total loss.

7.4.2. STACK LENGTH

The stack length L_s is calculated from the sizing equation Eq. (7.1):

$$L_s = \frac{2}{\pi} \frac{T_e}{\sigma_t D_s^2} \tag{7.13}$$

if we set the torque to $T_e = 10$ MN·m for a 10 MW direct-drive wind turbine. The results of stack length obtained with $J_s = 3$ A/mm^2 are shown in Fig. 7.8. In general, the stack length decreases when the excitation increases. The stack length of the topologies with more non-magnetic cores decreases very fast, whereas that of the topologies with more iron cores decreases slowly. However, the fact is that the

topologies with more iron cores already have much smaller stack lengths at low excitation.

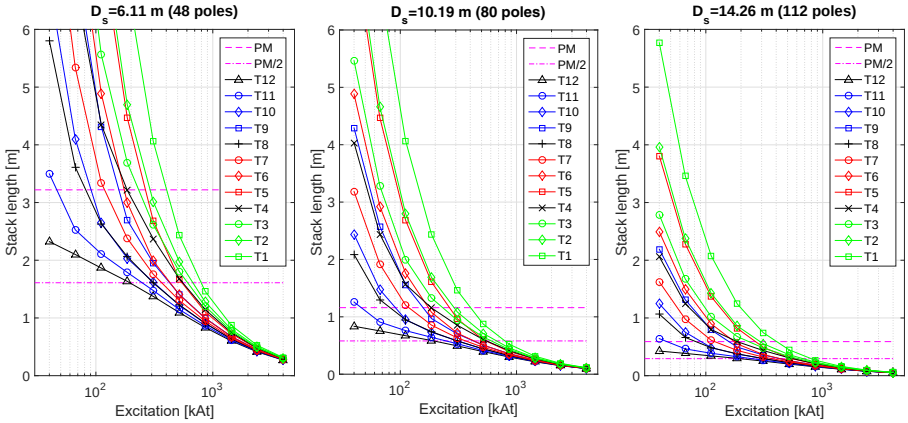

(a) 6.11 m (b) 10.19 m (c) 14.26 m

Figure 7.8: Stack length with respect to excitation currents for diameters of 6.11 m, 10.19 m and 14.26 m. Dashed horizontal lines indicate the typical stack length of a PMSG (upper) and half the PMSG level (lower).

The reference stack length of a 10 MN·m PMSG is also indicated by the dashed lines in this figure. This stack length is obtained by assuming a shear stress of 53 kPa. A half of this stack length is also shown for the shear stress of 106 kPa. This stack length will be achieved when the excitation is as high as 200 kAt for T12 and 800 kAt for T1 for both the diameters. The other topologies lie in between. The topologies with more iron require lower excitation currents.

If the excitation increases to about 4000 kAt, the difference of stack length for the topologies becomes minuscule. This vanishing difference is because the completely saturated iron behaves like a non-magnetic material, and then all the topologies have the same magnetic reluctance.

7.4.3. ACTIVE MATERIAL MASS

The active material mass consists of the core mass and the copper mass, neglecting the insignificant mass of the SC field winding. The iron mass density is 7650 kg/m^3 and the non-magnetic core material (i.e. glass fiber G10) has a mass density of 1850 kg/m^3. The copper mass density is 8900 kg/m^3.

The active material mass is not fully but nearly proportional to the stack length. It thus follows a trend similar to the stack length, as shown in Fig. 7.9. A larger

diameter reduces the active material mass, but it does not change the ranking of the compared twelve topologies. Also, with a high excitation, e.g. above 300 kAt, the difference between the active material mass of all the topologies becomes small.

With the same excitation in the region of low excitation (e.g. lower than 100 kAt), using iron cores can provide a lower active material mass. Using lightweight non-magnetic core materials, e.g. composites, is thus not the only choice to reduce the active material mass. For a higher excitation over 100 kAt, however, using either iron cores or non-magnetic cores with the same excitation does not make big differences.

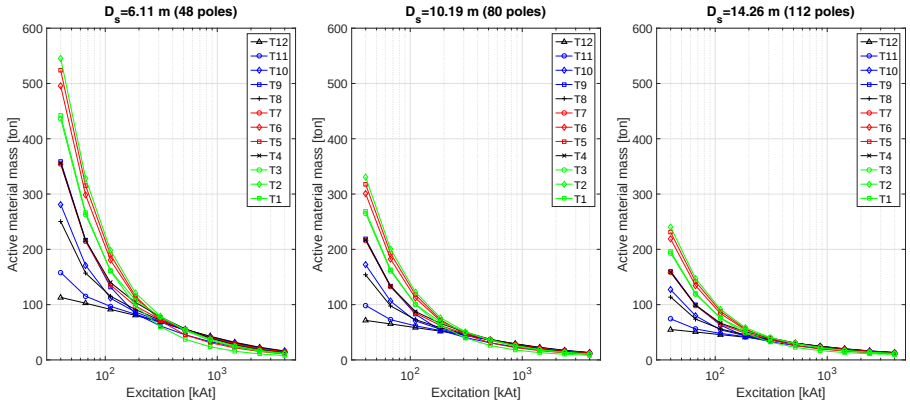

(a) 6.11 m (b) 10.19 m (c) 14.26 m

Figure 7.9: Active material mass with respect to excitation currents for diameters of 6.11 m, 10.19 m and 14.26 m, with $J_s = 3$ A/mm^2.

7

7.5. DISCUSSION ON DESIGN EXAMPLES IN LITERATURE

IN the literature, a few designs have been proposed for partially SC generators for 10 MW direct-drive wind turbines. Four available design examples which provide sufficient design details are summarized in Table 7.1. They use different excitation currents (Exci.), superconductor types (SC type), cryogenic temperatures (Temp.), armature current densities (J_s), shear stresses (σ_t) and air gap diameters (D_s), resulting in the different stack length (L_s), active material mass (M_{act}) and rated-load efficiency (only considering copper and iron losses in the generator). Each of these designs originates from one of the twelve topologies listed in Fig. 7.1 and their corresponding topologies are also indicated in Table 7.1. The fifth design is from this thesis. This design is the optimized topology T12 from Chapter 3, the IT design in Chapter 4, the Design D in Chapter 5 and the 6-m SCSG design in Chapter 6 (they

are the same design). This design is referred to Liu's design in this section.

• GE design employing NbTi at 4 K has already obtained a competitively small size (4.34 m diameter) and active material mass with a very high excitation of 928 kAt. The resulting shear stress is as high as 179 kPa. Its efficiency is only 96% and can not comply with the efficiency demand of 98%. It is also observed that no further efficiency increase can be obtained by increasing the excitation. However, the efficiency could be improved by, for example, enlarging the air gap diameter or reducing the armature current density.

• Abrahamsen's and Liu's designs both have small diameters of 6 m but the generators are both long due to relatively low shear stresses of 75 kPa. Abrahamsen's design is lightweight because of its non-magnetic cores, but it employs the topology T5 which results in a bulky and costly SC field winding [122]. On the contrary, Liu's design using the topology T12 has heavy active materials due to a large amount of iron, but it uses much less superconductors and then could have a lower active material cost. This large active material mass needs to be reduced by increasing the excitation.

• Tecnalia's and Xu's designs have higher shear stresses compared to Abrahamsen's and Liu's designs. Tecnalia's design based on the topology T8 also uses a large air gap diameter (10.10 m) as well as a high electrical loading (120 kA/m) to achieve its axial length (0.74 m) and active material mass (118 tons). Xu's design also based on the topology T12 uses an even larger air gap diameter (13.40 m) as well as a high electrical loading (120 kA/m) to achieve a lightweight generator design (49 tons). However, these two designs both have efficiencies below 97% and their high electrical loadings increase the complexity of cooling the armature winding.

None of the five designs in Table 7.1 provide an efficiency of over 98% (or the 2%-loss level) without considering the cryogenic cooling power. Reducing the armature current density or increasing the air gap diameter together with a much higher excitation current can be considered to address this challenge.

7.6. FEASIBILITY OF COMMERCIAL SUPERCONDUCTORS

Not all SC wires can achieve the high excitation for a shear stress of 106 kPa and a 2%-loss level, because the current density is limited by the critical engineering current density J_e as shown in Fig. 7.10 for different SC wires. When evaluating the superconductors, we need to know the magnetic flux density B which the superconductors are exposed to. The magnetic flux density is produced by the excitation of SC field windings.

The four topologies (T5, T8, T9 and T12) of the five design examples shown in Table 7.1 will be used to evaluate the feasibility of superconductors.

Table 7.1: Design examples of partially SC generators for 10 MW direct-drive wind turbines.

Design	Topology	SC type	Temp. (K)	Exci. (kAt)	J_s (A/mm^2)	σ_t (kPa)	τ_p (m)	D_s (m)	L_s (m)	M_{act} (ton)	Efficiency	Reference
Abrahamsen	T5	MgB_2	20	470	3.0	75	0.536	5.46	3.10	52	†96.7%	[122]
Tecnalia	T8	MgB_2	20	230	3.0	112	0.660	10.10	0.74	118	††96.2%	[23]
GE	T9	NbTi	4	928	†††2.5	179	0.379	4.34	1.88	††70	95.7%	[20]
Xu	T12	HTS	50	31	3.0	††††109	0.438	13.40	0.31	49	96.8%	[120]
Liu	T12	MgB_2	20	25	3.0	74	0.471	6.00	2.56	149	96.9%	This thesis

† Estimated with the copper Joule loss of 2.3% given in [122], considering an additional copper eddy current loss of roughly 1%.

†† Estimated with the parameters provided in [20].

††† Estimated with the overall efficiency of 95.2% provided in [23], plus assumed 1% for cryogenic cooling and auxiliary components.

†††† Estimated with the generator size and torque provided in [120].

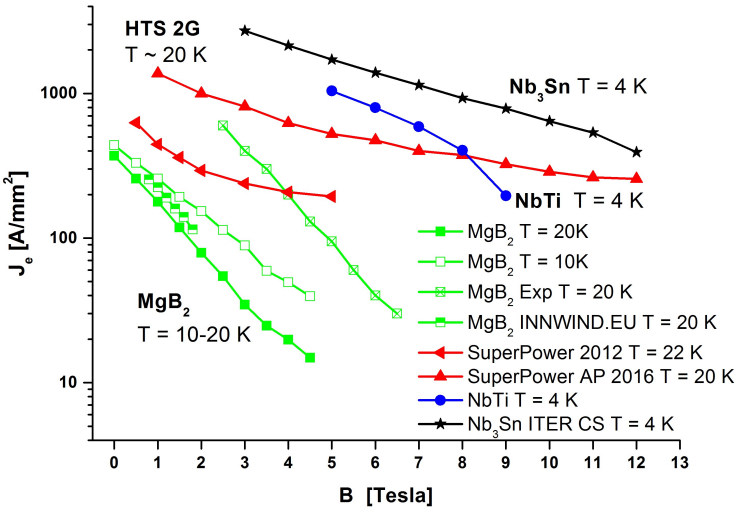

Figure 7.10: Critical engineering current density J_e of commercial superconducting wires. References: NbTi from [20], Nb_3Sn from [146], MgB_2 from [147], HTS 2G SuperPower 2012 from [148] and HTS 2G SuperPower 2016 from [149]. The base MgB_2 is the production wire in 2013. MgB_2 Exp is an experimental wire reported in 2013. MgB_2 INNWIND.EU is from the deliverable report for the INNWIND.EU project.

7.6.1. REQUIRED EXCITATION

By comparing Fig. 7.3 and Fig. 7.6, it is seen, that it is harder to reach the 2%-loss level than reaching the shear stress of 106 kPa for $J_s = 3$ A/mm^2. If the armature current density is reduced to $J_s = 2$ A/mm^2, the 2%-loss level will be fulfilled before the shear stress demand of 106 kPa is reached. Therefore, the criteria for selecting the required excitations are to achieve the 2%-loss level for $J_s = 3$ A/mm^2 and to achieve the shear stress of 106 kPa for $J_s = 2$ A/mm^2.

Table 7.2 shows the excitations required by the four topologies. Three air gap diameters (6.11 m, 10.19 m and 14.26 m) and two armature current densities (3 A/mm^2 and 2 A/mm^2) are investigated. The other parameters of the generator design are identical to those used in the studies of Sections 7.3 and 7.4 and have been described in Section 7.2.2. For $J_s = 3$ A/mm^2, the required excitations are obtained when the total loss equals 2%. As a result, the shear stresses with these excitations are much higher than 106 kPa. For $J_s = 2$ A/mm^2, the required excitations are obtained when the shear stress equals 106 kPa. As a result, the total losses with these excitations are a bit lower than 2%.

As shown in Fig. 7.6c, none of the four topologies can achieve the 2%-loss level for the air gap diameter of $D_s = 14.26$ m with $J_s = 3$ A/mm^2. For $J_s = 3$ A/mm^2 and

D_s = 6.11 m, T12 requires as high as 580 kAt and the other topologies require even higher. Reducing J_s = 3 A/mm^2 to J_s = 2 A/mm^2 makes the required excitations much lower as shown in Table 7.2. Then, the topology T12 requires only 200 kAt for the three diameters. With J_s = 2 A/mm^2, the three diameters of 6.11 m, 10.19 m and 14.26 m have the same required excitation for the same topology. The diameters make no difference of the require excitation so it is not needed to select a specific diameter for this evaluation of superconductors.

Also note that the required excitations listed in Table 7.2 are obtained from the design dimensioned in Section 7.2.2 for a pole pitch of τ_p = 0.4 m. This design was not optimized. Thus, the numbers of required excitations listed in Table 7.2 may not apply to other designs but are used as reference numbers.

Table 7.2: Required excitation (kAt) for different topologies to achieve the shear stress of 106 kPa and the 2%-loss level

J_s	†3 A/mm^2			††2 A/mm^2		
D_s (m)	6.11	10.19	14.26	6.11	10.19	14.26
T5	910	1370	n/a	550	550	550
T8	680	1250	n/a	310	310	310
T9	820	1280	n/a	450	450	450
T12	580	1050	n/a	200	200	210

†The loss level is just equal to 2% while σ_t is higher than 106 kPa.

††σ_t is just equal to 106 kPa while the loss level is lower than 2%.

7

7.6.2. RESULTING MAGNETIC FIELDS

The maximum magnetic flux density in the SC coil winding produced by the required excitation is calculated in 2D FE models. These fields depend on the cross-sectional area of the field coil. Thus, we set two realistic areas for this evaluation: 20×20 mm^2 and 40×40 mm^2. The contour of the larger field coil is sketched by the dashed boxes in Fig. 7.1. Figure 7.11 shows the maximum flux density perpendicular to the SC wires B_{mp} and the maximum norm flux density in the SC wires $|B_m|$ as a function of excitation currents (with no armature current). The perpendicular field B_{mp} is used for evaluating the SC wires which are tapes, such as HTS and MgB_2. The norm field $|B_m|$ is used for evaluating the round SC wires such as NbTi and Nb_3Sn. By looking up the required excitations in Table 7.2 and the field-excitation relations in Fig. 7.11, the values of B_{mp} and $|B_m|$ for the four topologies are identified and given in Table 7.3 and Table 7.4. These two tables show sixteen cases (C1a, C1b ...C8a, C8b) of combining the maximum field and current density in the SC field coil.

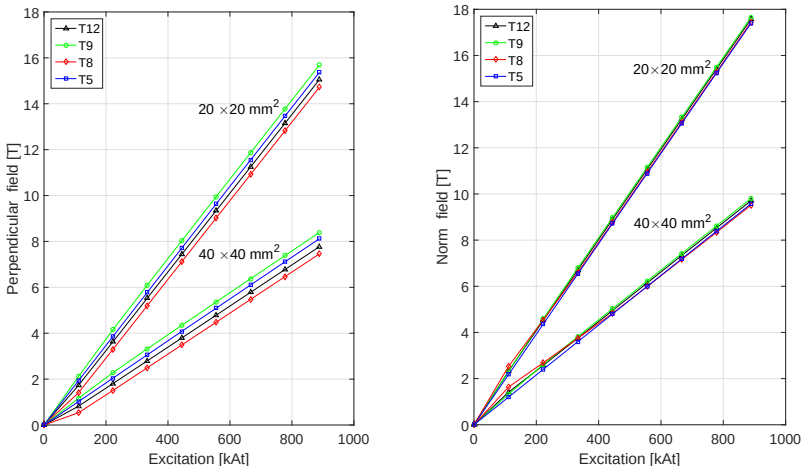

(a) Perpendicular component (b) parallel component

Figure 7.11: Maximum magnetic field at the surface of the SC field winding with respect to excitation currents for selected topologies.

The combination of $J_s = 3$ A/mm^2 and $D_s = 6.11$ m is a starting point. However, the maximum fields seem too high compared to Fig. 7.10 in most of the cases as indicated in Table 7.3. Thus, we could use $J_s = 2$ A/mm^2 instead to effectively lower the maximum fields as shown in Table 7.4. From this point of view, $J_s = 3$ A/mm^2 may not be a good option. The armature current densities of the design examples in Table 7.1 could be reduced for higher generator performance. In addition, a larger cross-sectional area of the field coil produces a lower maximum field in the field coil, as indicated in Fig. 7.11, Table 7.3 and Table 7.4.

7.6.3. REQUIRED FIELD CURRENT DENSITIES

The required current density in the SC field winding J_f is calculated by dividing the required excitation in Table 7.2 by the cross-sectional area of the field coil. The values of J_f are shown in Table 7.3 and Table 7.4 for the two cross-sectional areas of the field coil and for $J_s = 3$ A/mm^2 and $J_s = 2$ A/mm^2, respectively. The cross-sectional area of the SC field coil plays an important role in determining the current density. A larger area results in a lower current density and thus a looser requirement to the superconductor. However, a larger area means a higher cost of the SC field winding.

Table 7.3: Required surface magnetic flux density and current density for different topologies to achieve the 2%-loss level and a shear stress of over 106 kPa (J_s = 3 A/mm^2, D_s = 6.11 m)

	20×20 mm^2			
Topology	Case	B_{mp} (T)	$\|B_m\|$ (T)	J_f (A/mm^2)
T5	C1a	15.7	17.8	2275
T8	C2a	11.1	13.3	1700
T9	C3a	14.5	16.3	2050
T12	C4a	9.8	11.6	1450
	40×40 mm^2			
Topology	Case	B_{mp} (T)	$\|B_m\|$ (T)	J_f (A/mm^2)
T5	C5a	8.3	9.8	569
T8	C6a	5.6	7.3	425
T9	C7a	7.8	9.1	513
T12	C8a	5.0	6.4	363

Table 7.4: Required surface magnetic flux density and current density for different topologies to achieve the shear stress of 106 kPa and a loss level lower than 2% (J_s = 2 A/mm^2)

	20×20 mm^2			
Topology	Case	B_{mp} (T)	$\|B_m\|$ (T)	J_f (A/mm^2)
T5	C1b	9.5	10.8	1375
T8	C2b	4.8	6.2	775
T9	C3b	8.1	9.1	1125
T12	C4b	3.2	4.1	500
	40×40 mm^2			
Topology	Case	B_{mp} (T)	$\|B_m\|$ (T)	J_f (A/mm^2)
T5	C5b	5.0	5.9	344
T8	C6b	2.3	3.5	194
T9	C7b	4.4	5.1	281
T12	C8b	1.6	2.3	125

7.6.4. FEASIBLE SUPERCONDUCTORS

To evaluate the feasibility of superconductors, we compare the sixteen cases with the critical engineering current density J_e of the superconductors in Fig. 7.10. Note that B_{mp} is used for HTS and MgB_2 while $|B_m|$ is used for LTS. The feasibility of these superconductors for the sixteen cases and the four topologies is summarized in Table 7.5.

Table 7.5: Feasibility of Different Superconducting Wires

Superconductor	Feasible case	Feasible topology
MgB_2 20 K	None	None
MgB_2 INNW. 20 K	None	None
MgB_2 10 K	C8b	T12
MgB_2 Exp 20 K	C6b, C8b	T8, T12
2G HTS-2012 22 K	C6b, C8b	T8, T12
2G HTS-2016 20 K	C8a, C4b, C5b C6b, C7b, C8b	T5, T8, T9, T12
NbTi 4 K	C8a, C4b, C5b C6b, C7b, C8b	T5, T8, T9, T12
Nb_3Sn 4 K	C6a, C7a, C8a, C2b, C4b, C5b, C6b, C7b, C8b	T5, T8 T9, T12

Compared with the other SC materials, the LTS, i.e. NbTi and Nb_3Sn, are more feasible to achieve the shear stress of 106 kPa and the 2%-loss level for a partially SC generator. All the four topologies can employ the LTS. However, LTS operates at 4.2 K and thus requires rigorous cooling. The HTS-2012 (SuperPower) is feasible for fewer cases than the LTS but the newly developed HTS-2016 (SuperPower) is comparable to the NbTi. However, they have to be cooled down to 20 K, although they have critical temperatures of $T_C = 93$ K. The MgB_2 reported in [147] is not yet feasible for any of the four topologies at 20 K but feasible for T12 at 10 K with the larger field coil of 40×40 mm^2. A much lower temperature, such as 4 K, could be an option but this will drastically reduce the advantage of MgB_2 intended for 10-20 K. The MgB_2 used in the INNWIND.EU project seems infeasible at 20 K either if a realistic safety margin of current density, e.g. 20%, is considered. The new lab-tested MgB_2 shows its potential at 20 K to be feasible for T8 and T12 with the field coil of 40×40 mm^2. However, this lab-tested MgB_2 is not commercially available yet.

7.7. CONCLUSION

THe attractive performance of a shear stress of 106 kPa and a 2%-loss level can be achieved in all the twelve topologies by significantly increasing the excitation. The topologies with more iron, especially the fully iron-cored topology with salient poles, reach this performance more easily than the other topologies. Four of the twelve topologies are particularly investigated and they require excitations ranging from 200 kAt to 550 kAt with the armature current density of 2 A/mm^2. A higher ar-

mature current density, e.g. 3 A/mm^2, may not be a good option since it significantly increases the required excitations and challenges the superconductors.

The four topologies with such high excitations have different maximum magnetic fields in the superconducting field coil and the superconducting wires carry different current densities. By examining the critical engineering current density of commercial superconducting wires, the LTS, i.e. NbTi and Nb_3Sn, are capable of many of these magnetic fields and current densities at 4 K and thus feasible for all the four topologies. Some of the topologies may need a larger cross-sectional area of the field coil. The HTS may need to be cooled down to a relatively low temperature, e.g. 20 K, to increase its current density capability. At 20 K, the HTS is feasible for fewer topologies than the LTS but the newly developed HTS is comparable to the NbTi. The currently available MgB_2 is not feasible yet for any of the four topologies at 20 K but only feasible for the fully iron-cored topologies with salient poles at 10 K. MgB_2 superconductors, which are proposed for temperatures of 10-20 K, need further development to carry sufficient current densities in high magnetic fields.

8

CONCLUSION

IN 2012, the INNWIND.EU project initiated this research to investigate superconducting generators for 10-20 MW direct-drive offshore wind turbines. Superconducting generators are expected to be compact and lightweight because of the high magnetic field produced by superconducting windings. This technology is facing a few key feasibility challenges, such as high costs of superconducting wires, AC losses in superconductors and high short circuit torque. If these challenges are not solved, the feasibility of superconducting generators will remain low. Moreover, superconducting generators must have significant advantages over the mature conventional generators to enable commercialization. Another interesting issue is that many different electromagnetic designs have been proposed for superconducting generators. Each of them has its own advantages and disadvantages. There has not been an agreement on how to make the most feasible electromagnetic design for superconducting generators.

8.1. SOLVED RESEARCH PROBLEM

This thesis aims at increasing the feasibility of superconducting generators for 10 MW wind turbines and identifying the most feasible generator designs. This research problem is solved by answering the five research questions.

QUESTION 1

The first research question is: *Which topologies result in the lowest cost of energy, based on currently available superconductors?*

To answer this question, this thesis starts with looking into a wide range of electromagnetic designs by comparing as many generator topologies in Chapter 3. The purpose is to find the most feasible topologies from this large design space. The levelized cost of energy (LCoE) is considered as the key performance indicator for evaluating the feasibility of a new wind turbine technology. Due to the fact that 10 MW wind turbines do not exist yet, however, the simplified form of LCoE: the levelized capital cost of energy (LCCoE) is chosen as the criterion for a first comparison of generator topologies. In this LCCoE model, only the capital costs are considered. Moreover, the capital cost of the other wind turbine components except the active material cost of the superconducting generator are assumed to be constants. These assumed costs are based on a 10 MW reference wind turbine provided in the INNWIND.EU project and the superconducting generator designs proposed in the literature. Partially superconducting generators are chosen since their feasibility regarding AC losses is much higher than fully superconducting generators. Magnisium diboride (MgB_2) superconducting wires are employed in the field winding. They are less expensive than high temperature superconductors (HTS) while they require less rigorous cooling than low temperature superconductors (LTS). Twelve most applicable radial-flux generator topologies are optimized for the minimum LCCoE and then compared. A program using the genetic algorithm is developed in Chapter 3 for this optimization task.

In this comparison, not only are the current unit cost and current density capability of the MgB_2 wire used, but three scenarios are also studied by assuming a lower unit cost (1/4) and a higher current density capability (4 times). Such scenarios are to take into account the influence of the development of the superconductor technology on the comparison results. The comparison shows that the generator topologies with more iron in the core result in a lower LCCoE than the topologies with more non-magnetic cores, based on the current MgB_2 wire. When the MgB_2 wire becomes cheaper or capable of higher current densities, however, the topologies with more non-magnetic cores will become close to the topologies with more iron in the core regarding the LCCoE. This result implies that using iron cores will always be an effective option to reduce LCCoE for both now and far future. Required magnetic loadings can be produced in these topologies by using a small amount of costly superconducting wires.

The needed length of superconducting wires in these iron-core based topologies is more feasible than that in the other topologies in terms of fabrication and winding technologies. At present, manufacturing and winding very long superconducting wires (e.g. hundreds of kilometers) without performance degradation are very difficult. Therefore, although it is intended to use more superconducting wires to increase the torque density of the generator, the costs and manufacturing technology still make shorter wires more attractive. However, generators using these

iron-core based topologies tend to be heavy and thus, lightweight generator designs may not be obtained. When superconducting wires become sufficiently cheap compared to the other active materials of the generator, more non-magnetic cores can be employed if both a low generator weight and a low LCCoE are desired.

QUESTION 2

The second research question is: *What are the levels of AC losses in the superconducting winding of different electromagnetic designs due to ripple magnetic fields? Are the AC losses acceptably small or not?*

From the comparison in Chapter 3, the fully iron-cored topology with salient iron poles is found to be most feasible regarding LCCoE at present. Its AC loss level is examined in Chapter 4 since its iron stator teeth may cause high AC losses in the MgB_2 superconducting field winding. This topology is also compared with the topology with non-magnetic teeth. The result shows that using iron stator teeth in this topology does not lead to excessive AC losses. Using large numbers of slots per pole per phase (e.g. 4 or 5) can further reduce the AC losses. Therefore, this topology is considered most feasible and chosen for further comparison with the mature technology of permanent magnet generators.

QUESTION 3

The third research question is: *How can the short circuit torque be effectively suppressed by electromagnetic design?*

In partially superconducting generators, the large magnetic air gap leads to excessive short circuit torque. Such high torque challenges the mechanical construction of the wind turbine drive train. It is considered that the short circuit torque of the generator should be sufficiently low to adapt to the mechanical construction. In Chapter 5, three approaches are investigated to reduce the short circuit torque to no higher than 3 times the rated torque. Using an electromagnetic shield or more iron in the core is not effective. Using segmented armature winding with multiple power electronic converters can be an effective option when four segments are used for a 10 MW generator and only one segment is shorted. This approach needs further investigation since the model used for the armature winding segmentation assumed independent segments which simplified the winding construction in the model. However, the result implies that armature winding segmentation is a possible way to effectively reduce the short circuit torque of a superconducting generator.

QUESTION 4

The fourth research question is: *How competitive is a superconducting generator compared with a permanent magnet generator?*

In Chapter 6, the LCCoE-optimal generator design based on the fully iron-cored topology with salient poles is compared with 10 MW permanent magnet generators. However, this superconducting generator design does not have significant advantages over permanent magnet generators regarding the LCCoE and the generator cost, size and weight.

QUESTION 5

The fifth research question is then: *What is the potential of a superconducting generator for large wind turbines? What are the design parameters and suitable superconductors required to achieve high generator performance?*

Since the LCCoE at present is not yet the performance indicator that makes superconducting generators competitive, high generator performance from other perspectives must be achieved instead. Such high generator performance should be so attractive to the wind energy industry that the resulting high generator costs and added complexities of cryogenic systems can be considered worthwhile. For this purpose, shear stress and efficiency are chosen as the evaluating performance indicators since they are expected to be the breakthroughs by applying superconducting generators.

In Chapter 7, it is shown that increasing the excitation of the field winding to a high level can achieve high shear stresses and rated-load efficiencies. As an example, it is investigated what excitation is needed to reach both a shear stress as twice as that of a typical permanent magnet generator and a rated-load efficiency of 98%. The twelve generator topologies are again compared. All the topologies can achieve this high performance with a low armature current density of 2 A/mm^2. The topologies with more iron in the core reach this performance more easily than the topologies with more non-magnetic cores. The fully iron-cored topology with salient iron poles is again most feasible. Besides, to achieve such high generator performance, the required high excitation leads to a high current density and a high magnetic field in the superconducting wire. By examining current commercial superconducting wires, LTS and HTS are more feasible than MgB_2 wires to withstand the required high current density and high magnetic field. Although MgB_2 wires can be considered for the fully iron-cored topology with salient iron poles, they still need further development to be capable of the higher magnetic fields in the other topologies. In contrast, LTS and HTS are suitable for more generator topologies. However, LTS require 4-Kelvin operation and HTS are quite expensive, which also limits their feasibility.

ANSWER TO THE RESEARCH PROBLEM

In summary, from the perspective of electromagnetic design, this thesis points out a direction to increase the feasibility of superconducting generators for large direct-

drive wind turbines:

• Aiming at a lower LCCoE, iron-core based generator topologies are more feasible than the other topologies and the used lengths of superconducting wires are shorter. The fully iron-cored topologies are most feasible and their AC loss level is acceptably low. If a low generator weight and a low LLCoE are both desired, however, the topologies with more non-magnetic cores will become competitive once the superconducting wire is much cheaper and capable of much higher current densities.

• Currently, the superconducting generators do not show significant advantages of LCCoE over permanent magnet generators. To make superconducting generators attractive to wind energy industry, the shear stress and efficiency of the generator should be much higher than those of permanent magnet generators. Such advantages may offset the disadvantages of high generator costs and complicated cryogenic cooling.

• To achieve competitive shear stresses and efficiencies, the excitation of the superconducting field winding should be increased to a high level. To realize such high excitation, LTS and HTS are more feasible than MgB_2 wires at present. In addition, iron-core based generator topologies are again more feasible than the other topologies to reach high shear stresses and efficiencies, especially the fully iron-cored topology with salient poles.

• Aiming at an acceptable short circuit torque, armature winding segmentation with multiple power electronic converters can be considered.

This direction may not be the only one. However, it takes into account the key feasibility issues at the moment from the electromagnetic design perspective. Prototypes can be built following this direction to demonstrate and prove this technology.

8.2. SCIENTIFIC CONTRIBUTIONS

This thesis has two scientific contributions. The first contribution is finding the superconducting generator topology having the lowest LLCoE. This finding provides a design guideline to reduce the LLCoE of superconducting generators for wind turbine applications. Unlike the conclusions in the other literature, however, this finding from this thesis is not only using the current cost and properties of the superconducting wire (i.e. MgB_2 in this thesis) but also based on a scenario study which looks for future trends. This finding will thus be valid for both now and long terms.

The other contribution is finding the generator design requirements to achieve an attractive shear stress and generator efficiency. These requirements include field excitation, generator topology, armature current density and superconductor type. These required design parameters form another design guideline for superconducting generators to compete with permanent magnet generators in direct-drive wind turbine applications.

8.3. RECOMMENDATION FOR FUTURE WORK

To evaluate a wind turbine technology, the most complete way is to use LCoE as the criterion. An LCoE contains all the effects of size, weight, efficiency, cost, reliability and availability of the generator and the correlations among them. In this thesis, only the superconducting generator's active material cost and the resulting capital cost are variable in the the LCoE model. The other costs of the wind turbine components are assumed to be constants. In fact, some costs are hardly influenced by the electromagnetic design while the other costs more or less depend on the electromagnetic design. As 10 MW wind turbines are emerging in the near future, these dependences will be found and the LCoE and LCCoE models need to become more accurate.

As concluded in this thesis, the generator topologies with more iron in the core shows the advantages of reducing the LCCoE and achieving high shear stresses and efficiencies. However, they may have large magnetic forces between the rotor and stator because of the iron core in the stator. Such large magnetic forces will challenge the generator's structural support to maintain the air gap. It is interesting to evaluate the effects of iron-based generator topologies on the magnetic force and the design of the generator structure. This effect combined with the effect of active material mass can then be used to improve the LCCoE model and the assumed constant structural cost will become dependent on the topology. The advantage of the iron-based topologies to have a lower LCCoE may then be reduced. Moreover, the large magnetic force may also reduce the advantage of iron-based topologies that have high shear stresses and efficiencies to compete permanent magnet generators. Therefore, structural models of a superconducting generator are needed as future work to improve the LCCoE model and the evaluation of the potential generator performance.

By increasing the performance of the superconducting wire, the difference between the LLCoE of the generator topologies with iron core and non-magnetic core becomes small, while weight differences become significant. We neglected the influence of weight in the LLCoE model. However, in situations where weight is important, e.g. floating wind turbines, more radical superconducting generator concepts may be interesting, including fully superconducting generators.

Effectively reducing the short circuit torque of a superconducting generator is always an interesting topic. Using armature winding segmentation shows its potential in this thesis as a starting point. In future work, this approach needs further development. For example, a model with fewer assumptions needs to be developed with the consideration of the winding segmentation construction. This model then needs experimental validation.

This thesis makes a step of contribution to increase the technology readiness

level of superconducting generators for large direct-drive wind turbines. Efforts are still going on to achieve a mature superconducting generator design that is compact, lightweight, efficient, reliable and affordable. As 8 MW wind turbines using conventional direct-drive permanent magnet generators or geared induction generators are available in the market, superconducting generators will face more challenges from these conventional generators at the 10 MW power level. It is therefore urgent now to prove the superconducting generator technology. Besides theoretical studies and magnet pole demonstrations in various ongoing projects, construction and testing of full-scale superconducting generators seem highly demanded at the moment. It is hoped that the design direction or guidelines concluded from this thesis can help such work.

However, it cannot be ignored that the limited security of supply of permanent magnet materials may change the prospect of permanent magnet generators. Therefore, superconducting generators will stay as an interesting alternative for future large wind turbines and keep developing.

ACKNOWLEDGEMENTS

When I decided to do Ph.D., I did not expect so many challenges and difficulties, both in the research work and in my private life. Great thanks to my parents first of all, who have supported me every microsecond from China. I would not have achieved so far without their love and encouragement. They always trusted me with no hesitation and gave me full confidence and courage to overtake the various difficulties in my Ph.D. research and private life. Confucius remarked, "While his parents are living, a son should not go far abroad; if he does, he should let them know where he goes." Unfortunately, I broke it. I came to the Netherlands and have stayed for more than six years. Sometimes I myself did not know where to go during the four years of my Ph.D.. Sometimes I was drowned in my research and sometimes I was lost in my private life. They did not complain but unreservedly gave me their love and pushed me forward to today to finish my Ph.D.. I hope that the success of obtaining my doctoral degree will give the greatest reward to my parents who have sacrificed so much to support my dreams and desires.

Next, I would like to thank my co-promotor and daily supervisor dr. Henk Polinder. He also supervised my master thesis. Then he offered me this precious Ph.D. position. During the four years of Ph.D., I learned a lot from Henk about research methodology, critical thinking and how to design an electrical machine. Although the amount might be only 1% of his expertise, these knowledge and experience are already sufficient for me to start my career as an electrical machine and power conversion engineer. Henk was also concerned about my life and helped me ease my negative emotions from time to time. It was my luck to have Henk as my daily supervisor.

I would also like to thank dr. Asger B. Abrahamsen who is my second co-promotor. During my whole Ph.D. period, Asger was my project partner and we closely cooperated in the INNWIND.EU project. I learned a lot from Asger about superconducting materials and generators. In the last year of my Ph.D. when I was trying hard to publish journal papers, Asger provided many advices and suggestions and helped me a lot. One time he helped me revise a paper till midnight. It was my pleasure to have such a kind project partner and supervisor.

Thanks to my promotor prof. dr. Jan A. Ferreira. Although he was rather busy with his presidency in the IEEE Power Electronics Society in recent years, he still spent a few hours per month to evaluate the progress of my Ph.D. work and provide

his feedback. He could not supervise all the students at the same time but I could tell that he was trying to do his best. He was very patient on me when my progress was disappointing. I could not ask for more.

In these four years, I met many people around me. Some became my good friends. Some helped me a lot. I am afraid of forgetting to thank any of them. Xuezhou Wang was my Ph.D. colleague. Thanks to him for having lunch together, discussing machines, sharing life experiences, etc., almost everyday. Xiaowei Song was a Ph.D. student from Technical Univeristy of Denmark. We both worked on superconducting generators so we shared opinions while we also competed. Therefore, we grew up with each other. It is quite interesting that we have many other similarities, too. Are they due to coincidence or whatever reason? I do not know yet.

I am grateful for having had the Ph.D. colleagues and staff members of former EPP group and current DCE&S group, from Anoop Jassal to Tim Strous, from Tsegay Hailu to Jiayang Wu, from Sharmila Rattansingh to Harrie Olsthoorn.

I cherish very much my Chinese friends whom I have known since my master study in Delft. Those friends staying in the Netherlands made my life joyful. Thanks to Yating Ren, Fei Sun, Xinwei Sun, Zhuowei Liu, Long Kong, Fengli Wang, Fanhe Kong, Lu Zheng, Bo Fan, Qian Feng, Qing Shen, Ye Qiu. Those friends who have left the Netherlands left precious memories to me. Thanks to Shan Du, Ruoshi Wang, Haoyan Xue, Hejiang Chen, Xin Li.

In particular, thanks to Mrs. Ken Chao-Hsi and her Love Home. From her and the events at Love Home, I started to know more about Christianity and Christian culture. Every event at Love Home was full of love and fun and made me feel cured from anxiety and pressure.

Certainly, many thanks to XEMC Darwind B.V. for offering me my current job. I could not find another job that fit my interest and background so well in the Netherlands. Everyone of the company is so kind that I always feel happy nowadays. Special thanks to my colleagues Robert Rutteman and Michiel Damen for translating the summary of this thesis into Dutch.

Last but not least, I must thank the INNWIND.EU project. This project financially sponsored my Ph.D. study and research and provided an excellent platform to me to learn wind turbine technologies. It also provided many chances of presenting my work so my presentation skill was well trained. I will never forget those half-year meetings of the project held allover Europe, the insightful presentations in those meetings and the banquet at the foot of Acropolis of Athens. Here I would like to thank all the project partners involved in the INNWIND.EU project.

CURRICULUM VITÆ

Dong Liu was born in Lanzhou, Gansu, China on 22nd December 1984. He finished his high school education at High School Attached to Northwest Normal University, Lanzhou, China in 2003 and in the same year he went to Harbin Institute of Technology, Harbin, China for his bachelor education. In 2007, he graduated with Bachelor of Engineering and started his first job as a technical service engineer at Shenzhen NARI Technology Ltd., Shenzhen, China. In 2010, he started his master program at Delft University of Technology, Netherlands. In 2012, he received his Master of Science in Electrical Engineering.

Since December 2012 he has been working towards his Ph.D. degree at the Department of Electrical Sustainable Energy at Delft University of Technology, Netherlands. His Ph.D research results are compiled in this thesis. He is currently working as Electrical Machine & Power Conversion Engineer at XEMC Darwind B.V., Hilversum, Netherlands.

LIST OF PUBLICATIONS

JOURNAL ARTICLES

17. **D. Liu, H. Polinder, A. B. Abrahamsen and J. A. Ferreira**, *Potential of partially superconducting generators for large direct-drive wind turbines*, IEEE Transactions on Applied Superconductivity. (Accepted)

16. **D. Liu, H. Polinder, A. B. Abrahamsen and J. A. Ferreira**, *Topology comparison of superconducting generators for 10-MW direct-drive wind turbines: cost of energy based*, IEEE Transactions on Applied Superconductivity. **27**, 4 (2017)

15. **D. Liu, H. Polinder, A. B. Abrahamsen and J. A. Ferreira**, *Effects of armature winding segmentation with multiple converters on the short circuit torque of 10-MW superconducting wind turbine generators*, IEEE Transactions on Applied Superconductivity, **27**, 4 (2017).

14. **D. Liu, H .Polinder, A. B. Abrahamsen, E. Stehouwer, B. Hendriks and N. Magnusson**, *Optimization and comparison of superconducting generator topologies for a 10 MW wind turbine applications*, International Journal of Applied Electromagnetics and Mechanics. **53**, S2 (2017)

13. **D. Liu, H. Polinder, N. Magnusson, J. Schellevis and A. B. Abrahamsen**, *Ripple field AC losses in 10-MW wind turbine generators with a MgB_2 superconducting field winding*, IEEE Transactions on Applied Superconductivity, **26**, 3 (2016).

12. **X. Song, D. Liu, H. Polinder, N. Mijatovic, J. Holbøll and B. B. Jensen**, *Short circuits of a 10 MW high temperature superconducting wind turbine generator*, IEEE Transactions on Applied Superconductivity, **27**, 4 (2017).

11. **N. Magnusson, A. B. Abrahamsen, D. Liu, M. Runde and H. Polinder**, *Hysteresis losses in MgB_2 superconductors exposed to combinations of low AC and high DC magnetic fields and transport currents*, Physica C: Superconductivity and its Applications, **506** (2014).

CONFERENCE PUBLICATIONS

10. **D. Liu, H. Polinder, X. Wang and J. A. Ferreira**, *Evaluating the cost of energy of a 10 MW direct-drive wind turbine with superconducting generators*, 2016 XXII International Conference on Electrical Machines (ICEM), Lausanne, Switzerland, 2016, pp. 318-324.

9. **D. Liu, H. Polinder, A. B. Abrahamsen, X. Wang and J. A. Ferreira**, *Comparison of superconducting generators and permanent magnet generators for 10-MW direct-drive wind turbines*, 2016 19th International Conference on Electrical Machines and Systems (ICEMS), Chiba, Japan, 2016.

8. **D. Liu, H. Polinder, A. B. Abrahamsen and J. A. Ferreira**, *Comparison of 10 MW superconducting generator topologies for direct-drive wind turbines*, 2015 IEEE International Electric Machines & Drives Conference (IEMDC), Coeur d'Alene, USA, 2015, pp. 174-180.

7. **D. Liu, H. Polinder, A. B. Abrahamsen and J. A. Ferreira**, *Effects of an electromagnetic shield and armature teeth on the short-circuit performance of a direct drive superconducting generator for 10 MW wind turbines*, 2015 IEEE International Electric Machines & Drives Conference (IEMDC), Coeur d'Alene, USA, 2015, pp. 709-714.

6. **D. Liu, A. Jassal, H. Polinder and J. A. Ferreira**, *Validation of eddy current loss models for permanent magnet machines with fractional-slot concentrated windings*, 2013 IEEE International Electric Machines & Drives Conference (IEMDC), Chicago, USA, 2013, pp. 678-685.

5. **X. Wang, D. Liu, H. Polinder, D. Lahaye and J. A. Ferreira**, *Comparison of nested-loop rotors in brushless doubly-fed induction machines*, 2016 19th International Conference on Electrical Machines and Systems (ICEMS), Chiba, Japan, 2016.

4. **X. Wang, D. Liu, H. Polinder, D. Lahaye and J. A. Ferreira**, *Finite element analysis and experimental validation of eddy current losses in permanent magnet machines with fractional-slot concentrated windings*, 2016 19th International Conference on Electrical Machines and Systems (ICEMS), Chiba, Japan, 2016.

3. **A. B. Abrahamsen, N. Magnusson, D. Liu, E. Stehouwer, B. Hendriks and H. Polinder**, *Design study of a 10 MW MgB_2 superconductor direct drive wind turbine generator*, Proceedings of 2014 European Wind Energy Conference, Brussels, Belgium, 2014.

2. **A. B. Abrahamsen, N. Magnusson, B. B. Jensen, D. Liu and H. Polinder**, *Design of an MgB_2 race track coil for a wind generator pole demonstration*, Journal of Physics: Conference Series, **507**, 3 (2014).

1. **D. Kostopoulos, D. Liu, G. Genani and H. Polinder**, *Feasibility study of a 10 MW MgB_2 fully superconducting generator for offshore wind turbines*, Proceedings of EWEA Offshore 2013 conference, Frankfurt, Germany, 2013.

REFERENCES

[1] Z. Zhao, P. Wu, B. Xia, and M. Skitmore, *Development route of the wind power industry in China,* Renewable and Sustainable Energy Reviews **34**, 1 (2014).

[2] European Environment Agency, *Europe's onshore and offshore wind energy potential- an assessment of environmental and economic constraints,* EEA Technical report series: ISSN 1725-2237 (2009), 10.2800/11373.

[3] J. Kaldellis and M. Kapsali, *Shifting towards offshore wind energy—Recent activity and future development,* Energy Policy **53**, 136 (2012).

[4] M. Bilgili, A. Yasar, and E. Simsek, *Offshore wind power development in Europe and its comparison with onshore counterpart,* Renewable and Sustainable Energy Reviews **15**, 905 (2011).

[5] R. Texeira, *Multi-Terminal DC Networks System Integration, Dynamics and Control,* Ph.D. thesis, Delft University of Technology, CPI Koninklijke Wöhrmann (2014).

[6] AWS Truepower, `https://www.awstruepower.com/knowledge-center/maps/`, [Online], [Last accessed May 2017].

[7] EWEA, *The European offshore wind industry -key trends and statistics 2015,* `https://windeurope.org/wp-content/uploads/files/about-wind/statistics/EWEA-European-Offshore-Statistics-2015.pdf`, [Online], [Last accessed May 2017].

[8] Siemens, *Siemens 8.0 MW offshore wind turbine,* `http://www.siemens.com/content/dam/internet/siemens-com/global/market-specific-solutions/wind/brochures/siemens-wind-power-offshore-swt-8.0-154-productflyer-web-doublepages.pdf`, [Online], [Last accessed May 2017].

[9] MHI Vestas, `http://www.mhivestasoffshore.com/v164-8-0-mw-breaks-world-record-for-wind-energy-production/`, [Online], [Last accessed May 2017].

[10] F. Spinato, P. J. Tavner, G. J. W. V. Bussel, and E. Koutoulakos, *Reliability of wind turbine subassemblies,* IET Renewable Power Generation **3**, 387 (2009).

[11] INNWIND.EU, `http://www.innwind.eu/`, [Online], [Last accessed May 2017].

[12] K. Atallah and D. Howe, *A novel high-performance magnetic gear,* IEEE Transactions on Magnetics **37**, 2844 (2001).

[13] K. Atallah, J. Rens, S. Mezani, and D. Howe, *A novel "Pseudo" direct-drive brusheless permanent magnet machine,* IEEE Transactions on Magnetics **44**, 4349 (2008).

[14] H. Polinder, J. Ferreira, B. Jensen, A. Abrahamsen, K. Atallah, and R. McMahon, *Trends in wind turbine generator systems,* IEEE Journal of Emerging and Selected Topics in Power Electronics **1**, 174 (2013).

[15] A. B. Abrahamsen, N. Mijatovic, E. Seiler, T. Zirngibl, C. Træholt, P. B. Nørgård, N. F. Pedersen, N. H. Andersen, and J. Østergård, *Superconducting wind turbine generators,* Superconductor Science and Technology **23**, 034019 (2010).

[16] B. B. Jensen, N. Mijatovic, and A. B. Abrahamsen, *Development of superconducting wind turbine generators,* Journal of Renewable and Sustainable Energy **5**, 023137 (2013).

[17] S. S. Kalsi, B. B. Gamble, G. Snitchler, and S. O. Ige, *The status of HTS ship propulsion motor developments,* in *2006 IEEE Power Engineering Society General Meeting* (2006) pp. 5 pp.–.

[18] H. W. Neumüller and et al., *Advances in and prospects for development of high-temperature superconductor rotating machines at siemens,* Superconductor Science and Technology **19**, S114–S117 (2006).

[19] A. M. Campbell, *Superconducting and conventional machines,* Superconductor Science and Technology **27**, 124012 (2014).

[20] R. Fair, *Superconductivity for Large Scale Wind Turbines*, Tech. Rep. (DOE report DE-EE0005143, 2012).

[21] G. Snitchler, *Progress on high temperature superconductor propulsion motors and direct drive wind generators,* in *Power Electronics Conference (IPEC), 2010 International* (2010) pp. 5–10.

[22] AML, `http://amlsuperconductivity.com/applications/energy/doe-approved-wind-turbine-solution/`, [Online], [Last accessed May 2017].

[23] I. Marino, A. Pujana, G. Sarmiento, S. Sanz, J. M. Merino, M. Tropeano, J. Sun, and T. Canosa, *Lightweight MgB_2 superconducting 10 mw wind generator,* Superconductor Science and Technology **29**, 024005 (2016).

[24] O. Keysan and M. Mueller, *A modular and cost-effective superconducting generator design for offshore wind turbines,* Superconductor Science and Technology **28**, 034004 (2015).

[25] S. S. Kalsi, *Superconducting Wind Turbine Generator Employing MgB_2 Windings Both on Rotor and Stator,* IEEE Transactions on Applied Superconductivity **24**, 47 (2014).

[26] X. Song, N. Mijatovic, B. B. Jensen, and J. Holbøll, *Design study of fully superconducting wind turbine generators,* IEEE Transactions on Applied Superconductivity **25**, 1 (2015).

[27] G. Shrestha, *Structural Flexibility of Large Direct Drive Generators for Wind Turbines*, Ph.D. thesis, Delft University of Technology (2013).

[28] P. J. Masson, *Superconducting generators for large wind turbine: design tradeoff and challenges,* (presented at the 1st European Workshop SOWiT, 2011).

[29] R. Qu, Y. Liu, and J. Wang, *Review of superconducting generator topologies for direct-drive wind turbines,* IEEE Transactions on Applied Superconductivity **23**, 5201108 (2013).

[30] H. Karmaker, M. Ho, and D. Kulkarni, *Comparison between different design topologies for multi-megawatt direct drive wind generators using improved second generation high temperature superconductors,* IEEE Transactions on Applied Superconductivity **25**, 5201605 (2015).

[31] K. Sivasubramaniam, X. H. X. Huang, D. Ryan, K. Weeber, J. Bray, E. Laskaris, L. Tomaino, J. Fogarty, and S. Ashworth, *AC losses in a high temperature superconducting generator,* IEEE Transactions on Applied Superconductivity **15**, 2162 (2005).

[32] N. Magnusson, A. B. Abrahamsen, D. Liu, M. Runde, and H. Polinder, *Hysteresis losses in MgB_2 superconductors exposed to combinations of low AC and high DC magnetic fields and transport currents,* Physica C: Superconductivity and its Applications **506**, 133 (2014).

[33] Y. Liu, R. Qu, J. Wang, H. Fang, X. Zhang, and H. Chen, *Influences of generator parameters on fault current and torque in a large-scale superconducting wind generator,* IEEE Transactions on Applied Superconductivity **25**, 1 (2015).

[34] H. K. Onnes, *Disappearance of the electrical resistance of mercury at helium temperatures,* Electrician **67**, 657 (1911).

[35] R. de Bruyn Ouboter, *Superconductivity: Discoveries during the early years of low temperature research at leiden 1908-1914,* IEEE Transactions on Magnetics **23**, 355 (1987).

[36] CCAS, *Superconductivity: Present and Future Applications*, Tech. Rep. (Coalition for the Commercial Application of Superconductors (CCAS), 2014).

[37] A. P. Drozdov, M. I. Eremets, I. A. Troyan, V. Ksenofontov, and S. I. Shylin, *Conventional superconductivity at 203 kelvin at high pressures in the sulfur hydride system,* Nature **525**, 73 (2015).

[38] W. Meissner and R. Ochsenfeld, *Ein neuer effekt bei eintritt der supraleitfähigkeit,* Naturwissenschaften **21**, 787 (1933).

[39] S. Blundell, *Superconductivity, a very short introduction* (Oxford Univeristy Press, 2009).

[40] P. J. Lee, *Superconductivity and magnetism,* in *Engineering Superconductivity* (Wiley-IEEE Press, 2001) pp. 1–185.

[41] Y. Iwasa, *Case Studies in Superconducting Magnets, Second Edition* (Springer US, 2009).

[42] T. Berlincourt, *Type II superconductivity: Quest for understanding,* IEEE Transactions on Magnetics **23**, 403 (1987).

[43] R. G. Sharma, *Type II Superconductors,* in *Superconductivity: Basics and Applications to Magnets* (Springer International Publishing, Cham, 2015) pp. 49–69.

[44] M. R. Osorio, A. P. Morales, J. G. Rodrigo, H. Suderow, and S. Vieira, *Demonstration experiments for solid-state physics using a table-top mechanical Stirling refrigerator,* European Journal of Physics **33**, 757 (2012).

[45] M. Garber, M. Suenage, W. B. Sampson, and R. L. Sabatini, *Critical current studies on fine filamentary NbTi accelerator wires,* Advances in Cryogenic Engineering Materials SE-84 **32**, 707 (1986).

[46] N. high-magnetic-field lab, `https://nationalmaglab.org/images/magnet_development/asc/plots/JeChart041614-1022x741-pal.png/`, [Online], [Last accessed May 2017].

[47] M. P. Oomen, *AC loss in superconducting tapes and cables*, Ph.D. thesis, Delft University of Technology, Universiteit Twente (2000).

[48] P. Kováč, T. Melišek, and I. Hušek, *Ic anisotropy of in situ made MgB_2 tapes,* Superconductor Science and Technology **18**, L45 (2005).

[49] J. Durrell, *Critical Current Anisotropy in High Temperature Superconductors,* Ph.D. thesis, University of Cambridge (2001).

[50] B. ten Haken, J.-J. Rabbers, and H. H. ten Kate, *Magnetization and AC loss in a superconductor with an elliptical cross-section and arbitrary aspect ratio ,* Physica C: Superconductivity **377**, 156 (2002).

[51] STI, `http://www.suptech.com/about_superconducting_wire_n.php/`, [Online], [Last accessed May 2017].

[52] Aarnink, René and Overweg, Johan, *Magnetic resonance imaging, a success story for superconductivity,* Europhysics News **43**, 26 (2012).

[53] CERN, `https://home.cern/`, [Online], [Last accessed May 2017].

[54] ITER, `https://www.iter.org/`, [Online], [Last accessed May 2017].

[55] R. Zuijderduin, *Integration of High-T_c Superconducting Cables in the Dutch Power Grid of the Future,* Ph.D. thesis, Delft University of Technology, Delft University of Technology (2016).

[56] M. Noe and M. Steurer, *High-temperature superconductor fault current limiters: concepts, applications, and development status,* Superconductor Science and Technology **20**, R15 (2007).

[57] Columbus Superconductors, `http://www.columbussuperconductors.com/`, [Online], [Last accessed May 2017].

[58] J. C. H. Bone, *Influence of rotor diameter and length on the rating of induction motors,* Electric Power Applications, IEE Journal on **1**, 2 (1978).

[59] K. J. Binns and D. W. Shimmin, *The relationship between performance characteristics and size of permanent magnet motors,* in *1995 Seventh International Conference on Electrical Machines and Drives (Conf. Publ. No. 412)* (1995) pp. 423–427.

[60] P. C. Sen, *Principles of Electric Machines and Power Electronics* (John Wiley & Sons, 1997).

[61] J. L. Kirtley, J. L. Smith, and S. D. Umans, *Cryogenic isolating torque tubes for a superconducting generator-detailed model and performance analysis,* IEEE Transactions on Energy Conversion **6**, 267 (1991).

[62] N. Mijatovic, B. Jensen, C. Træholt, and A. Abrahamsen, *Superconducting wind turbine generators*, Ph.D. thesis (2014).

[63] S. Kalsi, D. Madura, T. MacDonald, M. Ingram, and I. Granta, *Operating experience of superconductor dynamic synchronous condenser,* in *2005/2006 IEEE/PES Transmission and Distribution Conference and Exhibition* (2006) pp. 899–902.

[64] T.-J. Yang, L. Horng, H.-S. Koo, and K. Chen, *Investigation of the bending effect and the critical current density on a Bi-Based superconducting tape,* in *Advances in Superconductivity V: Proceedings of the 5th International Symposium on Superconductivity (ISS '92), November 16–19, 1992, Kobe*, edited by Y. Bando and H. Yamauchi (Springer Japan, Tokyo, 1993) pp. 803–806.

[65] Y. Yang, G. Li, M. Susner, M. Sumption, M. Rindfleisch, M. Tomsic, and E. Collings, *Influence of twisting and bending on the Jc and n-value of multifilamentary MgB_2 strands,* Physica C: Superconductivity and its Applications **519**, 118 (2015).

[66] J. C. Eliassen, *Winding and Testing of Superconducting Coils*, Master's thesis, Norwegian University of Science and Technology, Department of Electric Power Engineering, Norway (2015).

[67] D. Kostopoulos, D. Liu, G. Genani, and H. Polinder, *Feasibility study of a 10 mw mgb_2 fully superconducting generator for offshore wind turbines,* in *2013 EWEA Offshore Proceedings* (2013) pp. 1–11.

[68] J. R. Bumby, *Superconducting Rotating Electrical Machines* (Oxford Univeristy Press, 1984).

[69] K. Kajikawa, Y. Uchida, T. Nakamura, H. Kobayashi, T. Wakuda, and K. Tanaka, *Development of stator windings for fully superconducting motor with MgB_2 wires,* IEEE Transactions on Applied Superconductivity **23**, 5201604 (2013).

[70] Y. Terao, M. Sekino, and H. Ohsaki, *Electromagnetic design of 10 MW class fully superconducting wind turbine generators,* IEEE Transactions on Applied Superconductivity **22**, 5201904 (2012).

[71] P. Tixador, Y. Brunet, P. Vedrine, Y. Laumond, and J. L. Sabrie, *Electrical tests on a fully superconducting synchronous machine,* IEEE Transactions on Magnetics **27**, 2256 (1991).

[72] P. N. Barnes, M. D. Sumption, and G. L. Rhoads, *Review of high power density superconducting generators: Present state and prospects for incorporating YBCO windings,* Cryogenics **45**, 670 (2005).

[73] Q. Jiang, M. Majoros, Z. Hong, A. M. Campbell, and T. A. Coombs, *Design and ac loss analysis of a superconducting synchronous motor,* Superconductor Science and Technology **19**, 1164 (2006).

[74] O. Tsukamoto, N. Amemiya, T. Takao, S. Akita, K. Ohishi, H. Shimizu, Y. Tanaka, and Y. Uchikawa, *Development of 30 kVA class fully superconducting generator,* IEEE Transactions on Magnetics **28**, 283 (1992).

[75] O. Tsukamoto, N. Amemiya, K. Yamagishi, T. Takao, S. Akita, S. Torii, K. Ohishi, and H. Shimizu, *Development and electrical test of a 30 kVA class fully superconducting generator,* IEEE Transactions on Magnetics **30**, 2308 (1994).

[76] J. R. Bumby and R. Martin, *Axial-flux permanent-magnet air-cored generator for small-scale wind turbines,* IEE Proceedings - Electric Power Applications **152**, 1065 (2005).

[77] A. S. Mcdonald, M. A. Mueller, and H. Polinder, *Structural mass in direct-drive permanent magnet electrical generators,* IET Renewable Power Generation **2**, 3 (2008).

[78] D. Bang, *Design of Transverse Flux Permanent Magnet Machines for Large Direct-Drive Wind Turbines*, Ph.D. thesis, Delft University of Technology (2010).

[79] A. Zavvos, D. Bang, A. McDonald, H. Polinder, and M. Mueller, *Structural analysis and optimisation of transverse flux permanent magnet machines for 5 and 10 MW direct drive wind turbines,* Wind Energy **15**, 19 (2012).

[80] M. Mueller and A. Zavvos, *Electrical generators for direct drive systems: a technology overview,* in *Electrical drives for direct drive renewable energy systems*, edited by M. Mueller and Henk Polinder (Woodhead Publishing, 2013) pp. 3–29.

[81] O. Keysan and M. A. Mueller, *A transverse flux high-temperature superconducting generator topology for large direct drive wind turbines,* Physics Procedia **36**, 759 (2012).

[82] D. Bang, H. Polinder, G. Shrestha, and J. A. Ferreira, *Review of generator systems for direct-drive wind turbines,* European Wind Energy Conference & Exhibition, Belgium , 1 (2008).

[83] A. Cavagnino, M. Lazzari, F. Profumo, and A. Tenconi, *A comparison between the axial flux and the radial flux structures for PM synchronous motors,* IEEE Transactions on Industry Applications **38**, 1517 (2002).

[84] U. Lucia, *Carnot efficiency: Why?* Physica A: Statistical Mechanics and its Applications **392**, 3513 (2013).

[85] A. B. Abrahamsen and et al., *First assessment of PI's for 10-20 MW SC and PDD generators*, Tech. Rep. (INNWIND.EU, 2013).

[86] T. Wada and A. Sato, *Basic experiment on the indirect cooling for superconducting magnets,* in *Advances in Cryogenic Engineering: Part A & B*, edited by R. W. Fast (Springer US, Boston, MA, 1990) pp. 849–856.

[87] F. N. Werfel and et al., *Technology, preparation, and characterization,* in *Applied Superconductivity* (Wiley-VCH Verlag GmbH & Co. KGaA, 2015) pp. 193–402.

[88] S. S. Kalsi, *Cooling and thermal insulation systems,* in *Applications of High Temperature Superconductors to Electric Power Equipment* (Wiley-IEEE Press, 2011) pp. 35–58.

[89] R. Radenbaugh, *Refrigeration for superconductors,* Proceedings of the IEEE **92**, 1719 (2004).

[90] W. E. Gifford, *The Gifford-McMahon Cycle,* in *Advances in Cryogenic Engineering: Proceedings of the 1965 Cryogenic Engineering Conference Rice University Houston, Texas August 23–25, 1965*, edited by K. D. Timmerhaus (Springer US, Boston, MA, 1966) pp. 152–159.

[91] M. Thirumaleshwar and S. Subramanyam, *Gifford-McMahon cycle — a theoretical analysis,* Cryogenics **26**, 177 (1986).

[92] R. Sier, *Hot Air Caloric and Stirling Engines: A history*, v. 1 (L.A. Mair, 1999).

[93] G. Popescu, V. Radcenco, E. Gargalian, and P. R. Bala, *A critical review of pulse tube cryogenerator research,* International Journal of Refrigeration **24**, 230 (2001).

[94] J. Ekin, *Experimental Techniques for Low-Temperature Measurements* (Oxford University Press, 2006).

[95] Babcock Noell GmbH, `http://www.bng.bilfinger.com/en/`, [Online], [Last accessed May 2017].

[96] J. He, Y. Tang, J. Li, L. Ren, J. Shi, J. Wang, R. Qu, L. Su, X. Li, Y. Xu, and Z. Zhu, *Conceptual design of the cryogenic system for a 12 MW superconducting wind turbine generator,* IEEE Transactions on Applied Superconductivity **24**, 1 (2014).

[97] S. Santiago and et al., *First modular cryostat*, Tech. Rep. (Suprapower, 2015).

[98] Suprapower, http://www.suprapower-fp7.eu/summary.php/, [Online], [Last accessed May 2017].

[99] Stirling cryogenics, http://www.stirlingcryogenics.com/Rotating-machines/, [Online], [Last accessed May 2017].

[100] B. B. Gamble, S. Kalsi, G. Snitchler, D. Madura, and R. Howard, *The status of HTS motors,* in *IEEE Power Engineering Society Summer Meeting,*, Vol. 1 (2002) pp. 270–274 vol.1.

[101] B. Gamble, G. Snitchler, and T. MacDonald, *Full power test of a 36.5 MW HTS propulsion motor,* IEEE Transactions on Applied Superconductivity **21**, 1083 (2011).

[102] R. Fair, C. Lewis, J. Eugene, and M. Ingles, *Development of an HTS hydroelectric power generator for the hirschaid power station,* Journal of Physics: Conference Series **234**, 032008 (2010).

[103] T. A. Keim, T. E. Laskaris, J. A. Fealey, and P. A. Rios, *Design and manufacture of a 20 MVA superconducting generator,* IEEE Power Engineering Review **PER-5**, 56 (1985).

[104] K. Sivasubramaniam, T. Zhang, M. Lokhandwalla, E. T. Laskaris, J. W. Bray, B. Gerstler, M. R. Shah, and J. P. Alexander, *Development of a high speed HTS generator for airborne applications,* IEEE Transactions on Applied Superconductivity **19**, 1656 (2009).

[105] H. W. Neumüller, W. Nick, B. Wacker, M. Frank, G. Nerowski, J. Frauenhofer, W. Rzadki, and R. Hartig, *Advances in and prospects for development of high-temperature superconductor rotating machines at siemens,* Superconductor Science and Technology **19**, S114 (2006).

[106] AMSC, http://www.amsc.com/documents/seatitan-10-mw-wind-turbine-data-sheet/, [Online], [Last accessed May 2017].

[107] Ecoswing, https://ecoswing.eu/, [Online], [Last accessed May 2017].

[108] ICMAB CSIC, http://departments.icmab.es/suman/2016/12/12/csic-institutes-materials-science-barcelona-aragon-together-gamesa-innovation-technology-develop-first-prototype-electric-superconducting-generator-medium-power-wi/, [Online], [Last accessed May 2017].

[109] Z. Chen, *Power electronic converter systems for direct drive renewable energy applications,* in *Electrical drives for direct drive renewable energy systems*, edited by M. Mueller and Henk Polinder (Woodhead Publishing, 2013) pp. 106–135.

[110] E. de Vries, *6 - wind turbine drive systems: a commercial overview,* in *Electrical Drives for Direct Drive Renewable Energy Systems*, Woodhead Publishing Series in Energy, edited by M. Mueller and H. Polinder (Woodhead Publishing, 2013) pp. 139 – 157.

[111] E. Hau, *Mechanical drive train and nacelle,* in *Wind Turbines: Fundamentals, Technologies, Application, Economics* (Springer Berlin Heidelberg, Berlin, Heidelberg, 2013) pp. 305–383.

[112] J. N. Stander, G. Venter, and M. J. Kamper, *Review of direct-drive radial flux wind turbine generator mechanical design,* Wind Energy **15**, 459 (2012).

[113] Siemens Wind Power, http://www.siemens.com/global/en/home/markets/wind.html/, [Online], [Last accessed May 2017].

[114] D. Dabrowski, A. Natarajan, and E. Stehouwer, *Structural optimization of an innovative 10 MW wind turbine nacelle,* in *Proceedings of the EWEA Annual Event and Exhibition 2015* (European Wind Energy Association (EWEA), 2015) paper for poster presentation.

[115] G. Snitchler, *A direct drive wind turbine HTS generator,* in *IEEE Power Engineering Society General Meeting* (2007) pp. 1–8.

[116] G. Snitchler, B. Gamble, C. King, and P. Winn, *10 MW class superconductor wind turbine generators,* IEEE Transactions on Applied Superconductivity **21**, 1089 (2011).

[117] B. Maples, M. M. Hand, and W. D. Musial, *Comparative assessment of direct drive high temperature superconducting generators in multi-megawatt class wind turbines*, Tech. Rep. (Golden, CO: National Renewable Energy Laboratory, 2010).

[118] S. S. Kalsi, *Rotating ac machines,* in *Applications of High Temperature Superconductors to Electric Power Equipment* (Wiley-IEEE Press, 2011) pp. 59–128.

[119] Y. Liu, R. Qu, and J. Wang, *Comparative analysis on superconducting direct-drive wind generators with iron teeth and air-gap winding,* IEEE Transactions on Applied Superconductivity **24**, 1 (2014).

[120] Y. Xu, N. Maki, and M. Izumi, *Electrical design study of 10-MW salient-pole wind turbine HTS synchronous generators,* IEEE Transactions on Applied Superconductivity **24**, 1 (2014).

[121] D. Liu, H. Polinder, N. Magnusson, J. Schellevis, and A. B. Abrahamsen, *Ripple field ac losses in 10-mw wind turbine generators with a MgB_2 superconducting field winding,* IEEE Transactions on Applied Superconductivity **26**, 1 (2016).

[122] A. B. Abrahamsen, N. Magnusson, B. B. Jensen, D. Liu, and H. Polinder, *Design of an MgB_2 race track coil for a wind generator pole demonstration,* Journal of Physics: Conference Series **507**, 032001 (2013).

[123] J. Pyrhonen, T. Jokinen, and V. Hrabovcova, *Design of Rotating Electrical Machines* (New York: Wiley, 2009).

[124] J. Manwell, J. McGowan, and A. Rogers, *Wind Energy Explained: Theory, Design and Application: 2nd edition* (Wiley, 2009).

[125] T. Burton, N. Jenkins, D. Sharpe, and E. Bossanyi, *Wind Energy Hand Book: 2nd edition* (Wiley, 2011).

[126] A. A. Arkadan, R. Vyas, J. G. Vaidya, and M. J. Shah, *Effect of toothless stator design and core and stator conductors eddy current losses in permanent magnet generators,* IEEE Transactions on Energy Conversion **7**, 231 (1992).

[127] H. Polinder, F. F. A. van der Pijl, G. J. de Vilder, and P. J. Tavner, *Comparison of direct-drive and geared generator concepts for wind turbines,* IEEE Transactions on Energy Conversion **21**, 725 (2006).

[128] K. Deb, A. Pratap, S. Agarwal, and T. Meyarivan, *A fast and elitist multiobjective genetic algorithm: NSGA-II,* IEEE Transactions on Evolutionary Computation **6**, 182 (2002).

[129] S. Lin, `http://nl.mathworks.com/matlabcentral/fileexchange/31166-ngpm-a-nsga-ii-program-in-matlab-v1-4/`, [Online], [Last accessed May 2017].

[130] N. Bianchi and S. Bolognani, *Design optimisation of electric motors by genetic algorithms,* IEE Proceedings - Electric Power Applications **145**, 475 (1998).

[131] H. Polinder, D. Bang, R. P. J. O. M. van Rooij, A. S. McDonald, and M. A. Mueller, *10 MW wind turbine direct-drive generator design with pitch or active speed stall control,* in *2007 IEEE International Electric Machines Drives Conference*, Vol. 2 (2007) pp. 1390–1395.

[132] P. Chaviaropoulos and A. Natarajan, *Definition of Performance Indicators (PIs) and Target Values*, Tech. Rep. (INNWIND.EU, 2014).

[133] A. B. Abrahamsen and A. Natarajan, *Variation of extreme and fatigue design loads on the main bearing of a front mounted direct drive system,* Journal of Physics: Conference Series **765**, 112006 (2016).

[134] J. F. Gieras, *Advancements in Electric Machines* (Springer-Verlag, 2008).

[135] H. London, *Alternating current losses in superconductors of the second kind,* Physics Letter **6**, 162 (1963).

[136] C. P. Bean, *Magnetization of high-field superconductors,* Reviews of Modern Physics **36**, 31 (1964).

[137] W. J. Carr, *AC Loss and Macroscopic Theory of Superconductors* (CRC Press, 2001).

[138] M. N. Wilson, *Superconducting Magnets* (Clarendon, 1983).

[139] B. ten Haken, J. J. Rabbers, and H. H. J. ten Kate, *Magnetization and AC loss in a superconductor with an elliptical cross-section and arbitrary aspect ratio,* Physica C: Superconductivity **377**, 156 (2002).

[140] Z. Chen and et al., *Deliverable 3.31: Converter designs tailored to SC and PDD concepts*, Tech. Rep. (INNWIND.EU) [Online], [Last accessed May 2017].

[141] J. Morren, J. Pierik, and S. W. de Haan, *Inertial response of variable speed wind turbines,* Electric Power Systems Research **76**, 980 (2006).

[142] H. Li, Z. Chen, and H. Polinder, *Optimization of multibrid permanent-magnet wind generator systems,* IEEE Transactions on Energy Conversion **24**, 82 (2009).

[143] C. Stuebig, A. Seibel, K. Schleicher, L. Haberjan, M. Kloepzig, and B. Ponick, *Electromagnetic design of a 10 MW permanent magnet synchronous generator for wind turbine application,* in *2015 IEEE International Electric Machines Drives Conference (IEMDC)* (2015) pp. 1202–1208.

[144] A. K. Sawhney, *A Course in Electrical Machine Design* (Delhi: Dhanpat Rai & Co., 2006).

[145] Z. Zhang, A. Matveev, S. Øvrebø, R. Nilssen, and A. Nysveen, *State of the art in generator technology for offshore wind energy conversion systems,* in *2011 IEEE International Electric Machines Drives Conference (IEMDC)* (2011) pp. 1131–1136.

[146] E. Seiler, D. Richter, B. Bordini, L. Bottura, D. Bessette, A. Vostner, and A. Devred, *Hysteresis losses and effective $j_c(b)$ scaling law for ITER Nb3Sn strands,* IEEE Transactions on Applied Superconductivity **26**, 1 (2016).

[147] D. Doll and et al., *The markets that are opening for mgb_2 superconductors and related applications,* (Presented at 11th European Conference on Applied Superconductivity, Contribution 1M-WT-I1, Genova, 2013).

[148] D. W. Hazelton, *2G HTS Conductors at SuperPower,* (presented at Low Temperature High Field Superconductor Workshop 2012 (LTHFSWS2012), Napa, CA, USA, 2012).

[149] R. Nakasakiet and et al., *Progress of 2G HTS wire development at SuperPower,* (Presented at Applied Superconductivity Conference, ASC 2016, 1MOr2A-03, September 4-9, 2016, Denver, CO, USA, 2016).